Dissertation

submitted to the

Combined Faculties for the Natural Sciences and for Mathematics

of the Ruperto-Carola University of Heidelberg, Germany

for the degree of

Doctor of Natural Sciences

presented by

M. Sc. Dmytro Dvornikov

born in Tula, Russian Federation

Oral examination: 30th November 2017

Transforming Growth Factor beta signaling in lung cancer: molecular alterations, biomarkers and novel regulatory mechanisms revealed by mathematical modeling

Referees: Prof. Dr. Ursula Klingmüller

Prof. Dr. Thomas Höfer

Live as if you were to die tomorrow.

Learn as if you were to live forever.

– Mahatma Gandhi

Моим маме и папе, и особенно Валечке.

Acknowledgements

Many people have accompanied me over the years that I devoted to my PhD project. Finally, I have the honor of expressing my gratitude for all their help and support.

First of all, my deepest thankfulness goes to my first supervisor Prof. Dr. Ursula Klingmüller for granting me the opportunity to carry out my PhD project in her lab. I will always be grateful for her scientific guidance and support. I am especially thankful for engagement in multiple exciting projects and collaborations. I have learnt and developed a lot over these years. I thank Prof. Dr. Thomas Höfer for agreeing to be the second referee of this thesis and being a member of my TAC committee meetings. Also, many thanks to Prof. Dr. Britta Brügger for acting as a chair examiner in my thesis defense and to Prof. Dr. Stefan Wiemann for his willingness to be part of my thesis defense examination committee.

This work would not have been possible without the help of many great collaboration partners. First of all, I am very grateful to my modeling partner Dr. Raphael Engesser. It was a true pleasure working with you. I could not have wished for a better modeler. I want to thank Sebastian Ohse, Dr. Hauke Busch and Dr. Melanie Börries for performing the analysis of RNA-Seq data. I also thank Dr. Marc Schneider, Dr. Michael Meister and Dr. Thomas Muley for analysis of patient samples and corresponding survival analysis. I am grateful to PD Dr. Karin Müller-Decker for support with *in vivo* mice experiments. I thank Dr. Martin Böhm for mass spectrometric analysis of Smad2/3 degree of phosphorylation and for sharing his invaluable knowledge regarding the mass spectrometry. I want to express many thanks to Dr. Damir Krunic for his kind assistance with microscopy and image analysis.

I also would like to acknowledge Dr. Marcel Schilling. Your clear analytical thinking, fruitful discussions, constructive criticism and numerous advices had a huge impact on the success of my PhD project. Life of every PhD student in the lab would have been much more difficult without you being around. Thank you for always being there for us.

I want to thank all-all-all current and previous A150/B200 members for truly friendly and creative atmosphere. Thanks to you I was always looking forward to my every day in the lab. Special thanks go to Susen, Marvin and Sandra for keeping the lab in shape, taking care of all the ordering, and making sure that the stock reagents and consumables are always available. I also thank my PhD fellows Flo (the best conference roommate and the kindest person ever), Frederique and Lorenz for friendly atmosphere and constant support; Dr. Stephanie Müller for many helpful advices and support during my early days in the lab; Angela for always staying positive and tolerating my mess; Artyom, Irina, Anja, Claire, Viktor and

Melisa for bringing new young life and smiles to the lab. I am also thankful to all my students that I supervised over these years (Artyom, Liza, Ksenia, Elli, Tamara), as I learned many lessons of my own together with you. I want to thank the secretary of our lab, Martina, for taking care of numerous small things that made the life of PhD students in our lab so much easier. I am grateful to my new box members, Martin and Marv, for their warm welcome and easy-going working atmosphere.

Magda, I am so lucky that our life paths have crossed in summer 2014. There are no words to describe my gratitude for all your help, unconditional support, and endless science-related and unrelated discussions. Thank you for always being there for occasional cup of tea or coffee, being my sports-mate and the most fearsome board game opponent. Your infinite energy combined with an unbreakable spirit is something that will always inspire me. You are truly an amazing person.

Last of all I would like to thank my dearest friends outside of the lab and my family.

Sergy Havrylov, meeting you back in December 2007 has definitely changed the course of my life. You made me look differently on many things, you made me think about something that I have never considered before, and most importantly you inspired me to choose the perilous but nevertheless exciting path of a scientist. I have no regrets of doing so. Thank you!

I also want to say my special big-big thanks to Sergy Velychko, a man with whom we shared more than just a room in Ukrainian dormitory. We went together, side-by-side through all the perils of bachelor studies, applying abroad, studying in Germany and pursuing our PhD studies afterwards. Thank you for all the fun that we had, thank you for being literally our personal photographer, thank you for all our trips together and all the joyful colorful moments.

Most importantly, I cannot imagine going through these years of PhD without constant support and encouragements from my beloved wife, Valentina. I am so happy to have you in my life. No matter what storms were battering around, you always remained the island of peace and tranquility in my life. Thank you for all your patience, all unforgetful moments and always being there for me. I love you so much.

Last but not the least, I am grateful to my parents, Natalia and Sergey, for believing in me and supporting along this long and treacherous path.

Contents

Publications

*Dvornikov D, *Schneider MA, *Ohse S, Szczygieł M, Titkova I, Rosenblatt M, Muley T, Warth A, Herth FJ, Dienemann H, Thomas M, Timmer J, Schilling M, Busch H, Boerries M, Meister M, Klingmüller U. "Expression ratio of TGFβ-inducible MYO10 is prognostic for overall survival of squamous cell lung cancer patients and predicts chemotherapy response". *Under review.*

Ucar O, Li K, Dvornikov D, Kreutz C, Timmer J, Matt S, Brenner L, Smedley C, Travis MA, Hofmann TG, Klingmüller U, Kyewski B. "A Thymic Epithelial Stem Cell. Pool Persists throughout Ontogeny and Is Modulated by TGF-β". **Cell Rep**. 2016 Oct 4;17(2):448-457.
doi: 10.1016/j.celrep.2016.09.027. PubMed PMID: 27705793; PubMed Central PMCID: PMC5067280.

*Marwitz S, *Depner S, *Dvornikov D, Merkle R, Szczygieł M, Müller-Decker K, Lucarelli P, Wäsch M, Mairbäurl H, Rabe KF, Kugler C, Vollmer E, Reck M, Scheufele S, Kröger M, Ammerpohl O, Siebert R, Goldmann T, Klingmüller U. "Downregulation of the TGFβ Pseudoreceptor BAMBI in Non-Small Cell Lung Cancer Enhances TGFβ Signaling and Invasion". **Cancer Res**. 2016 Jul 1;76(13):3785-801.
doi: 10.1158/0008-5472.CAN-15-1326. Epub 2016 May 17. PubMed PMID: 27197161.

* shared first-authorship

Summary

Non-small-cell lung cancer (NSCLC) is the leading cause of cancer-related mortalities worldwide. NSCLC can be further subdivided in lung adenocarcinoma (LUAD) and lung squamous cell carcinoma (LUSC). Elevated levels of the Transforming Growth Factor beta (TGFβ) ligand correlate with a poor survival of lung cancer patients. However, the underlying mechanisms contributing to the pro-tumorigenic effects of TGFβ signal transduction in lung cancer are poorly understood.

First, the activation status of the TGFβ signal transduction was examined at the protein and mRNA level in tumor tissue of lung cancer patients. This analysis revealed that the components of the TGFβ pathway were substantially activated in human lung cancer tissue with concomitant epigenetic silencing of a negative regulator of the TGFβ pathway, the decoy pseudoreceptor BAMBI. Reconstitution of BAMBI in NSCLC cells decreased TGFβ-induced Smad2/3 phosphorylation and TGFβ-induced *in vitro* cell migration and invasion. Furthermore, BAMBI reconstitution reduced the *in vivo* metastatic potential of NSCLC cell lines as assessed by a mouse lung colonization assay. These results demonstrated that the loss of the negative regulator BAMBI promotes the activation of the TGFβ pathway as well as TGFβ-driven invasiveness of lung tumors.

Second, molecular components contributing to TGFβ-induced lung cancer progression were investigated. The dynamics of gene expression in TGFβ-treated LUSC cells was assessed by next-generation mRNA sequencing. The examinations revealed up-regulation of motility- and actin cytoskeleton-related genes including the non-muscle myosin 10 (*MYO10*). Knockdown of MYO10 abrogated TGFβ-induced collagen gel invasion of LUSC cells. Examination of mRNA expression in paired surgically resected tissues of LUSC patients showed that the mRNA expression ratio of *MYO10* in tumor and tumor-free tissue is prognostic for patient overall survival and facilitates the prediction of the response of these patients to adjuvant chemotherapy.

Having established that the TGFβ signal transduction pathway is deregulated in lung cancer, it is important to understand how the dynamic properties of the pathway are controlled. The analysis of TGFβ-induced signal transduction in three LUAD cell lines showed a distinct dynamic behavior of the TGFβ-induced Smad2/3 phosphorylation and a differential impact of inhibitor perturbations. These results suggested a different prevalence of negative feedbacks that induce the degradation of the TGFβ receptor or reduce its ability to phosphorylate Smads in the examined cell lines. The model-based analysis predicted that the TGFβ receptor protein undergoes constant turnover: the unstable receptor protein is constantly degraded and produced again from the stable receptor mRNA. High stability of the TGFβ receptor mRNA was confirmed by mRNA half-life analysis, while the accumulation of the TGFβ receptor protein upon inhibition of the proteasome function was validated using targeted quantitative mass spectrometry. These findings highlighted that the TGFβ receptor is one of the most sensitive nodes that controls pathway activation. Therefore, targeting processes that control receptor abundance rather than using conventional TGFβ receptor kinase inhibitors could be a promising therapeutic approach.

Taken together, the presented work provides insights into molecular alterations that cause TGFβ pathway deregulation, suggests new potential biomarkers and showcases the potential of the mathematical modeling approach combined with quantitative experiments to uncover general principles of cell type-specific regulation of TGFβ-induced Smad2/3 phosphorylation in lung cancer cell lines.

Zusammenfassung

Das nichtkleinzellige Lungenkarzinom (*non-small-cell lung cancer*, NSCLC) verursacht weltweit die meisten Todesfälle von Krebspatienten. Bei NSCLC wird zwischen Adenokarzinom (*lung adenocarcinoma*, LUAD) und Plattenepithelkarzinom (*lung squamous cell carcinoma*, LUSC) unterschieden. Erhöht Werte des Liganden *transforming growth factor beta* (TGFβ) korrelieren mit schlechten Überlebensprognosen. Die zugrunde liegenden Mechanismen, die zu der krebsfördernden Wirkung der TGFβ-Signaltransduktion beitragen, sind jedoch größtenteils unbekannt.

In dieser Arbeit wurde zuerst in Tumorgeweben von Lungenkrebspatienten der Aktivierungsstatus der TGFβ-Signaltransduktion auf Protein- und mRNA-Ebene untersucht. Die Analyse zeigte eine substantielle Aktivierung der Komponenten der TGFβ-Signaltransduktion im humanen Lungenkrebsgewebe. Diese Aktivierung ging mit einer gleichzeitigen epigenetischen Abschaltung eines negativen Regulators der TGFβ-Signaltransduktion einher, des nichtfunktionalen Pseudorezeptors BAMBI. Das Wiedereinbringen von BAMBI in NSCLC-Zellen verringerte die von TGFβ induzierte Phosphorylierung von Smad2/3 sowie die von TGFβ induzierte Zellmigration und Zellinvasion *in vitro*. Weiterhin konnte durch Kolonisierungsversuche in Mauslungen gezeigt werden, dass das Wiedereinbringen von BAMBI *in vivo* das Potential zur Metastasenbildung von NSCLC-Zelllinien reduziert. Diese Ergebnisse zeigten, dass der Verlust des negativen Regulators BAMBI die Aktivierung der TGFβ-Signaltransduktion sowie die von TGFβ verursachte Zellinvasion in Lungenkarzinomen erhöht.

Als nächstes wurden die molekularen Komponenten untersucht, die zu einer von TGFβ induzierten Lungenkrebsprogression beitragen. Die Dynamik der Genexpression in mit TGFβ stimulierten LUSC-Zellen wurde mittels Next-Generation-mRNA-Sequencing untersucht. Die Resultate zeigten eine Erhöhung von Zellmotilität- und Actin-Zellskelett-Genen, darunter das nicht-muskuläre Myosin 10 (MYO10). Der Knockdown von *MYO10* verhinderte die von TGFβ induzierte Kollagen-Gel-Invasion von LUSC-Zellen. Die Untersuchung der mRNA-Expression in gepaarten operativ entfernten Lungengeweben von LUSC-Patienten zeigte, dass das mRNA-Expressionsverhältnis von MYO10 zwischen Tumor- und tumorfreiem Gewebe ein prognostischer Faktor für das Gesamtüberleben der Patienten ist. Zusätzlich ermöglicht dieses Expressionsverhältnis eine Vorhersage der Patientenantwort auf adjuvante Chemotherapie.

Da diese Arbeit eine Veränderung der TGFβ-Signaltransduktion im Lungenkrebs gezeigt hat, wurde ein genaues Verständnis der Kontrolle der dynamischen Eigenschaften dieses Signalwegs angestrebt. Die Analyse der von TGFβ induzierten Signaltransduktion in drei LUAD-Zelllinien zeigte verschiedene dynamische Verhaltensweisen der von TGFβ induzierten Phosphorylierung von Smad2/3 und einen unterschiedlichen Einfluss von Inhibitoren. Diese Ergebnisse deuten auf eine unterschiedliche Ausprägung von negativen Rückkopplungsmechanismen in den drei Zelllinien hin. Die negativen Rückkopplungsmechanismen verstärken einerseits den Abbau des TGFβ-Rezeptors, während sie andererseits die Aktivität des Rezeptors in Bezug auf die Phosphorylierung der Smad-Proteine verringern. Eine Analyse eines mathematischen Modells sagte voraus, dass der TGFβ-Rezeptors einem konstanten Umsatz unterworfen ist: das instabile Rezeptor-Protein wird fortwährend degradiert und mittels der stabilen Rezeptor-mRNA neu gebildet. Die hohe Stabilität der TGFβ-Rezeptor-mRNA wurde mit Hilfe einer mRNA-Halbwertszeit-Analyse bestätigt, während die Anhäufung des TGFβ-Rezeptor-Proteins nach Inhibierung der Proteasom-Funktion durch gezielte quantitative Massenspektrometrie validiert wurde. Diese Ergebnisse unterstreichen, dass der TGFβ-Rezeptor einer der sensitivsten Knotenpunkte für die Kontrolle des Signalwegs darstellt. Aus diesem Grund könnte statt konventioneller TGFβ-Rezeptor-Inhibitoren die gezielte Inhibierung von zellulären Prozessen, die die Rezeptormenge kontrollieren, einen vielsprechenden therapeutischen Ansatz darstellen.

Zusammengenommen gibt die vorliegende Arbeit Aufschluss über die molekularen Veränderungen, die die Deregulierung des TGFβ-Signalwegs verursachen, sagt neue potentielle Biomarker vorher und demonstriert das Potential eines mathematischen Modells in Verbindung mit quantitativen Experimenten, um generelle Eigenschaften der Zelltyp-spezifischen von TGFβ induzierten Phosphorylierung von Smad2/3 in Lungenkrebszelllinien aufzudecken.

1 Introduction

1.1 Lung cancer

1.1.1 Classification and etiology

Lung cancer is the leading cause of cancer-related mortalities with more than two million deaths per year (1). The major subtypes of lung cancer are small-cell lung cancer (SCLC) and non-small-cell lung cancer (NSCLC) with the latter accounting for 80% of all lung tumors. NSCLC can be further subdivided in lung adenocarcinoma (LUAD), lung squamous cell carcinoma (LUSC) and lung large-cell carcinoma (LCC). LUAD is the most prevalent form (60%), followed by LUSC (35%) and LCC (5%) (2). Although LCC appear as poorly differentiated tumors with a distinct histology than LUAD and LUSC, genetically LCC tumors closely resemble either LUSC and LUAD (3). Therefore, LCC most probably comprises certain subtypes of LUSC or LUAD and thus will not be further covered separately in details in this thesis.

Smoking is the main risk factor for developing lung cancer. Smokers have 5- to 10-fold higher chance of lung cancer with a clear dose-response relationship (4). However non-smokers (<100 cigarettes in a lifetime) still have 1% chance to develop a lung cancer over the lifetime. Non-smokers almost exclusively develop lung adenocarcinomas with a higher chance of having driver oncogene mutations (5).

1.1.2 Genomic alterations

Lung cancer is characterized by a high degree of molecular heterogeneity and a high mutational burden when compared to other cancer types (6). Such a high mutation rate in lung tumors is explained by the mutagenic effect of cigarette smoke (7). Indeed, it was demonstrated that lung tumors in smokers have increased frequency of cytosine to adenine mutations that are usually associated with tobacco smoke. Importantly, the mutational landscapes of LUAD and LUSC substantially differ from each other (**Table 1.1**). LUAD is characterized by high frequency of oncogenic driver mutations, the mutations that are believed to be responsible for tumor initiation and progression (8). Somatic copy number alterations, point mutations and gene fusions affecting driver oncogenes are identifiable in nearly 76% of LUAD patients (9). Among the most frequently mutated oncogenes are *KRAS* (33% in TCGA cohort), *EGFR* (16%), *BRAF* (7%), *MET* (6.5%), *ALK* and *ROS1* fusions (each <4%) and *ERBB2* (<2%). Additionally, loss-of-function mutations in TP53 are observed in almost 47% LUAD patients (10).

	LUAD	LUSC
Mutations	*TP53*, *KRAS*, *EGFR*, *BRAF*, *MET*	*TP53*, *CDKN2A*, *PIK3CA*, *KEAP1*, *PTEN*, *NOTCHs*, *EGFR*
Fusions	*ALK*, *ROS1*, *RET*	*FGFRs*
SCNAs	Gains: *TERT*, *TTF1*, *MYC* Losses: *CDKN2A*	Gains: *SOX2*, *PIK3CA*, *TP63* Losses: *CDKN2A*, *PTEN*
Altered pathways	RTK / RAS / RAF mTOR Cell cycle regulation	Squamous differentiation Oxidative stress response PIK3CA Cell cycle regulation

SCNA = somatic copy number alterations

Table 1.1. Recurrent genomic alterations in adenocarcinoma of the lung (LUAD) and squamous cell carcinoma of the lung (LUSC). Adapted and modified from Devarakonda et al. (10). For the full names of genes refer to the list of abbreviations.

In contrast, driver oncogene mutations, such as activating mutations in *KRAS*, *EGFR* and *BRAF* genes, are rarely observed in LUSC patients. Instead, gene amplifications (*EGFR* and *FGFR1*) and loss of onco-suppressors (*TP53* and *CDKN2A*) are commonly reported in LUSC context (11).

1.1.3 Clinical management of lung cancer

Until late 1990, platinum-based general cytotoxic chemotherapy was the only available therapeutic option for late-stage lung cancer patients independently of tumor histology. Since then treatment of NSCLC has undergone profound changes. Recent progress in uncovering the complex mutational landscape of lung cancer has enabled introduction of new drugs based on patient-specific molecular alterations. Currently, all adenocarcinoma patients are routinely screened for *EGFR* activating mutations and *ALK* translocations. In case such alterations are found, targeted drugs can be administrated already as a first-line therapy. This results in a higher tumor response rate and improved progression-free survival in comparison with standard care platinum-based chemotherapy (12, 13). The importance of other clinically relevant molecular aberrations, such as *MET* amplification and *ROS1* translocations, are currently investigated in clinical trials.

Finally, recent progress in immune-related therapies offers new treatment possibilities of lung cancer. Immunotherapy-based approaches were shown to be effective in both squamous and non-squamous NSCLC patients. Drugs that target immunosuppression checkpoints (anti-PD-L1 and anti-CTLA-4) proved to be effective in extending overall survival of previously-treated patients or even in some cases resulted in a complete tumor remission with much less treatment-related side effects when compared to standard chemotherapy (14, 15). However, a low response rate of only 15–20% and absence of reliable predictive biomarkers to identify patients that will benefit from the therapy greatly limits the use of this

approach. Thus, this calls for new combinatorial treatments to boost anti-tumor immune response alongside with an identification of new biomarkers that will allow patient stratification.

1.1.4 Major challenges in lung cancer treatment

Despite recent advances in molecular diagnosis and targeted therapies, over half of lung cancer patients die within one year of diagnosis with the 5-year-survival being only 18% (16). There are three main challenges that complicate the fight against lung cancer.

Asymptomatic progression and early metastasis. More than 40% of NSCLC patients have already distant metastasis at the time of their first hospital admission (17). The major reasons for that are an excessive lung volume that allows tumor to grow unnoticed without affecting patient's everyday performance and a vast capillary network of the lung that allows an easy spread of disseminating tumor cells. Early preventive screening of patients at high risk of developing a lung cancer as well as better understanding of the molecular mechanisms facilitating early metastasis are crucial in tackling this challenge.

Acquired therapy resistance. Despite introduction of new treatment approaches the median survival of lung cancer patients has only marginally improved from 6 months in the 80s to 9–12 months nowadays (18). Patients with specific oncogenic mutations acquire resistance to targeted therapies against EGFR or ALK already several months after treatment (19, 20). Several mechanisms of acquired resistance exist. First, the target gene undergoes either amplification or acquires a second mutation that interferes with the binding of the drug. Wildtype *EGFR* amplification or $EGFR^{T790M}$ mutation are the most prominent examples of such scenario. Second, re-wiring of the signaling network occurs that results in the use parallel pathways (bypass tracks) instead of the drug-targeted pathway to drive tumor cell survival and proliferation. For example, *MET* amplification is frequently observed in the patients that develop resistance against anti-EGFR therapy. Finally, acquisition of an epithelial-to-mesenchymal transition (EMT) phenotype is associated with resistance to both targeted and general cytotoxic chemotherapies (21, 22). Cancer cells that underwent EMT have rewired signaling transduction and metabolic networks, reduced rates of cell division, an upregulated DNA repair machinery and show increased expression of multidrug resistance transporters, therefore reducing the efficiency of conventional cytotoxic chemotherapy (23).

Lack of predictive biomarkers for general chemotherapy. In contrast to molecularly targeted and immune therapies, where predictive biomarkers are either already available or actively being developed, there are no commonly accepted predictive biomarkers for general cytotoxic chemotherapy in lung

cancer (24). However, cytotoxic chemotherapy still remains a standard first-line therapy for the majority of NSCLC patients (25). Therefore, finding such robust predictive biomarkers would personalize lung cancer treatment by identifying chemotherapy-responsive patients, thus avoiding unnecessary toxicities and ultimately improving patient outcome.

1.2 Transforming Growth Factor beta (TGFβ) signaling pathway

Transforming Growth Factor beta (TGFβ) cytokine was first isolated from Moloney sarcoma virus (MSV)-transformed fibroblasts in 1978 (25). Although TGFβ was initially believed to be a pro-proliferative cytokine as it was causing anchorage-independent growth of fibroblasts (26), nowadays it is widely accepted as one of the most potent anti-proliferative cytokines (27). The TGFβ superfamily of cytokines consists of 33 structurally related dimeric proteins in humans (28). These cytokines tightly orchestrate a variety of processes of embryonic development and adult tissue homeostasis by regulating cell proliferation, differentiation, apoptosis and migration in context-dependent and tissue-specific manner (29).

1.2.1 Canonical Smad signaling pathway

The core TGFβ signaling pathway is a conceptually simple and linear pathway (**Figure 1.1**). Pathway activation is initiated by ligand-induced formation of the tetrameric complexes consisting of two pairs of specific type I and type II TGFβ receptors (TβR1 and TβR2, respectively) that possess serine/threonine kinase activity (30). Complex formation enables constitutively active TβR2 to phosphorylate the glycine- and serine-rich (GS) juxtamembrane domain of TβR1. Phosphorylation triggers conformational changes in TβR1 and thus, activates its kinase activity (31). The activated TβR1 in turn, propagates the intracellular signaling through phosphorylation of receptor-regulated (R)-Smad proteins, e.g. Smad2/3, at two C-terminal serine residues (32). Two activated R-Smads form trimeric complexes with one common (Co)-Smad, Smad4, translocate to the nucleus, where they recruit additional sequence-specific DNA-binding co-factors as well as transcriptional co-activators and co-repressors to fine-tune the expression of target genes (33).

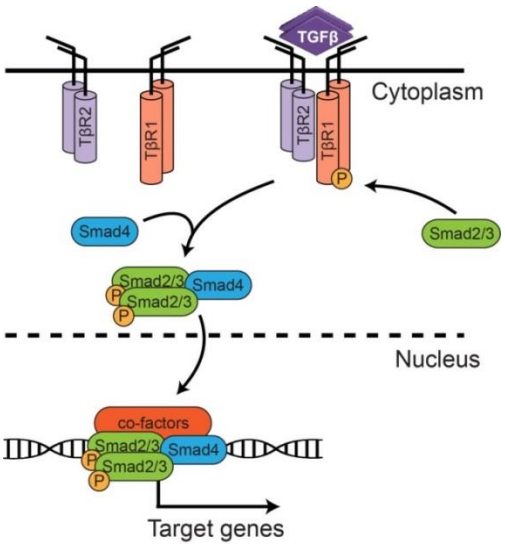

Figure 1.1. Scheme of the canonical TGFβ/Smad signaling pathway. Dimeric TGFβ ligand, shown as dark violet diamonds, initiates the pathway activation by binding to two type I TGFβ receptors (shown as TβR1) and two type II TGFβ receptors (shown as TβR2). This promotes phosphorylation of the TβR1 (indicated by encircled P) by constitutively active TβR2. Activated TβR1, in turn phosphorylates Smad2/3 molecules (green ellipses, phosphorylation is indicated by encircled P). Activated Smad2/3 proteins form trimeric complex with Smad4 (blue ellipse), translocated into a nucleus, recruit additional co-factors (red ellipse) and induce gene expression.

There are seven human type I and five type II TGFβ receptors. Each of the 33 cytokines that belong to the TGFβ superfamily is recognized by a specific combination of type I and type II receptors (**Figure 1.2**) (34). Based on the R-Smads that they phosphorylate, TGFβ type I receptors can be further subdivided into those that activate Smad2/3 proteins (TGFβ branch), and those that phosphorylate Smad1/5/8 in response to bone morphogenetic proteins (BMP branch). Additionally, inhibitory (I)-Smads, namely Smad6 and Smad7, are crucial for repressing TGFβ/Smad signal transduction in BMP and TGFβ branches respectively (35, 36).

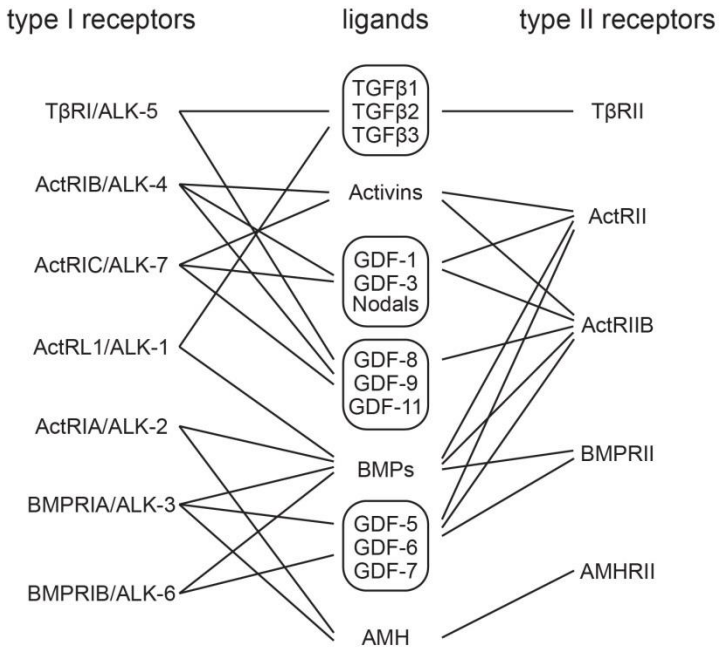

Figure 1.2. Scheme of binding specificity of type I and type II TGFβ receptors to their corresponding ligands. Adapted and modified from Heldin and Moustakas (34).

R-Smads (Smad2 and Smad3) and Smad4 molecules consist of two Mad-homology (MH) domains coupled by a linker region (32) (**Figure 1.3**). The N-terminal domain, MH1, is evolutionary conserved and present in the R-Smads and Smad4, but not in inhibitory Smads 6 and 7 (37, 38). MH1 domain of these Smads harbors β-hairpin structure for DNA binding. The MH1 domain of Smad2 is an exception as it has two insertions (L1 and exon 3) that prevent DNA binding (39). The MH2 domain is present in all Smads and is mainly responsible for protein-protein interactions. Additionally, it facilitates interaction with the TβRI (40). The MH2 domain also mediates interactions with nucleoporins, transcription factors, such as the forkhead, homeobox and zinc-finger families, co-repressors – among them Ski and SnoN, and co-activators, such as p300/CBP (41, 42). R-Smads contain a C-terminal motif Ser-X-Ser which serves as a phosphorylation site for the activated type I TGFβ receptor. The linker region between the MH domains contains multiple Ser/Thr phosphorylation sites which are targets for Cdk and Erk kinases (43).

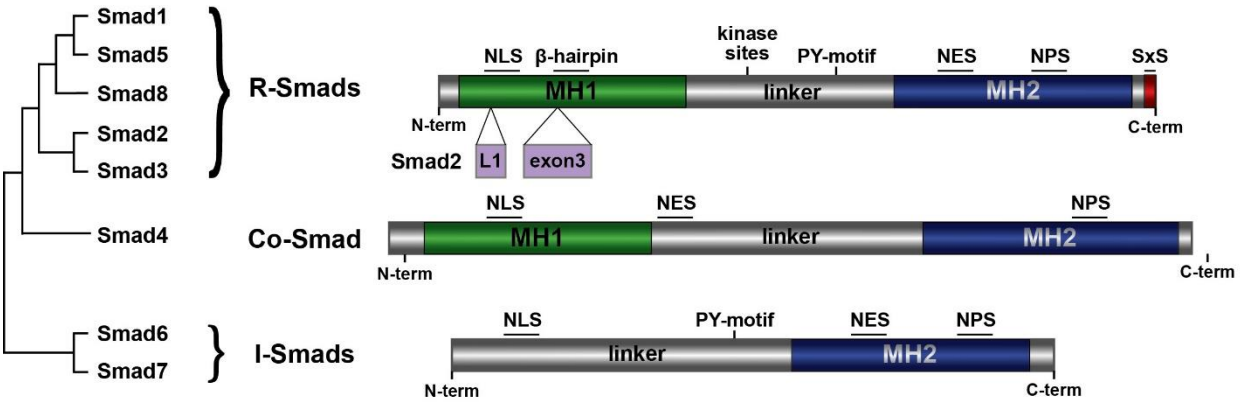

Figure 1.3. Phylogenetic tree and schematic structures of Smads. There are three Smad subgroups: R-Smads, I-Smads, and Co-Smad. MH1 and MH2 domains are shown in green and blue, respectively. The C-terminal SxS motif of R-Smads is phosphorylated by activated type I TGFβ receptors. Smad2 contains two inserts in its MH1 domain (L1 and exon 3), which are not found in other R-Smads. I-Smads lack MH1 domain. The linker region of R-Smads contains multiple phosphorylation sites for MAPKs, CDKs, and other protein kinases. In R-Smads and I-Smads, the linker region contains a PY motif for recognition by the WW domains in Smurf ubiquitin ligases. Nuclear export signals (NES), nuclear localization signals (NLS) and nucleopore signals (NPS) are located in the MH1 or MH2 domains of Smads. Adapted from ten Dijke and Hill (44).

There are three isoforms of the TGFβ ligand encoded in the human genome, TGFβ1, TGFβ2 and TGFβ3. The isoforms differ in their affinity for the TGFβ receptors. While TGFβ1 and TGFβ3 bind TβR2 with higher affinity than TβR1, TGFβ2 shows rather low affinity for TβR2 and thus requires additional co-receptors such as betaglycan (also known as type III TGFβ receptor) and endoglin (45). TGFβ1 is considered the prototype ligand for the TGFβ signaling branch.

TGFβ dimers are secreted by the cell in the inactive state bound to latency-associated peptide (LAP) and the latent TGFβ-binding protein (LTBP) (46). Such trimeric complexes are deposited within the extracellular matrix (ECM) and have to be activated by proteolytic cleavage to become available for cells (47).

In addition to Smad-dependent signaling, TGFβ receptors also activate several other signaling pathways, including Wnt, Notch, Hippo, Hedgehog, p38/JNK mitogen-activated protein kinases (MAPKs), PI3K-Akt, NF-κB and JAK/STAT signaling pathways. Such crosstalks can be caused by direct co-activation of pathways by activated TGFβ receptors or by changing the expression of ligands, receptors or/and other components of the signaling pathways (48).

1.2.2 Negative regulation of TGFβ signal transduction

TGFβ signaling pathway at first glance appears as a straightforward signaling pathway that is driven by sequential phosphorylation events. However, the pathway is tightly regulated at every step of signal transduction. There are several major mechanisms that control duration and intensity of pathway activation.

Ubiquitin-dependent degradation. Activated TGFβ receptor complexes are targeted for lysosomal degradation in a caveolae-dependent manner (49). In addition, Smad7 recruits Smurf family E3 ubiquitin ligases to the active TGFβ receptor complex (50). This results in polyubiquitination of both TβR1 and Smad7 that are then destined for degradation (51). Because both Smad7 and Smurf2 are direct target genes of the TGFβ pathway (37, 52), this constitutes an important transcriptional negative feedback mechanism. Deubiquitinating enzymes USP4, USB11 and USP15 counteract the Smurf-induced receptor degradation and thus increase TβR1 stability and enhance TGFβ signaling (53-55). Additionally, activated Smad proteins can be Ser/Thr- and Tyr-phosphorylated at their linker domain by several members of MAP kinases (Erk1/2, JNK and p38), cyclin-dependent kinases (CDKs 2, 8 and 9), GSK3, protein kinase C, casein kinase and several others kinases (56, 57). Phosphorylated motifs are recognized by E3 ubiquitin ligases, mainly Smurf1 and Nedd4L, which polyubiquitinate Smad2 and Smad3 and target them for proteasome-dependent degradation (58, 59).

Attenuating TGFβ receptor activity. There are several negative regulators that compromise the ability of TGFβ receptors to phosphorylate downstream Smads in an ubiquitin-independent manner. The decoy receptor BAMBI (BMP and activin membrane-bound inhibitor homolog) has an extracellular domain that is highly homologous to TβR1, but has a small intracellular domain that lacks kinase activity (60).

Therefore, it forms inactive complexes with TβR2 and TGFβ ligand and prevents pathway activation. The FK506-binding protein (FKBP1A) binds to the GS domain of the TβR1 and stabilizes its inactive conformation (61). Additionally, the transmembrane protein PMEPA1 competes with R-Smads for binding to the TβR1, and limits access of Smads to TβR1-dependent phosphorylation (62). Like PMEPA1, its homologue, C18ORF1, attenuates R-Smad recruitment to the TβR1 by sequestering Smad2 and Smad3 proteins (63). Similarly to I-Smads and the Smurf family of E3 ligases, *BAMBI*, *PMEPAI*, *C18ORF1* and *FKBP1A* genes are induced upon TGFβ pathway activation and therefore comprise an essential part of the transcriptional negative feedback loops acting in the TGFβ pathway.

Signal termination by phosphatases. Several dephosphorylating enzymes attenuate the activity of the TGFβ signaling pathway. A regulatory subunit of the protein phosphatase 1 (GADD34) is recruited by Smad7 to TβR1 resulting in its dephosphorylation (64). Similarly, the PP2A phosphatase was shown to dephosphorylate the TβR1 (65). Additionally, C-terminal Ser-phosphorylation of R-Smads can be removed by several phosphatases. Here, nuclear-localized PPM1A and a DUSP family member, MTMR4 phosphatase, was proposed to act as Smad2 and Smad3 phosphatases (66, 67).

Inhibiting Smads transcriptional activity. Smad complexes require recruitment of additional DNA-binding co-factors in order to effectively activate gene transcription. Therefore, interfering with the ability of Smad complexes to bind to DNA or interact with the required DNA-binding co-factors and transcriptional co-activators comprise an additional mechanism of inhibiting the TGFβ/Smad pathway. Transcriptional co-repressors SnoN, Ski and TGIF are induced upon TGFβ pathway activation, form complexes with activated Smads and repress transcription of Smad target genes by recruiting histone deacytylases to gene promoters (68-70). Additionally, SnoN and Ski binding to activated Smad trimers destabilizes the complexes and results in their dissociation (71).

Negative regulation by miRNAs. miRNAs are small (19–25 nucleotides) noncoding RNAs that regulate the stability and translation of target mRNAs upon binding to their partially or completely complementary sequences within 5'-untranslated regions (UTRs). The TGFβ signaling pathway induces expression of a wide range of miRNAs on the one hand, and on the other hand is a target of regulation by numerous miRNAs. Expression of TGFβ receptors, ligands, Smad proteins and other pathway components is tightly regulated by microRNAs. Furthermore, miRNAs whose expression is induced upon activation of the TGFβ signaling pathway often modulate the expression of the pathway itself. Particularly, miRNA clusters 23a, 17~92 and 140-5p are induced upon TGFβ treatment (72-74), and in turn modulate the expression of type I and II TGFβ receptors as well as Smad2, Smad3 and Smad4 (73, 75, 76). Therefore, miRNAs

comprise an additional important negative transcriptional feedback loop that controls activity of the TGFβ pathway.

Such comprehensive multi-level regulation of the TGFβ signaling pathway allows broad versatility of TGFβ-driven responses in a context- and dose-dependent manner.

1.3 Biological functions of the TGFβ signaling pathway

The multifunctional nature of TGFβ pathway responses is widely acknowledged. In normal tissues, it orchestrates multiple programs contributing to tissue development and homeostasis, including processes of cell proliferation and differentiation, wound healing, inflammation, immune control, apoptosis and many others (28). Additionally, aberrant TGFβ signaling plays a central role in several pathological processes such as tissue fibrosis and cancer (77).

It also became evident that effects of TGFβ are different, often even opposite and depend much on a cell type and specific conditions. For instance, (i) TGFβ inhibits proliferation of epithelial cells, but promotes cell growth of fibroblasts; (ii) TGFβ induces stem cell-like phenotypes, but also promotes differentiation; (iii) TGFβ inhibits tumor development at early stages and drives tumorigenesis at later stages (29). Such bifunctional, context- and tissue-specific nature of TGFβ signaling underlines the pleiotropic nature of the pathway regulation.

1.3.1 Dual role in cancer

At the early stages of tumor development TGFβ pathway acts as a tumor suppressor by inhibiting cell cycle progression and/or by inducing differentiation and apoptosis. However, once tumor cells have escaped TGFβ-mediated growth inhibition, they can abuse other TGFβ-induced responses to drive metastasis, immune invasion, angiogenesis and self-renewal of cancer-initiating cells (78).

1.3.1.1 Anti-tumorigenic effects of TGFβ

TGFβ signaling pathway exerts strong tumor-suppressive effects by inhibiting cell growth, apoptosis and cellular immortalization in early tumors of epithelial, endothelial, myeloid and lymphoid origin.

Growth arrest. TGFβ signaling induces G1 arrest by inducing expression of cyclin-dependent kinase inhibitors (CDKIs), $p15^{INK4B}$ and $p21^{CIP1}$ that bind to cyclin-dependent kinases (CDKs) and inhibit their

function (79). Expression of both $p15^{INK4B}$ and $p21^{CIP1}$ is induced directly by activated Smad complexes in association with FoxO DNA-binding cofactor (80). Additionally, TGFβ induces cytostatic effects by repressing expression of cMyc, a key transcriptional factor regulating cell growth and division (81). Importantly, expression of $p15^{INK4B}$ and $p21^{CIP1}$ is repressed by cMyc activity, therefore TGFβ-induced downregulation of cMyc further contributes to the increase of CDKIs expression and cell cycle arrest (82).

Induction of apoptosis. TGFβ-mediated apoptotic responses are cell type-specific and can be triggered by both Smad-dependent and -independent mechanisms. Smad-mediated responses include transcriptional induction of the pro-apoptotic proteins Bmf and Bim (83), increase in the expression of the death-associated protein kinase (DAPK) (84) and reduced expression of the anti-apoptotic proteins Bcl-X_L and Bcl-2 as well as of the prosurvival protein survivin (85-87). Smad-independent mechanism comprise activation of the TRAF6–TAK1–JNK/p38 cascade (88), activation of the death receptor Fas induced by direct interaction of Daxx adaptor protein with TβR2 (89) and increased production of reactive oxygen species (ROS) caused by downregulation of antioxidant genes and/or increased expression of NADPH oxidase (NOX) (90).

Prevention of cellular immortalization. TGFβ signaling suppresses the expression of telomerase reverse transcriptase (TERT), the enzyme that adds telomeric DNA repeats at the end of the chromosomes (91). Activated Smad complexes associate with transcription factor E2F1, bind to the promoter of *TERT* gene and recruit histone deacetylase resulting in gene silencing (92).

1.3.1.2 Escaping the cytostatic effect of TGFβ

Tumor cells evade the tumor-suppressive effects of TGFβ either by accumulating inactivating mutations in the genes encoding TGFβ receptors and Smad proteins, or by overactivating the oncogenic signaling pathways, which override downstream TGFβ-induced growth inhibitory signals, while leaving the core TGFβ pathway components intact.

Inactivation of the signaling components of the pathway. Mutations in the *TGFBR2* gene are frequently observed in tumors with microsatellite instability (MSI). Such tumors have an impaired mismatch DNA repair machinery (93), which results in the expression of a truncated non-functional receptor protein due to insertion or deletions of adenines in the polyadenine track of the *TGFBR2* gene sequence. Such scenario is commonly observed for colorectal, gastric, pancreatic, ovarian and head and neck cancers (93-95). Mutations in the *TGFBR1* gene are less common, but are nevertheless recurrently observed in

several cancer types (96-98). Cancer cells can also downregulate the expression of TGFβ receptors by hypermethylation of their gene promoter regions (99). Mutations in genes encoding R-Smads are not frequently observed, in contrast to Smad4 that is mutated in more than half of pancreatic cancers as well as in many colorectal, esophageal, lung and liver tumors (100, 101).

Overriding the TGFβ anti-tumor responses. Instead of completely inactivating TGFβ signal transduction, tumor cells can evolve mechanisms to overcome the cytostatic effects of TGFβ by overactivating the oncogenic signaling pathways (MAPK, PI3K–Akt, Ras, cMyc), which override TGFβ-induced growth inhibitory signals (102-105). Constitutively active PI3K–Akt axis sequesters FoxO transcription factor in the cytoplasm, thus preventing its association with activated nuclear Smad complexes and subsequent induction of $p15^{INK4B}$ and $p21^{CIP1}$ genes (106). Additionally, in tumors that overexpress cMyc, it forms complex with the transcription factor Miz-1 that binds to the promoters of $p15^{INK4B}$ and $p21^{CIP1}$ and represses their expression (79).

1.3.1.3 Pro-tumorigenic effects of TGFβ

Tumors that managed to escape tumor-suppressive effects of TGFβ without inactivating core signaling components of the pathway, can use other TGFβ-mediated responses for their tumorigenic advantage. In such tumors TGFβ turns into pro-tumorigenic pathway that drives tumor cell invasion and metastasis, stimulates angiogenesis, causes local and systemic immunosuppression, enhances chemoresistance of tumor cells and boosts the self-renewal capacity of cancer-initiating cells (102, 103, 105, 107).

Invasion and metastasis. The increase in cancer cell potential to migrate and invade in response to TGFβ has long been associated with the acquisition of epithelial-to-mesenchymal transition (EMT) phenotype (108). The process of EMT is naturally occurring during various embryonic processes such as gastrulation and neural crest formation (109). Epithelial cells undergoing EMT lose tight cell–cell adhesions and epithelial markers (E-cadherin, ZO-1, claudin etc), while acquiring elongated fibroblast-like morphology accompanied by massive cytoskeleton rearmaments and upregulation of mesenchymal markers (N-cadherin, vimentin, firbonectin etc) (110). Cells that underwent EMT can revert back to epithelial phenotype during a process that is called mesenchymal-to-epithelial transition. The TGFβ cytokine is one of the most potent and well-characterized inducers of EMT. Tumor cells harboring EMT features were repeatedly reported to localize at the invasion front of the tumor (111), hence mediating cancer cell dissemination and metastasis.

Induction of a cancer stem cell-like phenotype. Tumors are composed of highly heterogeneous populations of cells with different properties and genetic backgrounds. Only a minor fraction of cells from the tumor bulk are capable of initiating a new tumor at distant sites or when inoculated into immunodeficient mice (112-114). Cancer cells with such tumor-initiating properties are often called cancer stem cells. TGFβ treatment increases the abundance of $CD44^{high}/CD24^{low}$ and $CD44^{high}/Id1^{high}$ populations in breast and glioblastoma cancers respectively, which are believed to encompass cancer stem cell properties in these tumor entities (115, 116). Additionally, such stem cell-associated markers as Sox2, leukemia inhibitory factor (LIF) and CD133 are also upregulated by TGFβ (117, 118). Interestingly, acquisition of cancer stem cell properties appears to be closely associated with TGFβ-induced EMT program as both cancer stem cell and EMT markers are co-expressed in circulating tumor cells from patients with metastatic disease (119, 120).

Angiogenesis. Tumor growth relies on the process of angiogenesis to maintain a constant supply of oxygen and nutrients as well as to enable intravasation and spread of disseminating tumor cells. TGFβ is a potent inducer of angiogenic responses in endothelial and epithelial cells by upregulation of vascular endothelial growth factor (VEGF) and connective tissue growth factor (CTGF) (121, 122). High tissue levels of TGFβ correlate with increased density of the capillary network in multiple cancer types including breast and lung cancers (123, 124).

Immunosuppression. TGFβ induces strong immunosuppressive responses by directly affecting both the adaptive and the innate immune systems, including B and T lymphocytes, natural killer cells (NK), neutrophils and macrophages (125). TGFβ can induce apoptosis in both T and B cells as well as inhibit their proliferation and activation (126-128). Additionally, TGFβ inhibits the production of key components that confer T cell cytotoxicity such as granzymes A and B, perforin, Fas ligand and interferon-γ (129, 130). Macrophages exposed to TGFβ downregulate the expression of key pro-inflammatory chemokines including macrophage inflammatory proteins 1α and 2 (MIP-1α and MIP-2), interleukins IL-1β, IL-8 and IL-10, and CXCL1 chemokine that combined result in impaired macrophage activation and initiation of the immune response (131).

Chemoresistance. Tumor cells that underwent TGFβ-induced EMT show higher resistance to conventional cytotoxic and targeted therapies. For instance, high expression of EMT markers in tumors is associated with a worse clinical outcome and limited response to the anti-EGFR and cisplatin therapy in NSCLC patients (132-135). Similar correlations are also commonly observed in other cancer types such as melanoma, pancreatic, and head and neck cancers (136-138). Enrichment of tumor cells with stem

cell-like properties upon undergoing TGFβ-induced EMT is believed to be the main reason of such acquired and innate resistance to chemotherapy (139). Mechanistically, chemotherapy resistance of cancer stem cells is mediated by decreased proliferation rate as well as upregulated resistance-related and DNA repair machinery genes (140, 141).

1.3.2 Targeting TGFβ in clinical settings

Given the importance of TGFβ signaling in tumor progression, multiple therapeutic approaches have been developed to target the pathway (**Figure 1.4**). Such approaches include inhibitors of *TGFB1* gene expression, anti-sense oligonucleotides targeting *TGFB1* and *TGFB2* mRNAs, antibodies against TGFβ ligands or receptors as well as small molecule inhibitors of TβR1 kinase domain.

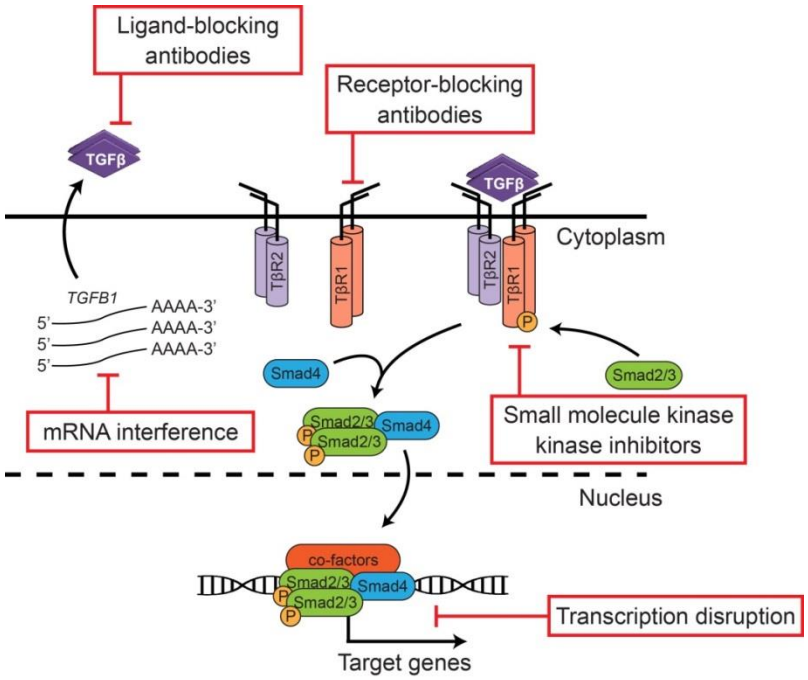

Figure 1.4. Intervention points used in anti-TGFβ therapy. Red boxes indicate molecular targets and processes of TGFβ production and signaling.

However, development of TGFβ inhibitors for clinical use proved to be difficult as none of the suggested targeted approaches and developed drugs was approved for patient treatment outside of the clinical trials. One of the main concerns of TGFβ blockade is the off-target effects. Because TGFβ effects are highly tissue-specific and have dual role in tumorigenesis, complete inhibition of the pathway raises multiple concerns. For instance, *TGFB1* knockout mice demonstrated severe inflammation and vascular disorders (142, 143), while other studies reported that TGFβ inhibition may awake dormant metastatic

tumor cells and promote de novo neoplasm formation (144, 145). Moreover, small molecule inhibitors developed to target TβR1 kinase domain also affected closely related receptors of the BMP branch. Surprisingly, despite all these concerns, anti-TGFβ drugs appear relatively safe with less toxicity than other currently available anti-cancer therapies (146-148). It is also now evident that TGFβ inhibition alone is unlikely to cause major anti-tumor responses, as it is not cytotoxic per se, but rather disinhibits the immune systems and limits cancer cell metastatic potential. Therefore, finding best drug combinations for each oncology setting is an important goal for the future of anti-TGFβ therapy. Immune checkpoint inhibitors appear as one of the most promising potential combinations with anti-TGFβ drugs (149, 150). Similarly to immunotherapy, identification of predictive biomarkers for anti-TGFβ therapy to help stratify the patients, which are most likely to benefit from such therapy, is a growing need for TGFβ inhibitors (151, 152). Finally, developing new drugs targeting tissue-specific components of the TGFβ pathway as well as its downstream effectors would further allow reducing the cytotoxicity and optimizing the treatment.

1.3.3 TGFβ in lung cancer

Early metastasis and therapy resistance are the main features that result in high mortality among lung cancer patients. Both features are attributed to cancer cells undergoing EMT and acquiring more invasive phenotype with cancer stem cell properties. EMT features are observed in the majority of lung cancer tumors (153). There is growing evidence that deregulated TGFβ signaling contributes to the acquisition of the EMT phenotype by tumor cells in the lung cancer context. Numerous studies reported elevated TGFβ plasma levels in lung cancer patients (124, 154). Moreover, TGFβ1 levels significantly correlate with angiogenesis, tumor stage and overall survival in patients with non-small-cell lung cancer (124, 155). Upregulation of multiple EMT-initiating transcription factors such as Zeb1/2, Snai1, Slug, Twist1/2, is frequently observed in lung cancer especially in the invading tumor margin (156). Such upregulation correlates with a lower response to treatment and reduced overall survival (157-161). Additionally, expression of downstream EMT effectors such as matrix metalloproteinases (MMPs), vimentin, E- and N-cadherins is routinely reported to be altered in lung cancer (162-164). Therefore, lung tumors appear to retain a functional TGFβ signaling cascade, mitigate its tumor-suppressive effects and use it to boost their metastatic potential and drug resistance. Indeed, several studies have demonstrated that the majority of lung cancer cell lines are not growth-inhibited when exposed to TGFβ (165, 166). However, there are also contradictory reports suggesting that lung tumors downregulate TβR2 to drive their tumorigenicity (167, 168). In line with it, the non-responsiveness to TGFβ-induced

growth arrest of lung cancer cell lines was suggested to be mediated by reduced expression or complete loss of TβR2 (165, 166, 169). Moreover, TβRII downregulation increased invasiveness of NSCLC cell lines (170, 171), while TβRII restoration reduced proliferation, anchorage-independent and xenograft growth (167). Therefore, a better mechanistic understanding of the TGFβ pathway biology in the context of lung cancer is essential for addressing the major challenges of lung cancer such as early metastasis and therapy resistance.

1.4 Systems biology

Conventional biological studies have been performed by focusing on individual molecules, cells, tissues, organs, or organisms. However, properties of a system can never be inferred by a simple sum of the properties of the discrete elements. One of the aims of systems biology is to understand how components within a cell or cells within an organ dynamically interact in a coordinated fashion in order to fulfill certain specialized functions, e.g. signal transduction or gene expression (172, 173). A static representation of a biological network cannot account for the dynamic complexity of the system and will not be able to explain properties emerging at the systems level. Therefore, a mathematical modeling approach is necessary to infer the dynamic behavior of biological processes.

1.4.1 Modeling approaches

Analysis of biological networks can be performed by two different strategies (**Figure 1.5**). Top-down approaches rely on high-throughput data to infer the influences, connections and the information flow within the biological networks. Such mathematical models require minimal prior biological knowledge as mainly statistical modeling methods such as clustering, principle component and regression analyses are used. In contrast, bottom-up approaches are based on extensive pre-existing biological knowledge to build up a model that describes a dynamic behavior of a small network such as signal transduction pathway. Precise mechanistic and dynamic insights can be obtained in such cases using deterministic ordinary-differential equations-based models, or stochastic models (174). The choice of the modeling approach depends on the data available and the particular question of interest (175).

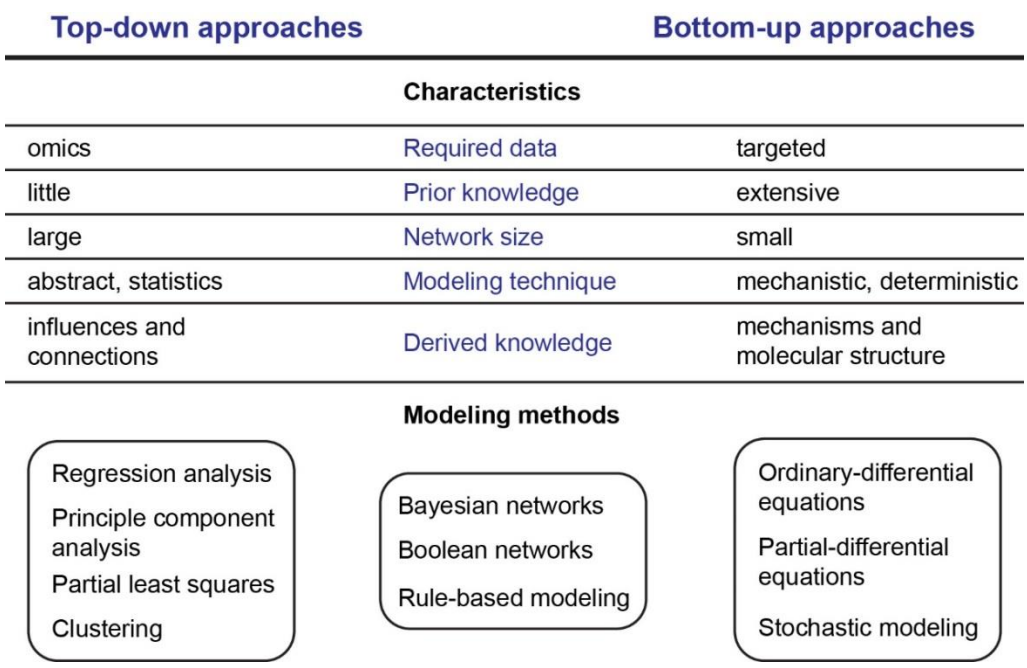

Figure 1.5. Modeling approaches in systems biology. Modeling methods can be globally subdivided into top-down and bottom-up approaches. Each requires different type of data and prior knowledge, and allows inferring different properties of the system. Boxes indicate exemplary modeling methods that can be applied for either of the approaches. Adapted from Edda Klipp (176).

1.4.2 Coupling of mathematical modeling and experimental data generation

The combination of experimental data generation and mathematical modeling provides a powerful tool for revealing regulatory mechanisms of the dynamic system (177). The existing experimental data and biological knowledge are used to establish mathematical models, which are calibrated on the data. Models that are able to describe the existing data are used to make *in silico* prediction of systems behavior under certain stimuli and perturbations. If new experimental data contradicts with the model predictions, the model structure or parameters have to be changed, until it can describe the data. Each cycle of this iterative process of experimental data generation and mathematical modeling gradually improves model reliability and its predictive power, ultimately providing the insights to experimentally unapproachable aspects of a biological system (**Figure 1.6**).

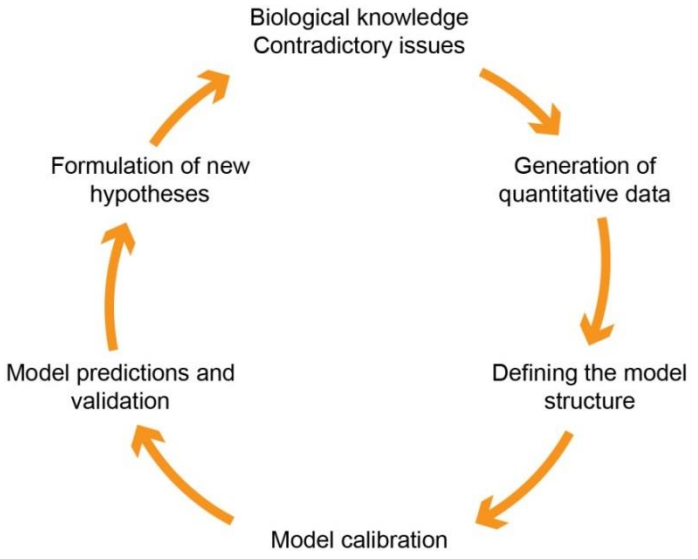

Figure 1.6. Iterative cycle of hypothesis formulation, experimental data generation and modeling in systems biology. New hypotheses and unanswered questions are examined by iterative cycles of quantitative data generation, establishment of the mathematical models with a structure according to the existent knowledge, model calibration and validation. Contradictions between model predictions and experimental validation results in the model refinement structure and obtaining new biological insights about the system. Adapted from Kitano (172).

1.4.3 Mathematical models of the TGFβ signaling pathway

The major signaling components of the TGFβ signaling pathway were identified decades ago. However, it became apparent that despite appearing as relatively simple and linear pathway, it is difficult to explain numerous pleiotropic effects induced by TGFβ without comprehensive understanding of how the signal is encoded and transmitted within the network. Consequently, multiple mathematical models of the TGFβ pathway were developed to address the complex dynamic properties of the pathway.

Receptor endocytosis. TGFβ receptor trafficking is believed to play a crucial role in mediating TGFβ signaling events. Several ODE-based models addressed the importance of the TGFβ receptor endocytosis by examining the connection between TGFβ receptor activity and its subcellular localization. The model of Vilar et al. considered the following components: ligand, type I and type II TGFβ receptors, activated receptor complexes and possible subcellular compartments: plasma membrane and endosomes (178). Zi and Klipp further extended the model structure by including downstream Smad activation and additional compartment of lipid-raft caveolae that mediates receptor degradation (179). The models predicted that a ratio between different receptor pools defines the activity of the pathway and suggested cell type-specific differences in receptor trafficking that explain variations among experimental datasets from different studies (49, 180).

Smad nuclear-cytoplasmic shuttling. Smad nuclear accumulation is a key step in inducing TGFβ responses. Several ODE-based models aimed to understand the kinetics of Smad nuclear import and

export, and the driving mechanisms of Smad nuclear retention (181, 182). Both models demonstrated that imbalance between the rates of cytoplasmic Smad phosphorylation and nuclear dephosphorylation is a driving force in Smad nuclear accumulation. Additionally, models demonstrated that there is no need for adaptor proteins that sequester Smads in the nuclear compartment as altering the phosphorylation/dephosporylation ratio was sufficient to explain all the experimental data.

Signal attenuation. Upon receptor activation downstream Smad2/3 phosphorylation peaks at about 1 hour after TGFβ treatment and declines afterwards (183). Several ODE-based models were proposed to explain this signal attenuation. A model of Clarke et al. suggested that TGFβ ligand depletion is the principal determinant of Smad signal duration and cells sense TGFβ levels by its constitutive uptake using type II TGFβ receptor (184). In contrast, Vizan et al. demonstrated that the dynamics of the TGFβ receptors on the cell surface is a key determinant of the signal attenuation and pathway dynamics. Ligand treatment induced rapid depletion of the competent surface receptors resulting in desensitized cells from repeated TGFβ stimulations (185). Finally, the authors claimed that pathway attenuation is independent of TGFβ target gene expression and is mediated by constitutively active proteasome-dependent degradation of the activated receptor. Subsequently, Khatibi et al. developed a model that included Smad7/Smurf and miR-433/Azin1 axes as negative and positive feedback loops respectively (186). The obtained model was able to explain sigmoidal, switch-like behavior of dose-response treatments that is observed in certain cellular systems (187).

Induced phenotypic responses. Mechanistic understanding of how variable TGFβ ligand doses are converted into cell fate decision remain poorly understood. Zhang et al. developed a model of to elucidate the underlying mechanism of TGFβ-induced EMT (188). Authors provide evidence that EMT process is executed as a sequential two-step program controlled by two double-negative transcriptional feedback loops. The Snail1/miR-34 feedback loop controls the initiation of the EMT, while Zeb1/miR-200 feedback loop tightly controls the establishment of the mesenchymal state. Interestingly, authors suggest existence of the metastable intermediate state, from which cells can still revert back to the epithelial phenotype, while transition to the mesenchymal state is irreversible as the positive autocrine TGFβ/miR-200 feedback loop is established to maintain the mesenchymal state.

The above mentioned mathematical models despite shedding the light on certain dynamic properties of the TGFβ pathway, had a number of shortcomings. First, majority of the models assumed comprehensive model structures, but used a limited set of experimental data for model calibration. As a result, majority of the rate constant were not defined based on experimental data of the given model

systems, but manually fixed to certain values that were considered as realistic by authors. For examples, the mathematical models of Vilar et al. (178) and Vizan et al. (185) considered existence of type I and type II TGFβ receptors in their model structure, although there was either no data on the receptor level acquired or it was not used for model calibration. Next, neither of the models used explicit methods to demonstrate identifiability of the developed models. Identifiability of model parameters is highly desired as only a model with majority of identifiable parameters can make prediction about dynamic behavior of model species that are not experimentally measured. Finally, all of the above mentioned models used experimental data produced only in one cell line. Therefore, cell type-specific differences in the pathway regulation could not be addressed.

1.5 Objectives

In order to comprehensively examine the importance of TGFβ signaling pathway in the context of lung cancer and to obtain better insights into regulatory processes controlling TGFβ pathway dynamics, the following aims were pursued in this thesis:

1. comprehensive examination of the status of TGFβ signal transduction pathway in tissue samples of lung cancer patients to identify possible mechanisms of TGFβ deregulation in lung cancer;
2. revisit potential mechanisms of TGFβ-mediated pro-tumorigenic effects in lung cancer;
3. establish an ODE-based mathematical model of the TGFβ signaling pathway to obtain mechanistic insights into its regulation.

The presented work provides insights into TGFβ-induced molecular machinery mediating cancer cell invasion and chemoresistance as well as reports biomarkers for identifying lung cancer patients with particularly aggressive disease. It also uncovers new mechanisms of TGFβ regulation that might facilitate the discovery of novel therapeutic strategies for targeting the pathway.

2 Results

2.1 Mechanisms causing TGFβ pathway deregulation in lung cancer

The results reported in this subsection have been previously published in their original or modified form in Marwitz*, Depner*, Dvornikov* et al. 2016 (189).

2.1.1 TGFβ pathway is altered in human lung tumors

To examine the status of the TGFβ signaling pathway in the context of lung cancer, immunohistochemical analysis (IHC) was used to assess the protein expression of the key TGFβ pathway components in tissues from 133 patients with non-small-cell lung cancer (**Figure 2.1A**) and in 23 tumor-free lung samples (**Figure 2.1B**). Out of those tumor-free specimens, four (17.4%) were matched samples for NSCLC lung cancer tissues. The presence of TGFβ signaling components was analyzed in lung cancer cells and compared to the expression in the type II alveolar epithelial cells (AECII) of the tumor-free tissues (**Figures 2.1C and 2.1D**). This cell type is considered to be a possible origin of adenocarcinomas (190), and has been recently discussed to exhibit features of progenitor cells (191).

The TGFβ ligand was detected in the majority of the lung cancer tissues (85%) but only in 34.7% of the AECII from the tumor-free samples. Weak staining for Smad2 and Smad3 was observed in 22.6% and 11.3% of the lung cancer samples, respectively, whereas in the AECII, Smad3 was not detectable by means of IHC, and Smad2 was present in 17.4% of the samples. For the majority of the lung cancer samples, Smad2 (78.2%) and Smad3 (87.2%) phosphorylation, indicative of pathway activation, was observed. In contrast to this, Smad2 and Smad3 phosphorylation was only present at low levels in 17.3% of the examined AECII. Smad4 was widely expressed in both lung cancer cells (71.4%) and AECII (60.8%). Similarly, SnoN was detected in the cytoplasm of almost all the lung cancer specimens (98.5%) as well as in the AECII (87%). Protein expression of the negative regulator Smad7, a direct target gene of TGFβ signaling, was detected in almost all the lung cancer samples (99.2%) and was primarily localized in nuclear regions. In the AECII, Smad7 was only moderately expressed (34.8%). Surprisingly, the protein expression of another negative regulator of TGFβ signaling, the TGFβ pseudo-receptor BAMBI, was almost completely absent in the lung cancer tissues (1.5%) but frequently detected in the AECII (30.4%). As assessed by Fisher's exact test, a statistically significant difference in the protein expression of TGFβ, pSmad2, pSmad3, Smad3, Smad7, SnoN and BAMBI was observed in the lung cancer cells compared to the AECII (**Table S6.1**). Furthermore, the frequency of pathway activation, as indicated by the presence

of pSmad2 and pSmad3 in the same sample, was significantly higher ($P \leq 0.001$) in the lung cancer tissues compared to the tumor-free lung tissues.

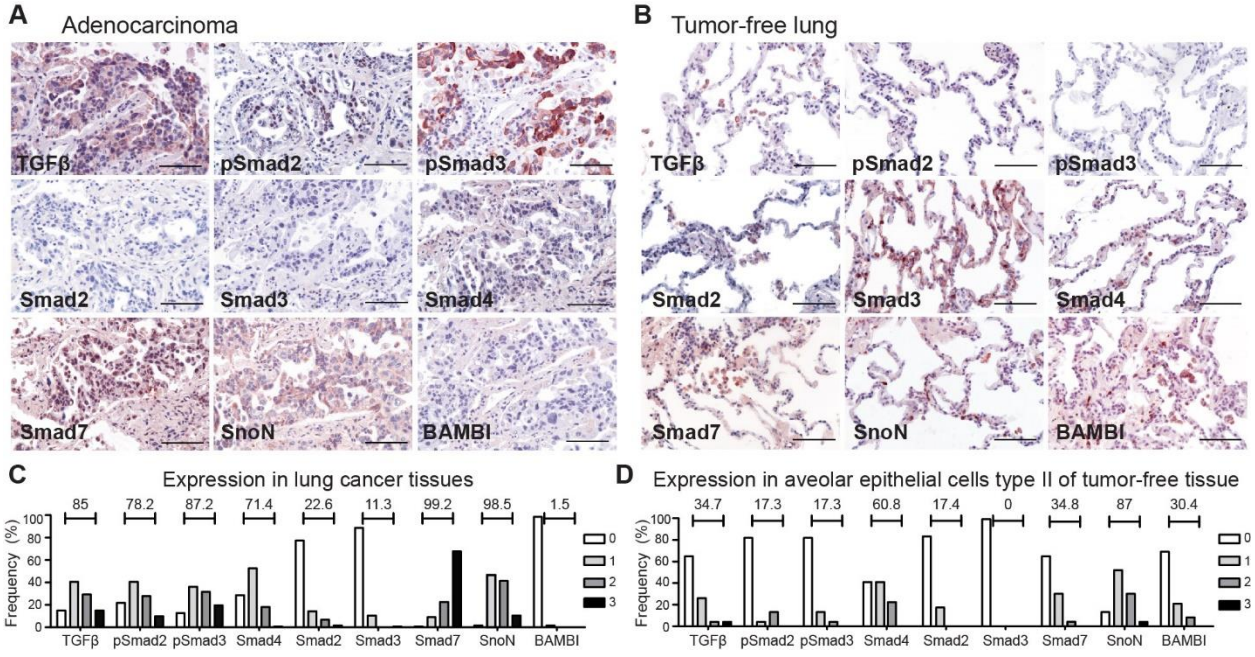

Figure 2.1. TGFβ/Smad signaling pathway is overactivated in the lung tumor tissues alongside with a complete loss of BAMBI. Detection and localization of TGFβ pathway components via immunohistochemistry in fixed paraffin-embedded lung adenocarcinoma (**A**), and tumor-free lung tissues (**B**). All the images are at 40× magnification. Scale bar corresponds to 100 mm. Positive staining is indicated by a red color (AEC). For each antibody, a positive signal was observed for at least some of the samples. Representative images are shown for tumor and tumor-free lung tissue. (**C** and **D**) Scoring of expression levels in lung cancer tissues (n = 133 patients) and in healthy AECII from tumor-free lung tissue (n = 23 patients), respectively. Bar charts indicate semi-quantitative scores based on the histologic analysis of the entire specimen as follows: negative (0), focal and weak expression (1), frequent intermediate expression (2), strong expression and dominating feature of specimen (3). Numbers above the bars display the total positive cases observed overall in percentage. Data generated by Sebastian Marwitz (Research Center Borstel). The figure is adapted from Marwitz*, Depner*, Dvornikov* et al. 2016 (189).

2.1.2 Differential expression of TGFβ-regulated genes in human lung cancer and tumor-free lung tissues

The observed increased activation of TGFβ signaling in lung cancer suggested concomitant alterations at the transcriptional level. Therefore, the mRNA expression of genes encoding TGFβ core pathway members in 19 matched pairs of tumor-free lung tissues and macro-dissected lung NSCLC tumors was analyzed using qRT-PCR.

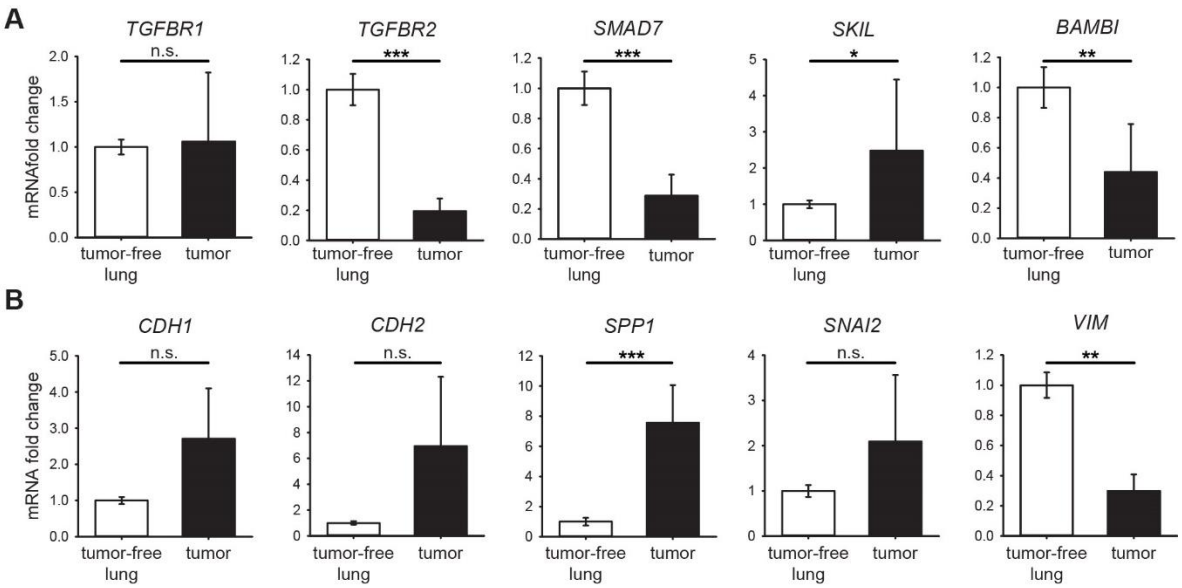

Figure 2.2. TGFβ-regulated genes are differentially expressed in human lung cancer tissues and tumor-free lung tissues. Nineteen samples of HOPE-fixed paraffin-embedded tissues from matched lung cancer and tumor-free lung samples were macrodissected and RNA was extracted. Expression of TGFβ pathway components (**A**) and downstream EMT genes (**B**) was analyzed using qRT-PCR. Statistical analysis by Wilcoxon Signed Rank Test with *, $P \leq 0.05$, **, $P \leq 0.01$ and ***, $P \leq 0.001$ regarded as significant, n.s. not significant. Data generated by Ruth Merkle (DKFZ, Heidelberg). The figure is adapted from Marwitz*, Depner*, Dvornikov* et al. 2016 (189).

Significant downregulation of genes encoding core components of the TGFβ signaling pathway, such as *TGFBR2*, *SMAD7* and *BAMBI*, was observed in the lung cancer tissues (**Figure 2.2A**). For *BAMBI*, the downregulation of its mRNA corresponded well with the reduced expression of the BAMBI protein in the lung cancer samples (**Figure 2.1**). The divergence between *SMAD7* mRNA and protein levels might be due to differences in post-translational regulation in tumor and healthy tissue. Possibly, since *SMAD7* mRNA is targeted by multiple miRNAs (192), protein translation of *SMAD7* mRNA is inefficient in healthy tissue or proteasomal degradation of Smad7 mediated e.g. by the E3 ubiquitin ligase Cbl (193) might be impaired in lung cancer cells resulting in elevated Smad7 protein levels despite reduced mRNA expression. In contrast, *SKIL* was upregulated in tumor samples (**Figure 2.2A**). As *SKIL* is a direct TGFβ target gene, its higher expression might result from the pathway overactivation in the tumor context (**Figure 2.1**). No significant differences between the tumor and tumor-free samples were observed for the intracellular signaling mediators *SMAD2*, *SMAD3*, *SMAD4*. Additionally, altered expression of several downstream TGFβ-inducible genes was observed (**Figure 2.2B**). Mesenchymal markers *SPP1* and *SNAI2* were upregulated, while *CDH2* and *CDH1* remained unchanged. Interestingly, reduced expression of the classical mesenchymal marker *VIM* was also observed. Such mixed pattern of EMT markers expression was reported for the aggressive hybrid subpopulation of NSCLC cancer cells (194). Overall, significant

alterations at the transcriptional level of TGFβ pathway were observed. In line with the absence of the negative regulator BAMBI protein in lung tumor tissues, several downstream TGFβ target genes demonstrated elevated expression levels.

2.1.3 Altering BAMBI expression affects TGFβ signaling in NSCLC cell lines

A striking feature of the examined lung cancer samples was the absence of the BAMBI protein as well as its reduced mRNA expression. This was confirmed by the observation that the amount of *BAMBI* mRNA was significantly lower in the NSCLC cell lines compared to the levels detected in healthy AECII (**Figure 2.3A**). To obtain insights into mechanisms whereby the loss of BAMBI might contribute to tumor progression, BAMBI expression in the NSCLC cell lines was reconstituted using a retroviral TET-On system that facilitates the inducible expression of BAMBI-GFP or GFP alone. This resulted in 20 and 100 times higher BAMBI expression level in A549 and H1975 cells, respectively, compared to AECII cells (**Figure 2.3B**). The reconstitution of BAMBI in the H1975 cells caused a considerable decrease in Smad2 and Smad3 phosphorylation at all the TGFβ concentrations used for stimulation (**Figures 2.3C and 2.3D upper panel**), while in the A549 cells, a decrease in Smad2 and Smad3 phosphorylation was observed at low TGFβ concentrations (**Figure 2.3D lower panel**). To determine whether the reconstitution of BAMBI also alters the transcription of downstream TGFβ-inducible genes, the mRNA expression of several TGFβ-inducible EMT genes was examined over a course 48 hours after TGFβ stimulation. Marked downregulation of *CDH1* (E-cadherin), *CDH2* (N-cadherin), and *SNAI2* gene expression was observed in both BAMBI-reconstituted A549 and H1975 cell lines (**Figure 2.3E**). Additionally, siRNA-mediated BAMBI knockdown was performed in A549 and SK-MES1 lung cancer cell lines that demonstrated intermediate levels of *BAMBI* mRNA expression in comparison to AECII (**Figure 2.3A**). Knockdown using two different BAMBI siRNAs resulted in 80–90% reduced *BAMBI* expression in both cell lines (**Figure 2.4A**). BAMBI downregulation resulted in higher Smad2 and Smad3 phosphorylation and enhanced target gene expression upon TGFβ stimulation in both, A549 and SK-MES1 cells (**Figures 2.4C and 2.4D**).

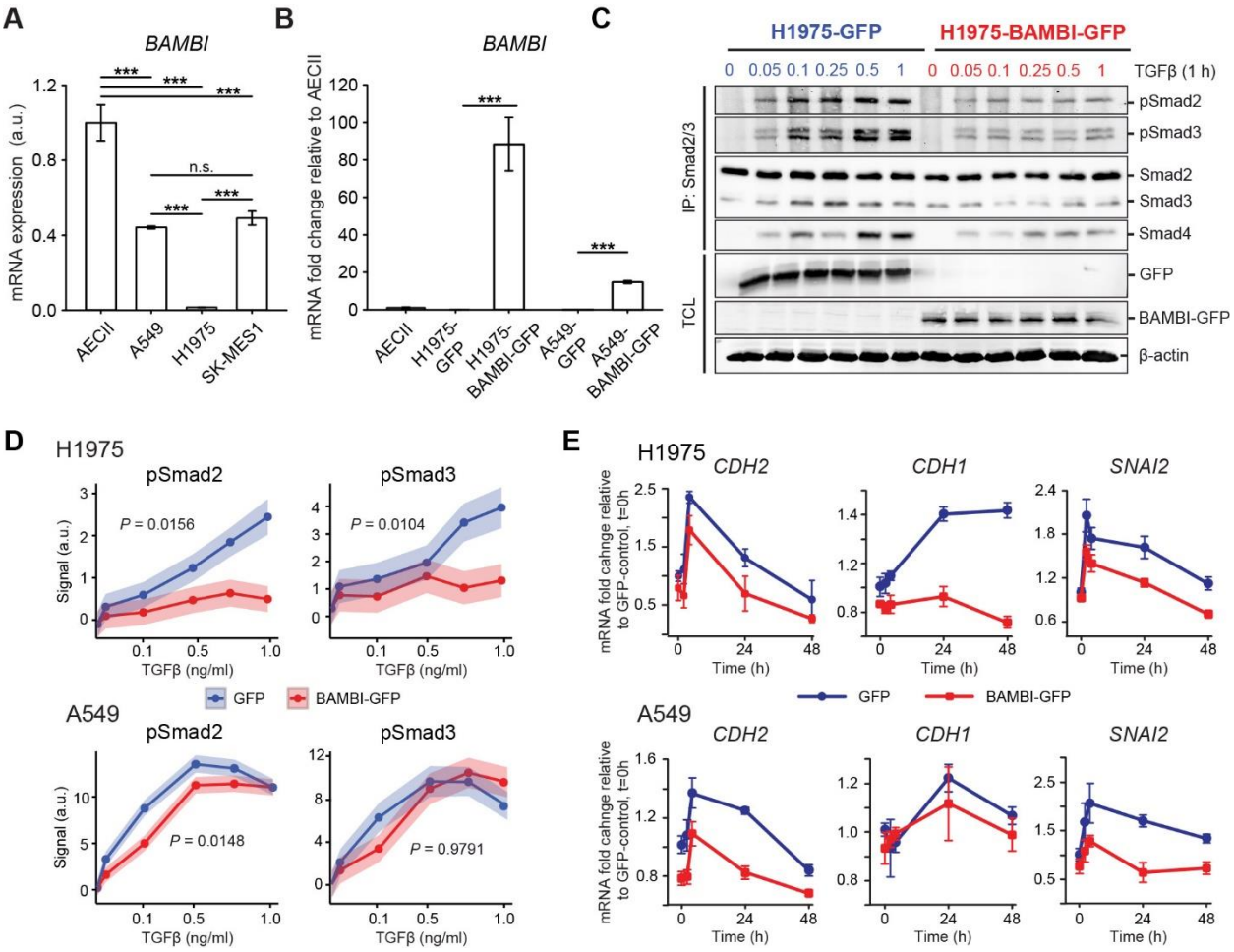

Figure 2.3. BAMBI overexpression dampens TGFβ signaling in NSCLC cell lines. (**A**) Relative expression of *BAMBI* mRNA in the indicated lung cancer cell lines in comparison with healthy AECII. The mean ± SD of qRT-PCR determinations from three AECII isolations and from three biologic triplicates of the lung cancer cell lines are shown. Statistical analysis was performed using one-way ANOVA test, with ***, $P \leq 0.001$ regarded as significant; n.s., not significant. (**B**) Relative expression of *BAMBI* mRNA in DOX-treated NSCLC cell lines in comparison with healthy AECII. Data represent the mean from four biologic replicates ± SD. Statistical analysis was performed using one-way ANOVA test, with ***, $P \leq 0.001$ regarded as significant. (**C**) Representative immunoblot of H1975 cells stably transduced with inducible vectors containing GFP or BAMBI-GFP were activated by addition of DOX for 24 h and stimulated with indicated doses of TGFβ for 1 h. Levels of pSmad2/3, total Smad2/3 and Smad4 were assessed by immunoprecipitation (IP) of total proteins and followed by immunoblotting against phosphorylated and total species. The level of GFP and BAMBI-GFP in total cell lysates (TCL) was monitored with immunoblotting. Actin was used as a loading control. (**D**) Quantification of TGFβ dose-dependent phosphorylation of Smad2 and Smad3 in H1975-GFP and H1975-BAMBI-GFP as well as in A549-GFP and A549-BAMBI-GFP cells. For each cell line, the Smad2/3 phosphorylation was determined by quantitative immunoblotting. The data shown are the mean of three biologic replicates. The shaded area indicates the SEM. Statistical analysis was performed using two-way ANOVA with repeated measurements, and $P \leq 0.05$ was considered significant. (**E**) Expression of the indicated EMT genes in H1975 and A549 cell lines stably transduced with GFP or BAMBI-GFP was assessed by qRT-PCR. The GFP and BAMBI-GFP expression was induced with DOX for 48 hours, and cells were stimulated with TGFβ for the indicated time points. mRNA levels were normalized using the geometric mean of the β-glucuronidase (*GUSB*) and esterase D (*ESD*) housekeeping genes. The experiments were performed in six biologic replicates, and the data represent mean values ± SD. qRT-PCR data produced by Ruth Merkle (DKFZ, Heidelberg). The figure is adapted from Marwitz*, Depner*, Dvornikov* et al. 2016 (189).

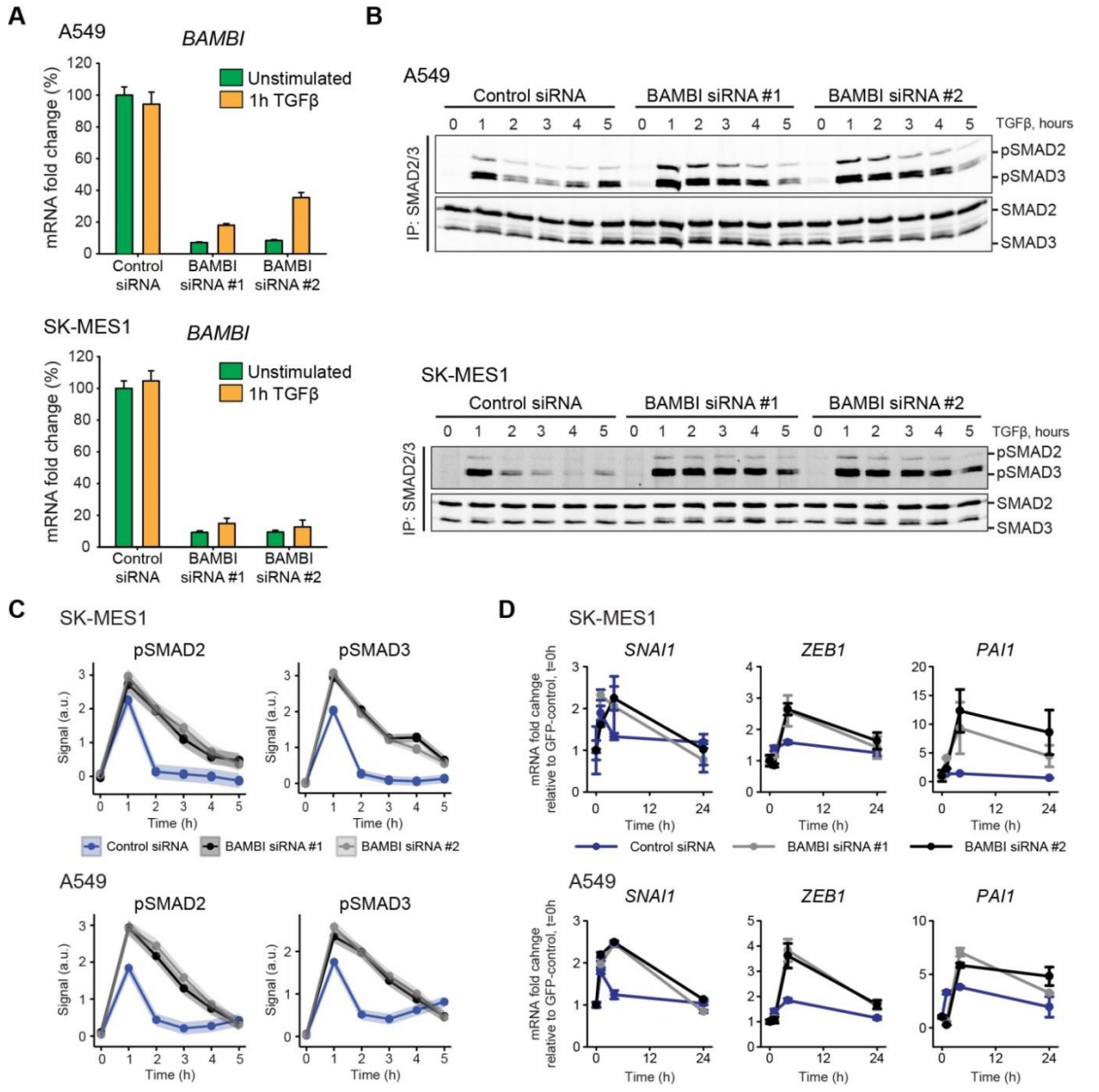

Figure 2.4. siRNA-mediated knockdown of BAMBI expression in NSCLC cell lines enhances TGF-β-induced signaling. (**A**) Validation of siRNA knockdown efficiency using qRT-PCR in A549 and SK-MES1 cells. After 36 hours of siRNA transfection cells were stimulation for 1 hour with TGFβ or left untreated. mRNA was extracted and the efficiency of BAMBI knockdown was analyzed using qRT-PCR. Data represent mean ± SD from 5 independent experiments. (**B**) Representative immunoblots of Smad2/3 phosphorylation dynamics upon BAMBI downregulation in A549 and SK-MES1 cells, respectively. Cells were transfected with two different siRNAs against BAMBI or control siRNA for 36 hours and then stimulated with 1 ng/ml TGFβ for indicated time points. (**C**) Quantification of the dynamic behavior of TGFβ-induced Smad2/3 phosphorylation upon BAMBI knockdown in A549 and SK-MES1 cells. For each cell line, the data shown are the mean of three independent experiments, and the shaded area indicates the SEM. (**D**) Expression of the indicated EMT genes in A549 and SK-MES1. Cells were transfected with BAMBI-specific siRNAs or control siRNA for 36 hours, stimulated with 1 ng/mL TGFβ, and mRNA expression was assessed by qRT-PCR. RNA levels were normalized using the geometric mean of the *GAPDH* and *G6PD* housekeeping genes. Data shown represent mean ± SD from three independent experiments. The figure is adapted from Marwitz*, Depner*, Dvornikov* et al. 2016 (189).

2.1.4 BAMBI reconstitution in lung cancer cells leads to reduced invasion and tumor growth

To determine the effects of BAMBI reconstitution on cellular responses, the TGFβ-induced migration and invasion of H1975-BAMBI-GFP cells and control H1975-GFP cells were analyzed. In a 2D migration assay, the TGFβ treatment resulted in increased speed (from 2.5 to 3.3 µm/h) and persistence (from 0.275 to 0.425) of cellular movement in control cells, while in the BAMBI-overexpressing cells the increase was almost entirely abrogated (**Figure 2.5A**). Furthermore, TGFβ treatment resulted in a three-fold increase of number of invaded H1975-GFP cells in a 3D collagen invasion assay, while in BAMBI-reconstituted cells such increase was not observed, suggesting that the silencing of BAMBI increased the potential of cells to invade in response to TGFβ stimulation (**Figure 2.5B**). Further, the impact of BAMBI loss-of-function on cancer cell invasion was examined. To achieve this, BAMBI siRNA-mediated knockdown in the squamous lung cell carcinoma cell line SK-MES1 that harbors higher basal expression of *BAMBI* mRNA than the adenocarcinoma cell line H1975 was performed. The knockdown resulted in increased invasion of unstimulated cells and importantly enhanced TGFβ-induced invasion for at least one of the siRNA used (**Figure 2.5B**).

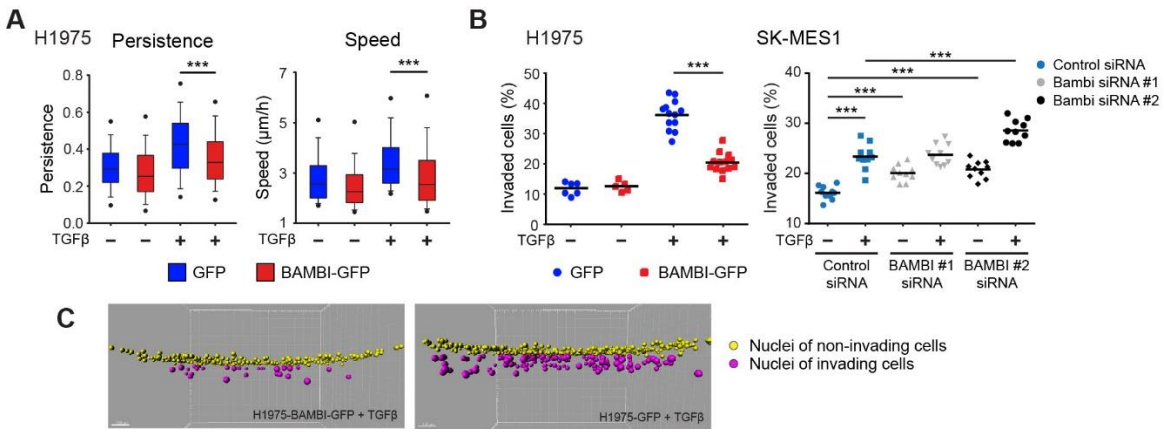

Figure 2.5. Reconstitution of BAMBI expression in lung cancer cells reduces TGFβ-mediated invasion capacity *in vitro*. (**A**) Persistence and migration speed of H1975-GFP and H1975-BAMBI-GFP cells, stimulated with TGFβ and imaged for 22 hours. The box is bound by the 25th and 75th quantiles. The whiskers extend to three-halves of the interquartile range. The lines indicate the median, and dots illustrate the 5th and 95th quantiles. Each box contains at least 350 cells from two independent experiments, nine biologic replicates in total. Statistical analysis was performed using the Mann–Whitney rank-sum test; ***, $P \leq 0.001$. (**B**) Quantification of the number of H1975 cells with BAMBI overexpression and SK-MES1 cells with BAMBI knockdown that invaded into the collagen gel. Every dot corresponds to one biologic replicate; black line is the median. Statistical analysis was performed using one-way ANOVA, with ***, $P \leq 0.001$ regarded as significant. (**C**) Representative reconstructed 3D images of collagen-invaded TGFβ-stimulated H1975-GFP and H1975-BAMBI-GFP cells. 3D invasion data of SK-MES1 cells are generated by Magdalena Szczygieł (DKFZ, Heidelberg). The figure is adapted from Marwitz*, Depner*, Dvornikov* et al. 2016 (189).

To investigate the influence of enhanced BAMBI expression on the metastatic potential and tumor forming capacity *in vivo*, both A549-GFP control and A549-BAMBI-GFP cells were injected into the tail veins of nude mice. The mice were kept in the presence of doxycycline (DOX) to ensure the expression of GFP or BAMBI-GFP, and the TGFβ ligand was administrated to facilitate cancer cell invasion. Per group twelve animals were injected and kept for ten weeks unless dropout criteria were observed, and mice were sacrificed earlier. In the GFP group two mice that were sacrificed pre-maturely and two mice that survived until the planned end-point of the experiment, developed histologically-confirmed tumors within the lungs. In the BAMBI-GFP cohort lung lesions were observed in one pre-maturely sacrificed mouse and in three mice that survived until the end-point. Overall four mice per group developed lung cancer. Macroscopic investigations of the dissected lungs showed that A549-BAMBI-GFP mice developed fewer lung lesions compared to A549-GFP mice (**Figure 2.6A**).

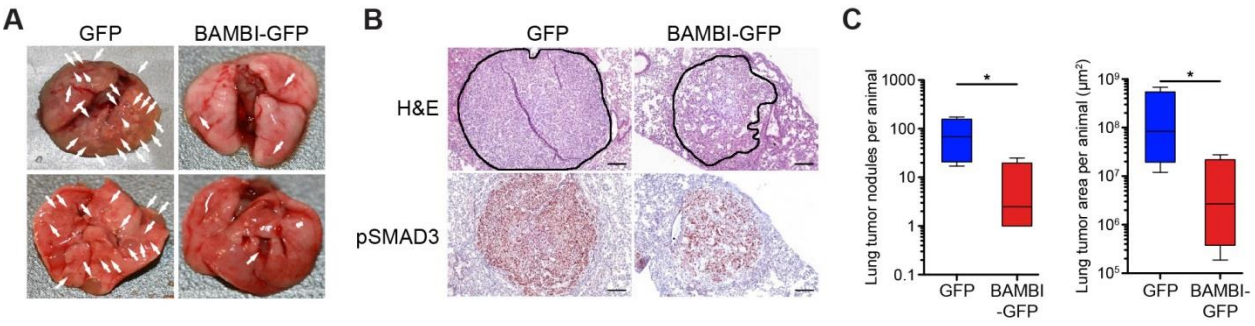

Figure 2.6. Reconstitution of BAMBI expression in lung cancer cells reduces TGFβ-mediated invasion capacity *in vivo*. (**A**) Representative images of mouse lungs nine weeks after tail vein injection of A549-GFP or A549-BAMBI-GFP cells. Lung macrometastases are indicated with white arrows. (**B**) Histologic analysis of lung tumor burden in mice injected with A549-GFP or A549-BAMBI-GFP. Lung tumor area within the H&E-stained tissue section of animal lungs was quantified using Infinity Analyze software. Exemplary images of tissue sections from A549-GFP- and A549-BAMBI-GFP–injected animals are shown, and lung tumors are manually marked by black borders (top plots). Activity of the TGFβ pathway was determined by IHC detection of pSmad3 (bottom plots). All images are taken at 10× magnification. Scale bar is 200 µm. (**C**) Quantification of human lung tumor nodules and lung tumor areas within animal lungs after tail vein injection of A549-GFP and A549-BAMBI-GFP cells. Tumor nodules were counted on H&E-stained sections from each lung of every animal that developed histology-confirmed lung tumors (n = 4 each). The total area of lung tumor per animal as determined by image analysis on H&E-stained sections (n = 4 each). All data are displayed as box and whiskers plot showing the median and minimum/maximum. For statistical evaluation of nonparametric data, the Mann–Whitney test (one-tailed) was applied and $P \leq 0.05$ (*) was regarded as significant. IHC stainings produced by Sebastian Marwitz (Research Center Borstel). The figure is adapted from Marwitz*, Depner*, Dvornikov* et al. 2016 (189).

Histological diagnosis revealed adenocarcinomas in the lungs of both groups (**Figure 2.6B**) and qRT-PCR analysis confirmed the presence of human A549 cells expressing either GFP or BAMBI-GFP (**Figure S6.1**). To determine the influence of DOX-induced GFP or BAMBI-GFP expression on the metastatic potential of A549 cells, the total amount of lung tumor nodules per animal was quantified. Mice injected with GFP-

expressing A549 cells showed a median of 68.5 (17 minimum, 174 maximum) tumor nodules per animal, while in mice injected with A549-BAMBI-GFP cells only 2.5 (1 minimum, 25 maximum) nodules per animal were observed (**Figure 2.6C**). Furthermore, the analysis of the tumor areas per animal showed a median tumor area of 8.4×10^7 μm^2 in control A549-GFP-injected mice whereas the median tumor area in lungs of mice injected with A549-BAMBI-GFP cells was 30 times smaller (2.7×10^6 μm^2). Statistical analysis employing the Mann-Whitney test showed for both analysis significant differences (*P*-values of 0.0295 and 0.0286 for number of nodules and tumor area, respectively) between the mice harboring A549 cells that express the GFP control or BAMBI-GFP (**Figure 2.6C**). This demonstrates that BAMBI reconstitution in A549 cells not only impairs TGFβ-induced cancer cell invasion *in vitro* but also *in vivo*. Additionally, immunohistochemical analysis of the human lung tumors within the mouse lungs showed reduced levels of Smad3 phosphorylation in A549-BAMBI-GFP cells compared to A549-GFP control cells (**Figure 2.6B**) indicating that reconstitution of BAMBI expression also suppressed the activation of TGFβ signaling *in vivo*.

In summary, BAMBI silencing resulted in elevated TGFβ signaling favoring tumor cell invasion, migration and EMT. Furthermore, an elevated activation of TGFβ signaling pathway in the absence of the negative regulator BAMBI may enhance the immunosuppressive effects (125) of TGFβ in tumor microenvironment and promote cancer cell invasion. Therefore, deregulated TGFβ signaling might play a central role in lung cancer progression.

2.2 Mechanisms behind TGFβ-mediated pro-tumorigenic effects in squamous cell lung cancer

Although the prevalence of squamous cell carcinoma of the lung (LUSC) in developed countries is declining, it still accounts for about 25% of NSCLC cases. Despite the great progress in developing targeted approaches in adenocarcinoma of the lung, therapeutic options for LUSC remain very limited as driver oncogene mutations are uncommon (195). For decades platinum-based chemotherapy has been the gold standard for first-line therapy for LUSC patients. However, in a significant proportion of patients cancer cells are resistant to chemotherapy and the disease rapidly progresses. Thus, there is an urgent clinical need to gain insights into mechanisms contributing to LUSC in order to establish mechanism-based biomarkers that help clinicians to identify patients at highest risk for disease progression and therapy resistance.

The TGFβ signaling pathway is implicated in numerous pro-tumorigenic processes, including immune evasion, inflammation and cancer metastasis (196). In the context of LUSC, elevated TGFβ1 levels were correlated with poor patient prognosis (197) with overactivation of the TGFβ pathway as a common feature in lung cancer (189). Moreover, the epithelial-to-mesenchymal transition (EMT) phenotype that is frequently mediated by TGFβ was widely observed in surgically resected specimens and associated with a worse clinical outcome and chemoresistance (133). However, a mechanistic understanding of TGFβ-induced changes and of LUSC progression remains to be established. Therefore, the aim of this project was to combine phenotypic and transcriptome-wide approaches to determine TGFβ-induced dynamic changes in the transcriptome of a LUSC cell line, and thereby derive a candidate prognostic biomarker and validate it in a clinical cohort.

2.2.1 TGFβ treatment enhances pro-tumorigenic properties of LUSC cells

To study the impact of TGFβ on LUSC cells, the LUSC cell line SK-MES1 was used as a cellular model system. Analysis by quantitative immunoblotting showed that TGFβ-induced phosphorylation of Smad2 and Smad3 in SK-MES1 cells reached a maximum after 30 min and rapidly declined thereafter (**Figure 2.7A**). SK-MES1 cells usually grow in tight epithelial colonies, but after treatment with TGFβ they lost cell-cell contacts and acquired an elongated spindle-shaped morphology (**Figure 2.7B**), a feature commonly observed upon TGFβ-induced EMT. In line with these morphological alterations, TGFβ treatment of SK MES1 cells induced the mRNA expression of classical EMT markers such as *SNAI1*, *ZEB1*, *VIM* and *MMP9* (**Figure 2.7C**).

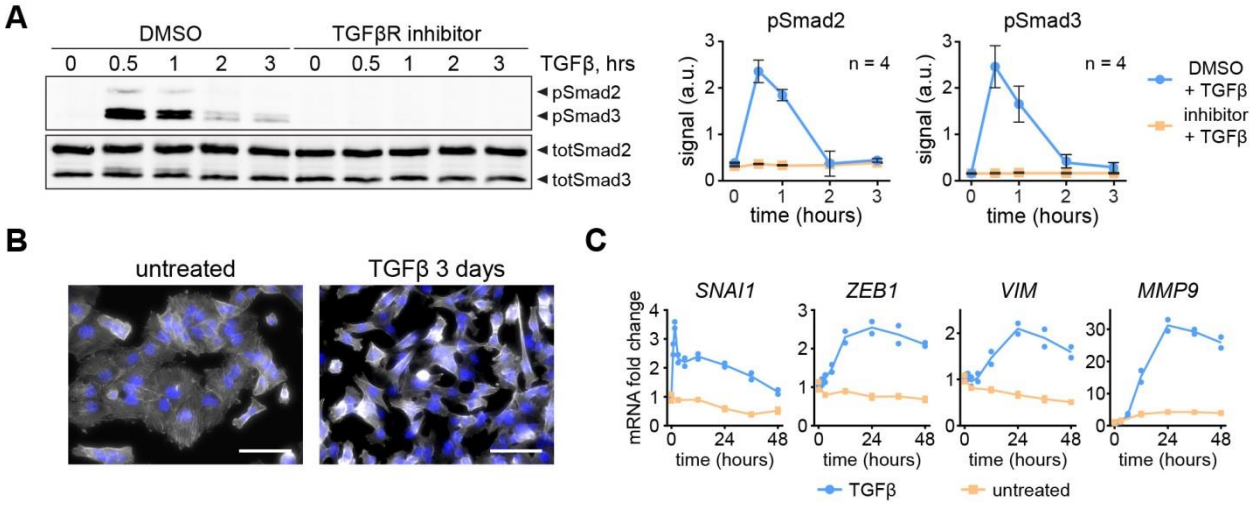

Figure 2.7. TGFβ treatment triggers EMT in SK-MES1 cells. (**A**) TGFβ induces Smad2/3 phosphorylation in TGFβR1-dependent way. SK-MES1 cells were pretreated with TGFβR1 inhibitor SB-431542 or DMSO and then stimulated with 2 ng/ml TGFβ1. Data presented correspond to mean and SD, n is the number of independent experiments. (**B**) Prolonged exposure of SK-MES1 cells to TGFβ1 induces acquisition of EMT-like morphology. Cells were either stimulated with 2 ng/ml TGFβ1 or left untreated for 3 days, fixed and stained for F-actin (white) and DNA (blue). Scale bar corresponds to 50 µm. (**C**) EMT marker genes are upregulated upon TGFβ1 treatment. Growth factor-depleted SK-MES1 cells were stimulated with 2 ng/ml TGFβ1 or left untreated. RNA was extracted and analyzed using qRT-PCR. mRNA expression was normalized to four housekeepers: *GUSB*, *HPRT*, *GAPDH* and *G6PD*. Each dot represents a biological replicate.

Next, to quantitatively examine the impact of TGFβ treatment on the migratory and invasive potential of SK-MES1 cells, workflows to quantitatively assess the impact of TGFβ on migratory and invasive properties of SK-MES1 at the single cell level were established (**Figures 2.8A and 2.8C**). This included the development of a mathematical algorithm to correct for the concave surface of the collagen gels to improve the reliability of quantifications in the 3D collagen invasion assay.

In the 2D migration assay analysis of more than 1000 of single cell tracks per condition showed that the TGFβ treatment resulted in a two-fold increase in migration speed (from 4 to 8 µm/h) (**Figure 2.8B**). Co-treatment with a type I TGFβ receptor inhibitor prevented this effect. In the 3D collagen invasion assay TGFβ treatment resulted in a two-fold increase in collagen-invaded SK-MES1 cells. Some of the TGFβ-treated SK-MES cells invaded more than 100 µm into the dense collagen gels, while untreated cells invaded on average not more than 20 µm (**Figure 2.8D**). The increase in the invasion capacity was TGFβ-specific because it was abolished by co-treatment with a type I TGFβ receptor inhibitor.

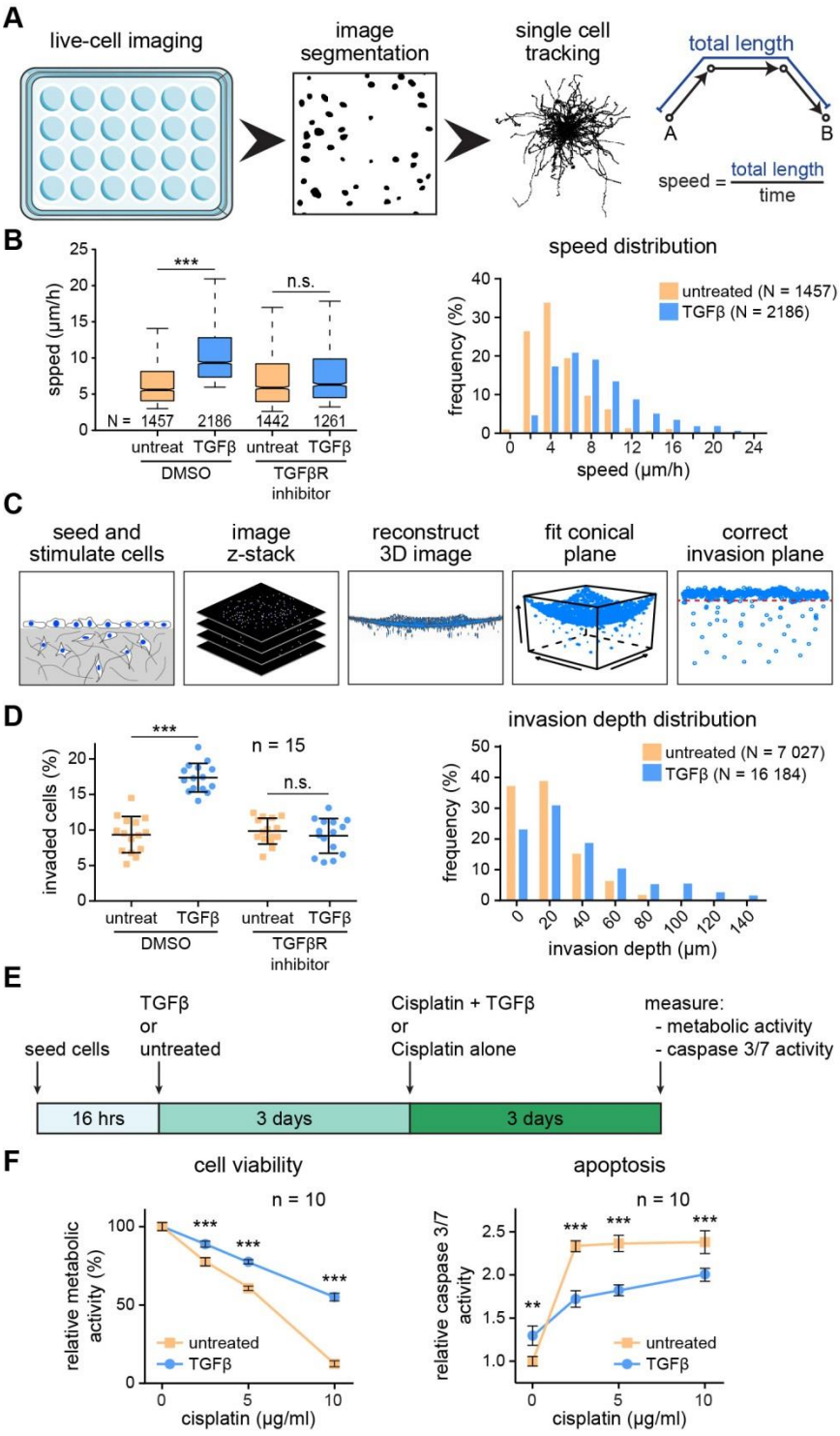

Figure 2.8. TGFβ treatment increases invasiveness and cisplatin resistance of squamous lung carcinoma cells SK-MES1. (**A**) A scheme of the 2D migration assay. (**B**) Migratory properties of SK-MES1 cells are increased upon TGFβ treatment. Cells were seeded in 24-well plate, pretreated with either SB-431542 or DMSO, stimulated with 2 ng/ml TGFβ1 and imaged for 60 hours. Migration speed from each single cell track was quantified. Center lines show the medians; box limits indicate the 25th and 75th percentiles; whiskers extend to 5th and 95th percentiles, N indicates the number of quantified single cell tracks per condition. Statistical analysis was performed using one-way ANOVA; ***, $P < 0.001$; n.s., not significant. (**C**) A scheme of the collagen 3D invasion assay. (**D**) TGFβ stimulation increases number of invading cells and the average invasion depth. SK-MES1 cells were seeded in 96-well plates with precast collagen gels, allowed to attach overnight, growth factor-depleted for three hours, pretreated with either SB 431542 or DMSO, stimulated with 2 ng/ml TGFβ1, allowed to invade for four days, stained with Hoechst and imaged with a confocal microscope. The number of invaded cells and invasion depth were assessed. Data are presented as median and SD, every dot corresponds to a biological replicate (n = 15). N indicates the number of invaded cells. Statistical analysis was performed using one-way ANOVA; ***, $P < 0.001$; n.s., not significant. (**E**) A scheme of the experimental setup. (**F**) Pre-treatment with TGFβ1 reduces sensitivity of SK-MES1 cells to cisplatin treatment. Cells were seeded in 96-well plate, stimulated with either 2 ng/ml TGFβ1 or left untreated for 3 days and then exposed to increasing doses of cisplatin for 3 days. Cell viability and caspase 3/7 activity were assessed. Data presented correspond to mean and SD, n is the number of biological replicates. Statistical analysis was performed using one-way ANOVA; **, $P < 0.01$; ***, $P < 0.001$. Migration experiments were performed by Irina Titkova (DKFZ, Heidelberg), 3D collagen invasion experiments by Magdalena Szczygieł (DKFZ, Heidelberg).

It was reported that the EMT phenotype correlates with increased resistance to chemotherapy (198). To examine the impact of TGFβ on the resistance of SK-MES1 cells to cisplatin, a cell viability assay based on metabolic activity and an apoptosis assay based on caspase 3/7 activity was employed (**Figure 2.8E**). Indeed, three-day pre-treatment of SK-MES1 cells with TGFβ resulted in a 4.4-fold increase of viable cells after 3 days exposure to 10 µg/ml cisplatin (**Figure 2.8F left**). Likewise, pretreatment with TGFβ reduced the caspase 3/7 activity across all tested doses of cisplatin by 25% (**Figure 2.8F right**). Collectively, these data indicate that SK-MES1 cells acquire a more aggressive phenotype upon exposure to TGFβ.

2.2.2 Multiple actin cytoskeleton- and motility-related genes are upregulated in LUSC cells upon TGFβ stimulation

To elucidate mechanisms underlying the TGFβ-induced pro-tumorigenic effects in LUSC, a time-resolved whole-transcriptome RNA-Seq analysis was performed with SK-MES1 cells that were treated with TGFβ for up to 48 hours or were left untreated. Genes were considered as differentially regulated if their overall mRNA expression dynamics in treated versus untreated cells was significantly different (multiple testing-adjusted *P*-value of <0.01). The resulting list of differentially regulated genes was used for Gene Set Enrichment Analysis (GSEA) to identify regulated gene ontology (GO) terms of cellular components, which were subsequently visualized with the REVIGO tool (199) to establish clusters with distinct gene expression patterns. This approach revealed a preferential regulation of four gene clusters encoding actin cytoskeleton-, motility-, ECM- and secretory-related proteins (**Figure 2.9A**). To narrow down the list of potential candidates involved in mediating the TGFβ-induced invasive properties of LUSC cells, the five genes per cluster with the lowest multiple testing-adjusted *P*-values and with at least two-fold peak amplitude change after normalization to corresponding untreated samples were selected. This resulted in a list of 15 genes because some of the genes were among the top five candidates in more than one cluster (**Figures 2.9B and 2.10A**). Interestingly, genes identified as candidates in our approach included *MYO10*, *SERPINE1*, *ITGB3*, *ITGA5*, *TGFBI*, *VIM* and *MARCKS*. These genes were previously associated with increased cancer invasiveness, chemoresistance and worse clinical outcome in different cancer entities including breast, NSCLC, invasive melanoma and prostate cancers (200-205). To determine which of these genes are relevant in the context of LUSC, the alterations of mRNA levels of the selected 15 candidate genes were evaluated in a cohort of 501 LUSC patients from the Cancer Genome Atlas (TCGA) (**Figure 2.9C**). Strikingly, the *MYO10* gene was upregulated in 27% of the patients, whereas an upregulation of the mRNAs of the other genes was only observed in 2–5% of the LUSC patients.

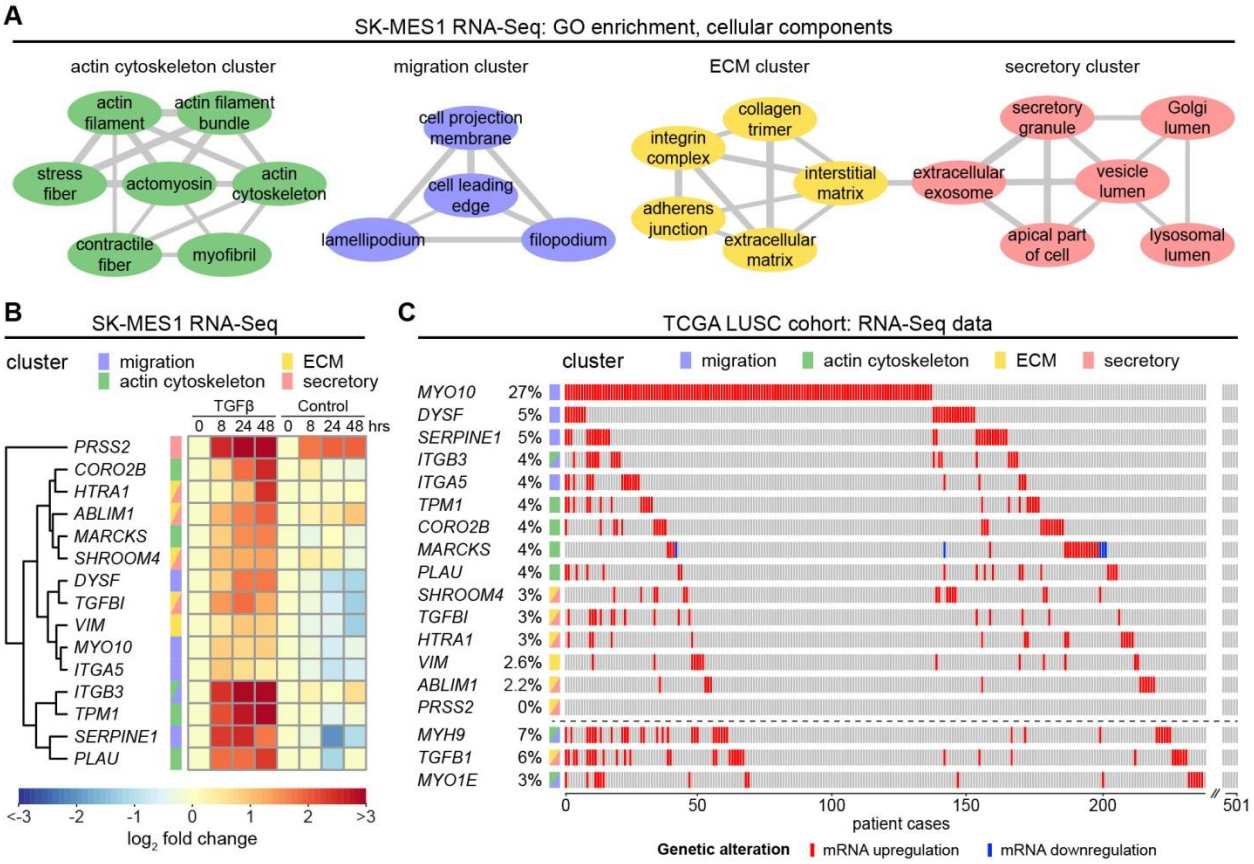

Figure 2.9. TGFβ treatment of LUSC cells results in upregulation of migration- and actin cytoskeleton-related genes. (**A**) Clusters of significantly upregulated GO cellular component gene sets between TGFβ-treated and untreated conditions. SK-MES1 cells were stimulated with 2 ng/ml TGFβ or left untreated. RNA was extracted and sequenced using HiSeq 4000. Significantly upregulated GO terms (adjusted *P*-value <0.01) were visualized using REVIGO (allowed similarity 0.5). Thickness of connecting grey lines corresponds to the similarity of the GO terms. Only clusters that consist of at least two GO terms are displayed. (**B**) Time-resolved dynamics of top differentially regulated candidate genes from each of the clusters. Top five genes from each of the four clusters with the lowest adjusted *P*-values and $\log_2$ fold change of at least 1 after normalization to untreated samples were selected as candidates. In case the same gene belonged to different clusters and satisfied the inclusion criteria, it was marked as belonging to both clusters. (**C**) TCGA LUSC cohort RNA-Seq expression data of selected candidate genes sorted by percentage of mRNA alterations. *MYH9*, *TGFB1* and *MYO1E* genes were additionally included, although they were not among top five genes in any of the clusters. RNA-Seq data processing and gene set enrichment analysis were performed by Sebastian Ohse (AG Busch/Börries, Freiburg University).

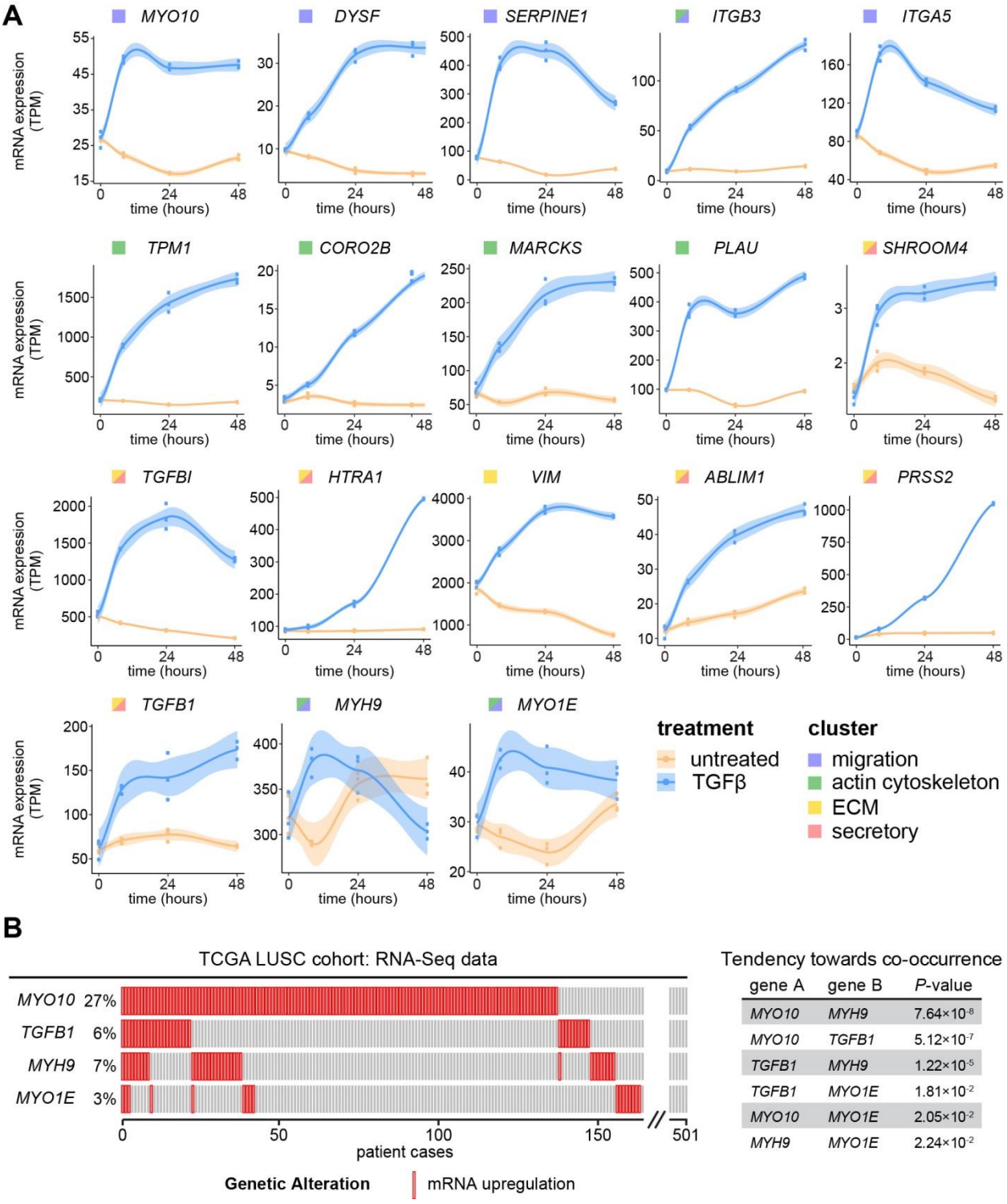

Figure 2.10. Time-resolved dynamics of candidate genes. (**A**) Cells were growth factor-depleted for three hours and stimulated with 2 ng/ml TGFβ1 or left untreated. mRNA was extracted and sequenced using HiSeq 4000. Data presented in TPM (transcripts per million) values. Each dot represents a biological replicate, shaded areas correspond to standard error. (**B**) TCGA RNA-Seq expression data of candidate myosin and *TGFB1* genes in LUSC. The significance of the association was tested using Fisher's exact test.

Interestingly, the genes with the highest percentage of mRNA upregulation in LUSC patients belonged either to the migration or the actin cytoskeleton clusters, while genes from the ECM and secretory clusters were rarely altered in LUSC patients, although several of the genes from these clusters showed a high fold increase in SK-MES1 cells upon TGFβ treatment (**Figures 2.9B and 10A**). Given the prominent upregulation of *MYO10* expression in LUSC patients and the pivotal role of non-muscle myosins in mediating cancer cell invasion in multiple cancer entities (205), we examined whether other myosin-encoding genes scored high in our analysis but were not among the top five regulated genes. Indeed, second and third most regulated genes encoding myosins were *MYH9* and *MYO1E*, which were previously implicated in cancer progression (206, 207). Both of these myosin genes were upregulated in LUSC patients of the TCGA cohort with *MYH9* being overexpressed in 7% of the cases (**Figure 2.9C lower panel**). Furthermore, a significant co-occurrence of an upregulation of the mRNAs of *MYO10*, *MYH9*, *MYO1E* and *TGFB1* was observed in LUSC patients of the TCGA cohort (**Figure 2.10B**), suggesting that the exposure of tumor cells to elevated levels of TGFβ might have stimulated upregulation of motility and invasion-related myosins. Therefore, all three myosin genes were included for further analysis.

2.2.3 TGFβ-induced myosin motors are essential for TGFβ-mediated cancer cell invasion

To examine the biological importance of the candidate myosins, the RNA-Seq data were validated with time-resolved examinations by qRT-PCR of TGFβ-stimulated SK-MES1 cells. In line with the dynamics of gene expression observed by RNA-Seq (**Figure 2.11A**), all three candidate genes demonstrated strong mRNA induction upon TGFβ treatment, with *MYO10* expression being the most pronounced and most sustained (**Figure 2.11B**). Given the role of non-muscle myosins in cancer metastasis, the effect of gene silencing on the ability of the SK-MES1 cells to invade 3D collagen gels in response to TGFβ stimulation was examined. A pool of four targeting siRNAs was used to knockdown either of the *MYO10*, *MYH9*, *MYO1E* genes with resulting in knockdown efficiency of more than 85% at the mRNA level (**Figure 2.11C**). Whereas TGFβ treatment of SK-MES1 cells transfected with control non-targeting siRNA resulted in a two-fold increase in the number of invaded cells (**Figure 2.11D**), the TGFβ-enhanced invasion of SK-MES1 cells was abrogated upon downregulation of the different myosins. These results indicate that the TGFβ-induced non-muscle myosins MYO10, MYH9 and MYO1E play a non-redundant and crucial role in mediating invasiveness of the LUSC cells.

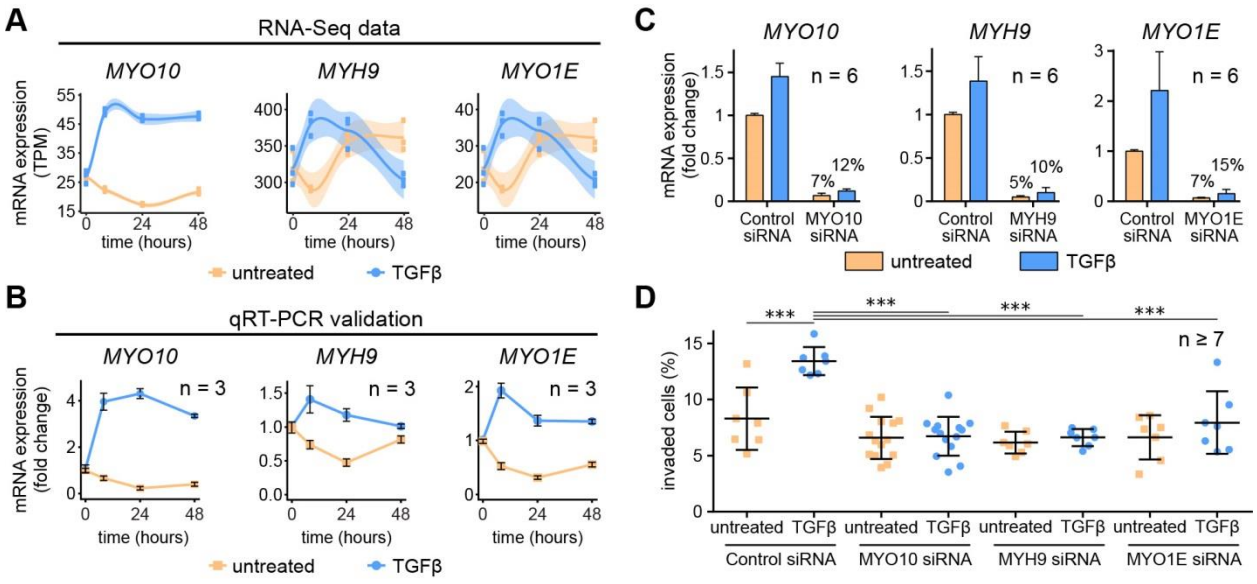

Figure 2.11. Knockdown of TGFβ-inducible myosins abrogates TGFβ-mediated cancer cell invasion. (**A**) Time-resolved mRNA expression dynamics of selected non-muscle myosins upon TGFβ treatment in SK-MES1 cells. Cells were growth factor-depleted for three hours and stimulated with 2 ng/ml TGFβ1 or left untreated. mRNA was extracted and sequenced using HiSeq 4000. Data presented in TPM (transcripts per million) values. Each dot represents a biological replicate; shaded areas correspond to standard error. (**B**) RNA of TGFβ-treated and untreated SK-MES1 cells that was used for RNA-Seq was also analyzed with qRT-PCR. Data presented correspond to mean and SD from three biological replicates. (**C**) After 36 hours of siRNA transfection SK-MES1 cells were stimulated for 1 hour with TGFβ or left untreated. mRNA was extracted and the knockdown efficiency was analyzed using qRT-PCR. Data represent mean and SD from six biological replicates. (**D**) SK-MES1 cells were transfected with siRNAs for 36 hours and stimulated with 2 ng/ml TGFβ for four days. Amount of invaded cells into the collagen gel was assessed. One representative experiment is shown. Every dot corresponds to a biological replicate (n ≥ 7), black line indicates the median. Statistical analysis was performed using one-way ANOVA; ***, $P < 0.001$. 3D collagen invasion assays were performed by Magdalena Szczygieł (DKFZ, Heidelberg).

2.2.4 *MYO10* mRNA overexpression is prognostic for overall survival of patients with squamous cell carcinoma

Actin-based protrusions and TGFβ-induced myosins are crucial for multiple phases of the metastatic cascade (208). Therefore, the clinical relevance of *MYO10*, the non-muscle myosin gene that showed the strongest upregulation in response to TGFβ stimulation in SK-MES1 cells and the highest mRNA overexpression in LUSC patients of the TCGA cohort, was assessed in paired tumor and tumor-free tissues from a NSCLC cohort including both LUAD and LUSC patients (**Table S6.2**). For each tumor entity, patients were divided into two subgroups based on the expression ratio of *MYO10* mRNA in tumor versus tumor-free tissue, *MYO10* fold change <1 and *MYO10* fold change >1, respectively (**Figure 6.12A**). To investigate the prognostic value of the *MYO10* mRNA expression ratio, Cox regression analysis was

performed (**Table 2.1**). Univariate analysis indicated that a high *MYO10* mRNA expression ratio (*P* = 0.018), gender (*P* = 0.04) as well as the pathological stages (*P* = 0.005 for pstage II and *P* <0.001 for pstage III) were prognostic factors for the overall patient survival. Further multivariate analysis suggested that a high *MYO10* mRNA expression ratio was only prognostic for LUSC patients, but not for LUAD patients (**Table 2.2**).

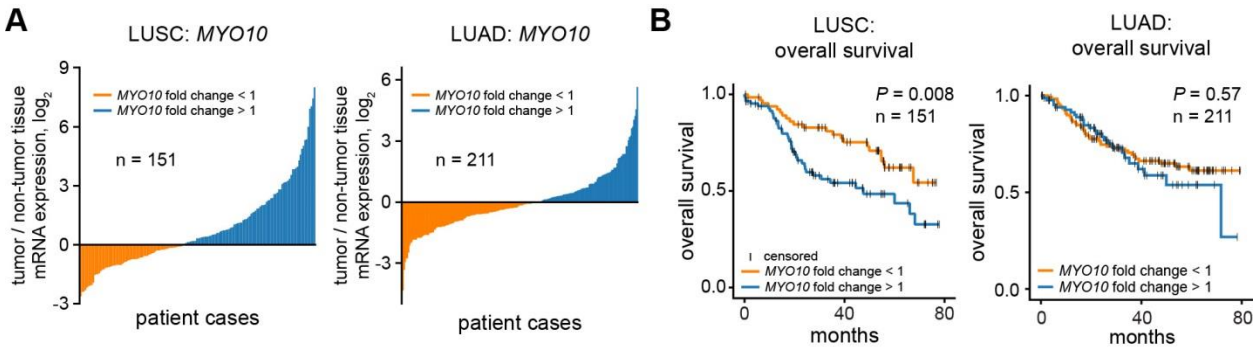

Figure 2.12. *MYO10* mRNA expression ratio is prognostic for overall survival of LUSC but not LUAD patients. (**A**) Left, *MYO10* mRNA expression ratio in tumor and adjacent non-tumor tissues. RNA from tumor and tumor-free fresh-frozen resected tissues was isolated and *MYO10* expression was measured. (**B**) Kaplan-Meier curves for overall survival using *MYO10* mRNA expression ratio. Significance of difference between the two groups was tested using non-parametric Mann-Whitney U test. mRNA expression was measured by Marc Schneider (ThoraxKlinik, University Heidelberg), survival analysis performed by Thomas Muley (ThoraxKlinik, University Heidelberg).

	All patients, n = 362	
variable	**HR (95% CI)**	***P*-value**
MYO10 in tumor (high vs. low expression)	1.042 (0.733–1.482)	0.818
MYO10 in non-tumor (high vs. low expression)	0.780 (0.548–1.109)	0.166
MYO10 ratio (up vs. down-regulation)	1.533 (1.075–2.186)	**0.018**
Gender (m vs. f)	1.555 (1.021–2.369)	**0.04**
Age	1.018 (0.999–1.037)	0.068
Histology (LUAD vs. LUSC)	0.839 (0.590–1.192)	0.327
pStage (II vs. I)	2.059 (1.238–3.425)	**0.005**
pStage (III vs. I)	3.899 (2.409–6.311)	**<0.001**
Smoking status (smoker vs non-smoker)	1.606 (0.811–3.180)	0.081
Smoking status (ex-smoker vs non-smoker)	1.232 (0.633–2.397)	0.539

Table 2.1. *MYO10* mRNA expression ratio predicts outcome in lung cancer patient cohort.

Using the *MYO10* mRNA expression ratio between tumor and adjacent tumor-free tissues to separate the patient groups, *MYO10* mRNA expression ratio was indeed found to be prognostic for overall survival of LUSC patients (*P* = 0.008, **Figure 2.12B left**), but not for LUAD patients (*P* = 0.57, **Figure 2.12B right**).

Multivariate analysis of overall survival

	LUAD patients, n = 211		**LUSC** patients, n = 151	
variable	**HR (95% CI)**	***P*-value**	**HR (95% CI)**	***P*-value**
MYO10 ratio (up vs. down-regulation)	1.008 (0.967–1.050)	0.71	1.012 (1.006–1-018)	**<0.001**
Gender (m vs. f)	1.405 (0.832–2.373)	0.204	1.750 (0.75–4.083)	0.195
Age	1.005 (0.979–1.033)	0.695	1.032 (0.999–1.066)	0.06
pStage (II vs. I)	2.372 (1.120–5.025)	**0.024**	2.135 (1.010–4.513)	**0.047**
pStage (III vs. I)	4.966 (2.382–10.353)	**<0.001**	4.613 (2.169–9.811)	**<0.001**

Table 2.2. Differential expression of *MYO10* is an independent predictor of survival in squamous cell carcinoma patients.

Next, the link between *MYO10* mRNA expression ratio and the outcome of the adjuvant chemotherapy treatment of LUSC patients was assessed. The LUSC patients were subdivided based on their *MYO10* mRNA expression ratio and the overall survival of cisplatin-treated and cisplatin-untreated patients within each group was compared (**Figure 2.13A**). Patients with lower *MYO10* mRNA expression in the resected tumors than in the adjacent tumor free-tissue benefited from cisplatin treatment compared to untreated patients (*P* = 0.028), while patients with high *MYO10* mRNA expression ratio did not perform better than untreated patients (*P* = 0.343). Therefore, the *MYO10* mRNA expression ratio is predictive for the outcome of adjuvant chemotherapy treatment of LUSC patients.

Because of the observed enhanced chemoresistance of LUSC cells after TGFβ treatment (**Figure 2.8B**) and because TGFβ-induced EMT has been previously associated with chemotherapy resistance in patients (133, 209) the expression of EMT markers in LUSC patient tissues was examined. Notably, patients with an elevated *MYO10* mRNA expression ratio displayed a higher expression of EMT signature genes such as *SNAI2* and *TWIST1* (**Figure 2.13B**).

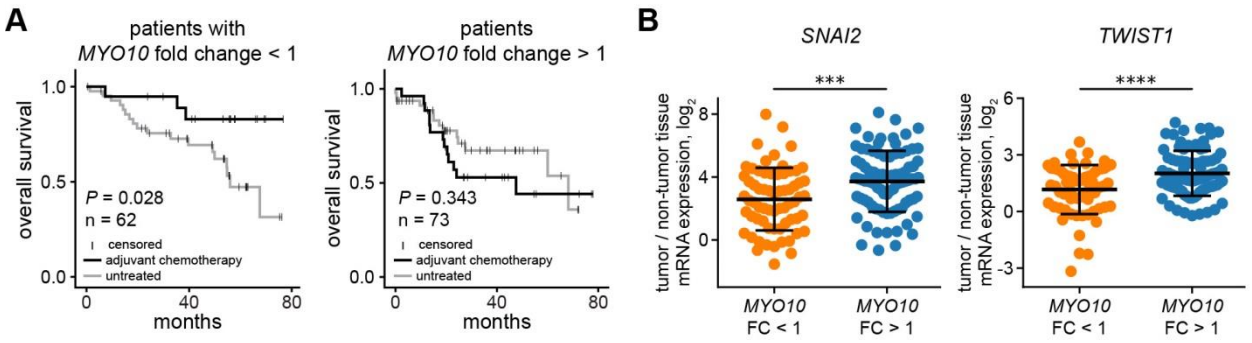

Figure 2.13. *MYO10* mRNA expression ratio is predictive for chemotherapy response of LUSC patients. (**A**) Kaplan-Meier curves for adjuvant chemotherapy response in *MYO10* low (left) and *MYO10* high (right) patients. Significance of difference between the two groups was tested using non-parametric Mann-Whitney U test. (**B**) Differences of *SNAI2* and *TWIST1* expression depending on *MYO10* mRNA expression ratio were tested by unpaired *t*-tests; ***, $P < 0.001$; ****, $P < 0.0001$. mRNA expression was measured by Marc Schneider (ThoraxKlinik, University Heidelberg), survival analysis performed by Thomas Muley (ThoraxKlinik, University Heidelberg).

The fact that TGFβ is one of the most potent EMT-inducers (110) and the co-occurrence of *MYO10* and *TGFB1* mRNA upregulation in a substantial proportion of LUSC patients (**Figure 2.10B**) suggest that activation of TGFβ signaling might trigger the observed alterations in LUSC patients. Finally, a higher *MYO10* mRNA expression ratio was observed in patients with stage III disease (**Figure 2.14A**), making it prognostic for patients with a higher pathological stage and affected local or distant lymph nodes (**Figures 2.14B and 2.14C**). Taken together, our studies suggest that the mRNA expression ratio of *MYO10* can be used as a new independent prognostic biomarker for survival in patients with resected LUSC.

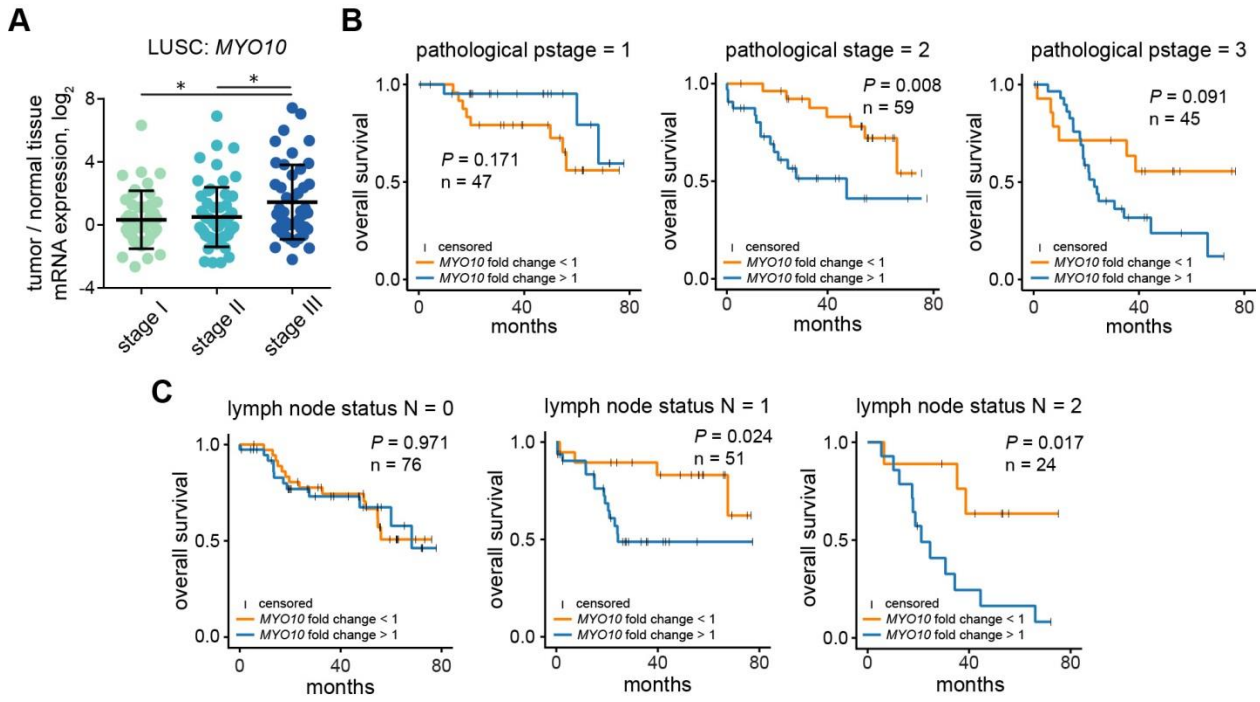

Figure 2.14. High *MYO10* mRNA expression ratio correlates with tumor stage and lymph node metastasis status. (**A**) *MYO10* expression ratio in different stages of LUSC. Differences were tested by one-way ANOVA; *, $P \leq 0.05$. (**B**) Kaplan-Meier curve for the pathological stages of LUSC patients. Significance of difference between the two groups was tested using non-parametric Mann-Whitney U test. (**C**) Kaplan-Meier curves for lymph node status using *MYO10* mRNA expression ratio. Significance of difference between the two groups was tested using non-parametric Mann-Whitney U test. mRNA expression was measured by Marc Schneider (ThoraxKlinik, University Heidelberg), survival analysis performed by Thomas Muley (ThoraxKlinik, University Heidelberg).

2.3 An ODE-based model of the TGFβ/Smad pathway signal transduction in LUAD cell lines

Having previously established that TGFβ signal transduction pathway is deregulated in lung cancer (**section 2.1**), it is important to understand how the dynamic properties of the pathway are controlled in this particular context. Therefore, the dynamic behavior of TGFβ-induced pathway activation was comprehensively examined in lung adenocarcinoma (LUAD) cell lines.

The lung adenocarcinoma cell lines H1975, H838 and H1650 were selected as representatives of a subset of alterations that are commonly observed in lung cancer patients (**Table 1.1**). Of the three examined adenocarcinoma cell lines, H838 had a wild-type EGFR. H1975 had a known L858R EGFR activating mutation alongside with a "gatekeeper" T790M mutation that confers resistance against first generation of anti-EGFR small-molecular inhibitors such as erlotinib by limiting the access of the inhibitor to the binding pocket of the kinase domain. The H1650 cell line had a 15-nucleotide activating deletion in the kinase domain of the EGFR. Additionally, H838 cells overexpressed KRAS, while H1650 cells had an inactivating mutation in PTEN. Furthermore, the cell lines differed with respect to their EMT state. H1650 cells demonstrated the most epithelial-like morphology and gene expression signature, while H838 cells had a fully mesenchymal gene expression signature. H1975 cells demonstrated features of both epithelial and mesechymal cells that is also referred to as a hybrid phenotype (194).

2.3.1 Dose- and time-dependent dynamics of TGFβ signal transduction

In response to TGFβ stimulation the TGFβ receptor becomes activated and phosphorylates Smad2 and Smad3 proteins on their C-terminus. Therefore TGFβ-induced Smad2/3 phosphorylation was used as an indicator for pathway activation. To understand the dynamic behavior of the pathway, it is important to optimize the initial stimulation dose. In general, a dose considered to be optimal when the cellular response scales linearly with the applied dose of a stimulus. A too low dose would not cause significant TGFβ-induced Smad phosphorylation due to the constantly active cytoplasmic phosphatases and negative regulators, whereas a too high dose would cause receptor saturation.

To assess the ability of the three selected LUAD cell lines to respond to TGFβ stimulation with Smad2/3 phosphorylation and to determine an optimal dose for time-resolved analysis, cells were stimulated with increasing doses ranging from 0 to 10 ng/ml TGFβ. Activation of the TGFβ pathway was determined

by measuring the phosphorylation of Smad2 and Smad3 proteins 90 min after addition of the TGFβ ligand using quantitative immunoblotting.

In all three cell lines the amount of phosphorylated Smad2 and Smad3 almost linearly scaled with the increasing TGFβ concentrations until saturation was reached (**Figure 2.15A**). Interestingly, the saturation was achieved with a dose of 1 ng/ml TGFβ in H1975 and H838 cells, while a lower dose of 0.5 ng/ml TGFβ was sufficient to induce the maximal pathway activation in H1650 cells. Because sufficiently strong TGFβ-induced Smad2/3 phosphorylation is required to reliably determine the dynamic behavior of the pathway and the use of the identical TGFβ dose for all three cell lines is preferred to allow the direct comparison of the resulting Smad2/3 phosphorylation dynamics, the dose of 1 ng/ml TGFβ was chosen as a compromise for subsequent time-resolved experiments.

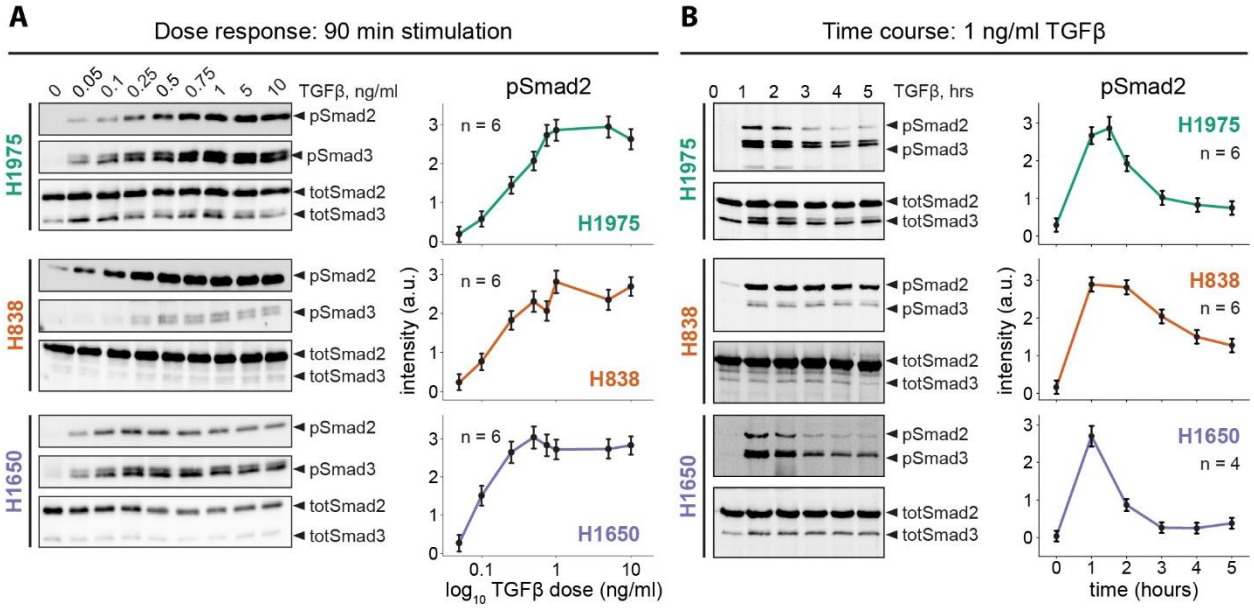

Figure 2.15. Dose- and time-resolved analysis of TGFβ/Smad signaling pathway in LUAD cell lines. H838, H1975 and H1650 cells were growth factor-depleted for three hours and subsequently treated with respective doses of TGFβ lysed after 90 min of stimulation for a dose-response analysis (**A**) or stimulated with 1 ng/ml TGFβ and lysed at the indicated time points for time course experiments (**B**). Subsequently, cellular lysates were subjected to immunoprecipitation with antibodies against Smad2/3 and analyzed using quantitative immunoblotting. Proteins were visualized with chemiluminescence and detected using ImageQuant LAS 4000 imager. Total (tot) and phosphorylated (p) levels of Smad2 and Smad3 were assessed. Left panels show representative immunoblots. Right panels display scaled pSmad2 intensities from several independent experiments using BlotIt script (210). For simplicity only pSmad2 quantifications are shown, because dynamics of Smad2 and Smad3 phosphorylation were similar. Error bars correspond to standard error estimated by the BlotIt package for R developed by Dr. Daniel Kaschek; n indicates number of independent experiments.

To determine the dynamic behavior of TGFβ-induced Smad2/3 phosphorylation in the LUAD cell lines H1975, H838 and H1650, the cells were growth factor depleted for three hours, were stimulated with 1 ng/ml TGFβ over a period of five hours and were lysed at the indicated time points. Subsequently, the dynamics of Smad2 and Smad3 phosphorylation, and the amount of Smad4 bound to activated Smad2/3 complexes was assessed by quantitative immunoblotting.

Time course analysis of the TGFβ-induced Smad2/3 phosphorylation in H1975, H838 and H1650 cells showed that in response to TGFβ treatment, pSmad2 and pSmad3 signals increased, reaching a peak at around 60 min after TGFβ stimulation in all three cell lines (**Figure 2.15B**). Interestingly, the cell lines demonstrated different rates of signal decline after reaching the activation peak of Smad2/3 phosphorylation. In H1975 and H838 cells, Smad2/3 phosphorylation remained elevated for 30–60 min after reaching the peak followed by a decline afterwards. The TGFβ-induced Smad2/3 phosphorylation declined in H838 cells slower than in H1975 cells, and remained elevated in both cell lines above the baseline up to five hours. In contrast, in H1650 cells Smad2 phosphorylation after reaching its peak at 60 min quickly declined almost to the basal unstimulated state five hours after TGFβ stimulation. In each cell line the amount of Smad4 recruited to the activated Smad2/3 complexes closely followed the dynamics of Smad2/3 phosphorylation in each cell line (**Figure S6.2**). Such pronounced differences in the Smad phosphorylation dynamics in response to TGFβ stimulation suggested that different mechanisms control the dynamics of TGFβ signal transduction in the examined LUAD cell lines.

2.3.2 Dose-dependent Smad2/3 phosphorylation dynamics

To further examine how dynamic features of the TGFβ/Smad signaling pathway, such as the maximal amplitude of Smad2/3 phosphorylation, the peak time and the level of the steady state, change with respect to the TGFβ dose (**Figure 2.16A**), a densely-sampled time course stimulation of H1975 cells with increasing doses of TGFβ was performed. H1975 cells were growth factor depleted for three hours and were stimulated with the concentrations ranging from 0.05 to 0.85 ng/ml TGFβ. Cells were lysed at the indicated time points, Smad2/3 immunoprecipitation was performed and Smad2/3 phosphorylation dynamics was examined with quantitative immunoblotting.

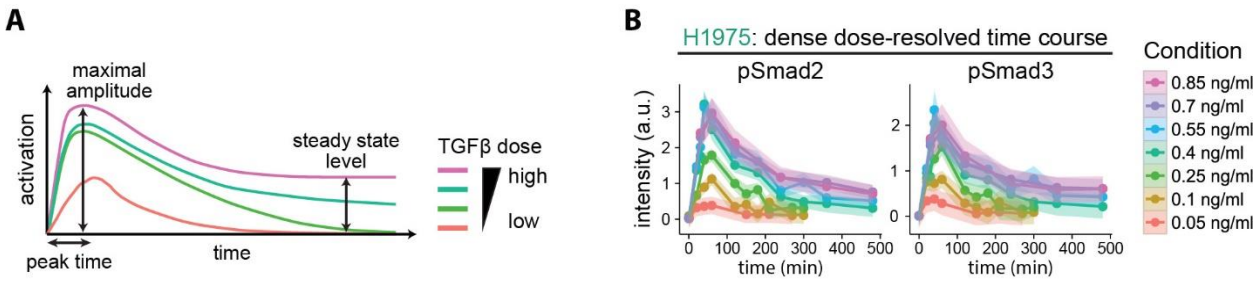

Figure 2.16. Dose-resolved time course analysis of TGFβ/Smad signaling pathway activation. (**A**) H1975 cells were growth factor-depleted for three hours and treated with given TGFβ concentrations. At the indicated time-points, cells were lysed in whole-cell lysis buffer and Smad2/3 immunoprecipitation was performed. Resulting samples were analyzed with quantitative immunoblotting. Proteins were visualized with chemiluminescence and detected using ImageQuant LAS 4000 imager. Signals from independent experiments were scaled using BlotIt script (210). Dots represent mean, shaded area corresponds to standard error estimated by the BlotIt package for R developed by Dr. Daniel Kaschek. (**B**) Scheme illustrating TGFβ pathway response to the increasing doses of the ligand.

The maximal amplitude of TGFβ-induced Smad2/3 phosphorylation and the steady state level of phosphorylated Smad2/3 gradually scaled with the applied TGFβ dose until pathway saturation was reached at a dose of approximately 0.7 ng/ml TGFβ (**Figure 2.16B**). Furthermore, shorter peak time was observed upon increasing TGFβ doses as the activation peak was reached 60 min after stimulation with a low dose of 0.05 ng/ml TGFβ used, while the dose of 0.85 ng/ml TGFβ resulted in an earlier peak at 45 min. The TGFβ-induced dynamic behavior of Smad2 and Smad3 phosphorylation closely resembled each other.

Overall, the peak amplitude and the steady state level of Smad2/3 phosphorylation positively correlated with the increase of sub-saturating TGFβ doses, while the peak time inversely correlated with the TGFβ dose.

2.3.3 Effects of network perturbation on TGFβ-induced Smad2/3 phosphorylation

Having observed a transient TGFβ-induced Smad2/3 phosphorylation in all examined LUAD cell lines and having established the dynamic features of the pathway that change in response to TGFβ stimulation, it is important to understand which processes control these features. Several potential mechanisms were suggested to control the activation of the TGFβ signaling pathway. A most commonly discussed mechanism involves degradation of the TGFβ receptor mediated by Smad7 and E3 ligases Smurf1/2, all of which are induced in response to TGFβ stimulation (50, 51). Additionally, transcription-independent mechanisms such as receptor and Smad dephosphorylation by phosphatases (64, 211), receptor

degradation by constitutively active mechanisms (185), and ligand depletion (184) were also reported. Therefore, to examine the mechanisms that control attenuation of the TGFβ pathway in the selected LUAD cell lines, several inhibitors such as actinomycin D (ActD), cycloheximide (CHX) and MG-132 that block the molecular processes of transcription, translation and ubiquitin-dependent degradation respectively were used. H1975, H838 and H1650 cells were growth factor depleted for three hours, were pre-treated for 30 min with respective inhibitors and were stimulated with 1 ng/ml TGFβ. Cells were lysed at the indicated time points, Smad2/3 immunoprecipitation was performed and dynamic behavior of TGFβ-induced Smad2/3 phosphorylation upon co-treatment with inhibitors was examined with quantitative immunoblotting.

To confirm that selected concentrations of the inhibitors are sufficiently active in the selected LUAD cell lines, the amount of SnoN protein bound to activated Smad complexes (SnoN CoIP) was additionally assessed. The *SKIL* gene encoding SnoN is directly induced by activated Smad complexes and the *SKIL* mRNA is already transcribed 45–60 min after TGFβ stimulation, followed by protein translation (68). SnoN binds to activated Smad complexes and acts as a transcriptional co-repressor by changing the affinity of the Smad complexes towards target genes (212). SnoN that is bound to activated Smad complexes is targeted for ubiquitin-dependent proteosomal degradation (213, 214). Therefore, inhibition of transcription and translation of SnoN with ActD and CHX respectively, should prevent the accumulation of SnoN bound to activated Smad complexes, while inhibition of the proteasome with MG-132 should result in higher levels of SnoN in complex with Smads in comparison to the DMSO control.

Indeed, no recruitment of SnoN to Smad2/3 complexes was observed upon inhibition of mRNA transcription with 1 µg/ml actinomycin D or inhibition of protein translation with 20 µg/ml cycloheximide (**Figure 2.17A SnoN CoIP panels**). On the contrary, blocking proteosomal degradation with 10 µg/ml MG-132 resulted in increased accumulation of SnoN in complex with Smad2/3 in comparison to DMSO-treated control cells. Therefore, these results confirm that in each case the concentration of the inhibitor was appropriately selected.

Inhibition of mRNA transcription with ActD resulted in a complete switch from transient to sustained TGFβ-induced Smad2/3 phosphorylation in H1975 and H838 cell lines without changing the maximal amplitude of Smad2/3 phosphorylation, suggesting an important role of strong transcriptional negative feedbacks in these two cell lines (**Figure 2.17B**). Whereas, in H1650 cells TGFβ-induced Smad2/3 phosphorylation still declined in the presence of ActD, although at a slower rate than in the control cells

(**Figure 2.17B**). This observation suggested the presence of both transcription-independent and -dependent feedback loops in H1650 cells.

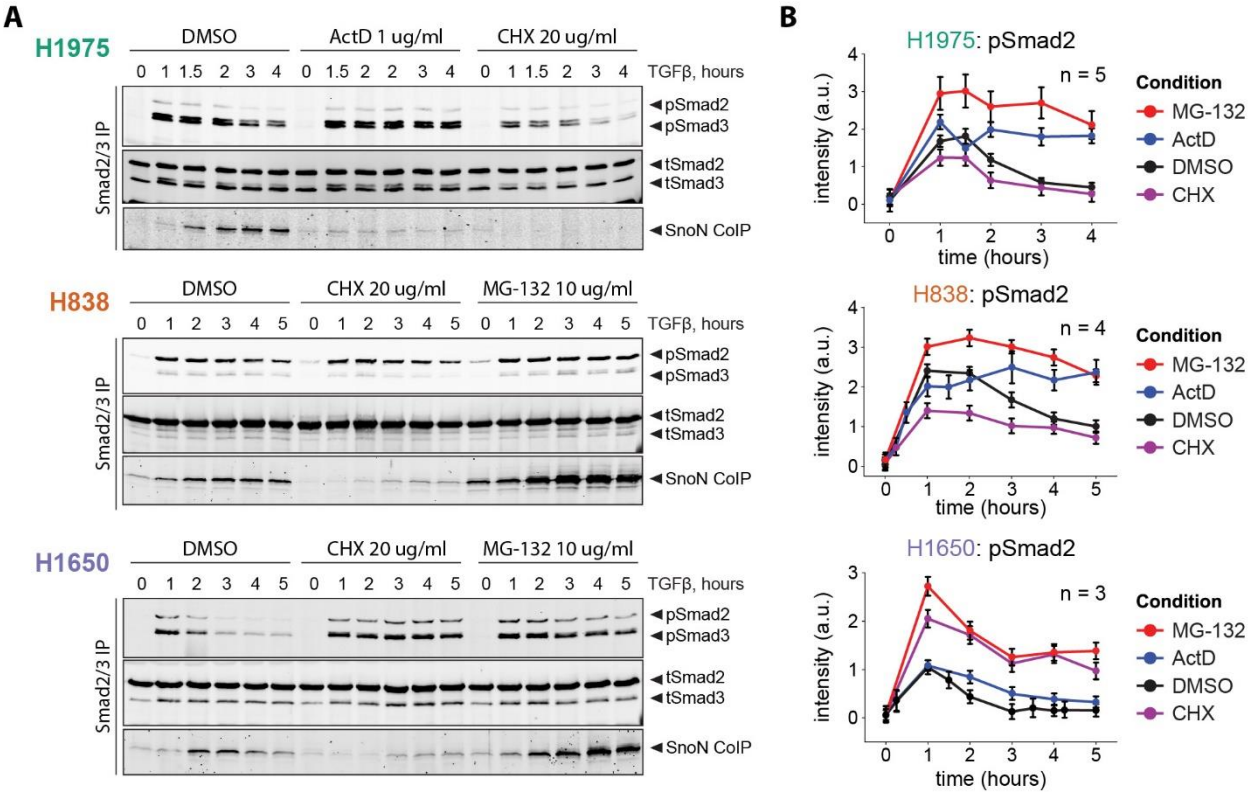

Figure 2.17. Perturbation of the TGFβ/Smad pathway. (**A**) H838, H1975 and H1650 cells were growth factor-depleted for three hours and pre-treated for 30 min with either 1 µg/ml ActD, 20 µg/ml CHX, 10 µg/ml MG-132 or equal volume of DMSO as a control. Cells were stimulated with 1 ng/ml TGFβ, lysed at the indicated time points for time course experiments. Cellular lysates were subjected to immunoprecipitation with antibodies against Smad2/3 and analyzed using quantitative immunoblotting. Proteins were visualized with far-red fluorescence and detected using Odyssey infrared imager. Total (tot) and phosphorylated (p) levels of Smad2 and Smad3, and co-immunoprecipiratied SnoN (SnoN CoIP) were assessed. Representative immunoblots are shown. (**B**) Cells were lysed in RIPA buffer and Smad2/3 immunoprecipitation was performed. Resulting samples were analyzed with quantitative immunoblotting. (**B**) Intensities of phosphorylated Smad2 from several independent experiments were scaled using BlotIt script (210). For simplicity only pSmad2 quantifications are shown, because dynamics of Smad2 and Smad3 phosphorylation were similar. Dots represent mean, error bars correspond to standard error estimated by the BlotIt package for R developed by Dr. Daniel Kaschek. n indicates number of independent experiments.

Surprisingly, inhibition of protein translation with CHX resulted in a weaker and transient Smad2/3 phosphorylation in H1975 and H838 cells. In contrast, upon application of CHX to H1650 cells, the amplitude of Smad2/3 activation was higher than in the control condition and slowly declined over time. Futhermore, in this case, Smad2/3 phosphorylation did not attenuate to the same level as in the control and ActD-treated cells, but rather remained elevated.

Finally, the application of the proteasome inhibitor MG-132 resulted in a higher amplitude of pathway activation in all three tested cell lines. Interestingly, the cell lines demonstrated different degrees Smad2/3 sustained phosphorylation upon MG-132 treatment. In H1975 and H838 cells the increased Smad2/3 phosphorylation remained elevated over the entire experimental time-frame with only a slight decline at the latest time points. In contrast, H1650 cells showed much faster decline of Smad2/3 phosphorylation after the initial peak. Interestingly, the initial decline was followed by the establishment of a new steady state of Smad2/3 phosphorylation at the same level as after CHX treatment.

Surprisingly, none of the inhibitor treatments affected the Smad2 and Smad3 protein levels within the experimental time frame. This suggested that the Smad2 and Smad3 proteins are relatively stable and possess a low turnover rate irrespective of their phosphorylation state. This observation indicated that degradation of the phosphorylated Smad2/3 is not the main mechanism of the observed transient pathway dynamics, in contrast to what was reported in other cellular systems (215, 216).

2.3.4 Mathematical model of TGFβ signal transduction

The experimental analysis of the dose- and time-resolved TGFβ-induced Smad2/3 phosphorylation in three selected LUAD cell lines revealed distinct dynamic features and differential impact of inhibitors. The following features of the pathway could not be intuitively explained: (i)different dynamic behavior of the TGFβ-induced Smad2/3 phosphorylation with the most sustained in H838 cells, intermediate in H1975 cells, and the least sustained in H1650 cells; (ii) switch from transient to sustained TGFβ-induced Smad2/3 phosphorylation dynamics in H1975 and H838 cells in response to inhibition of mRNA transcription, whereas in H1650 only a partial switch to sustained Smad2/3 phosphorylation dynamics was achieved upon inhibition of mRNA translation; (iii) weaker transient dynamics in H1975 and H838 cells in response to inhibition of protein translation with cycloheximide, in contrast a higher amplitude of TGFβ-induced Smad2/3 phosphorylation in H1650 cells; (iv) sustained increased TGFβ-induced Smad2/3 phosphorylation in H1975 and H838 cells when proteasome-mediated protein degradation is inhibited, in contrast to transient pathway overactivation in H1650 cells.

To disentangle these complex observations and to obtain insights into the underlying mechanisms that control the dynamic behavior of the TGFβ signaling pathway, an ordinary differential equation (ODE)-based mathematical model was developed in collaboration with Dr. Raphael Engesser (Freiburg

University). In such model each reaction represents the time-dependent changes in the concentration of certain model components.

2.3.4.1 Establishment of the mathematical core model

The structure of the model was based on the following assumptions (**Figure 2.18**). The TGFβ receptor was modeled as one species not differentiating on type I and type II TGFβ receptors, because experimental data was not acquired at the receptor level. Incorporation of constant ligand-independent receptor turnover into the model structure was essential to describe the discrepancy between the effects of translational (CHX) and transcriptional (ActD) inhibitors on the dynamics of TGFβ-induced Smad2/3 phosphorylation (**Figure 2.17B**). The receptor protein was assumed to be constantly produced from the corresponding mRNA and degraded by the proteasome.

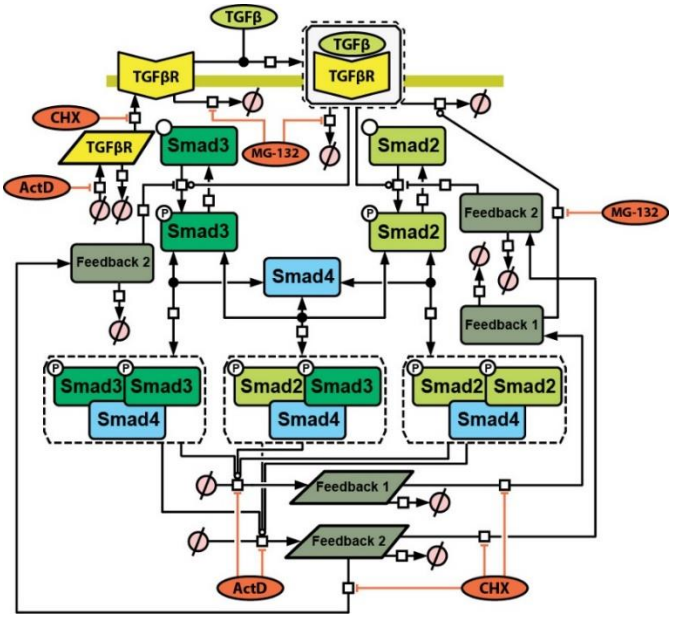

Figure 2.18. The structure of the mathematical model of TGFβ-induced Smad2/3 signal transduction. Catalytic reactions are represented by circle-headed lines, inhibition by bar-headed lines. Red capsules correspond to inhibitors. Prefix "P" indicates phosphorylated state. Activated species are encircled with dashed line. Parallelograms indicate mRNA species. Protein abundance of Smad2, Smad3 and Smad4 was assumed to be constant according to the experimental data (**Figure 2.17**). The full list of the dynamic variables, model reactions, conditions and equations is provided in the **section 6.3**.

The receptor is activated upon TGFβ binding and gains the ability to induce Smad2 and Smad3 phosphorylation. Phosphorylated R-Smads can form trimeric complexes with Smad4 and induce the transcription of downstream feedback loops. The existence of three different Smad trimers was assumed: Smad2–Smad2–Smad4, Smad2–Smad3–Smad4 and Smad3–Smad3–Smad4 based on the existing knowledge (217, 218). All three complexes were modeled with an equal ability to induce gene transcription.

Deactivation of Smad2 and Smad3 is mediated by constitutively active phosphatases (66, 67). Therefore, a combined dephosphorylation and complex dissociated step was implemented, converting trimeric activated Smad complexes to unphosphorylated monomeric Smads. This process is constitutively active and does not depend on gene transcription.

Regardless of the phosphorylation state, Smad2, Smad3 and Smad4 continuously shuttle between cytoplasm and nucleus (219-221). Because nuclear/cytoplasm fractionation data were not acquired in this work, the nuclear and cytoplasmic compartments were not separately represented in the model.

Two transcriptional negative feedback loops were implemented.

"*Feedback 1*" corresponded to the combined action of the negative regulators that mediate proteosomal degradation of the activated receptor. This feedback loop included such candidates as transcriptionally-induced inhibitory Smads (Smad6 and Smad7) and the E3 ubiquitin ligases Smurf1/2 that are recruited to the receptor by the inhibitory Smads (37, 51, 52).

"*Feedback 2*" represented the combined effect of negative feedbacks that attenuate TGFβ pathway activation in a proteasome-independent manner. Mechanistically, this feedback is represented by the decoy pseudoreceptor BAMBI that forms inactive complex with type II TGFβ receptor (60), by PMEPA1, a TGFβ-induced protein that sequesters R-Smads (62), by FKBP12, a protein that competes with R-Smads for binding to the type I TGFβ receptor (61), SnoN and Ski proteins that can interfere with the ability of the TGFβ receptor to phosphorylate Smad2/3 (222).

The molecular inhibitors used in this study, actinomycin D (ActD), cycloheximide (CHX) and MG-132, were incorporated into the model according the mode of their action: ActD was modeled to block all processes of mRNA transcription (223); CXH inhibited mRNA-to-protein translation (224); and MG-132 blocked ubiquitin-mediated proteosomal degradation (225). All inhibitors were modeled to be 100% effective and stable within the experimental time frame. The full list of the dynamic variables, model reactions, conditions and equations is provided in the **section 6.3**.

2.3.4.2 Concentrations of endogenous Smad pathway components

The absolute abundance of the signaling components is the crucial determinant of the network wiring and its dynamic behavior (226). Therefore, to quantitatively assess the cell type-specific differences in the amounts of key TGFβ/Smad pathway components Smad2, Smad3 and Smad4 in the lung adenocarcinoma cell lines H1975, H838 and H1650, corresponding recombinant proteins (calibrators)

were used as spike-in standards for quantitative immunoblotting. The calibrators were expressed in *E. coli* as full-length proteins tagged with either streptavidin-binding peptide (SBP) or glutathione S-transferase (GST) to allow affinity-based purification using streptavidin- or glutathione-coated sepharose beads. In this way, the calibrators were slightly different in size compared to the corresponding endogenous protein, but contained the same epitope recognized by the respective antibody. The absolute amounts of Smad2, Smad3 and Smad4 were determined by quantitative immunoblotting using a calibration curve of calibrators (**Figure 2.19A**). For this purpose, different amounts of the respective calibrators were added to the same amount of the cellular lysate prior to performing an immunoprecipitation (IP) against Smad2/3 or Smad4. A calibration curve was generated from the calibrator signal and used to calculate the amount of endogenous Smad2, Smad3 and Smad4 proteins (**Figure 2.19B**). For H1975 cells, 160,000 molecules of Smad2, 190,000 molecules of Smad3 and 123,500 molecules of Smad4 were calculated on average per cell (**Figure 2.19C**). For H838 cells, 320,000 molecules of Smad2, 36,000 molecules of Smad3 and 110,000 molecules of Smad4 were estimated on average per cell (**Figure 2.19C**). For H1650 cells, 156,000 molecules of Smad2, 49,000 molecules of Smad3 and 27,000 molecules of Smad4 were estimated on average per cell (**Figure 2.19C**).

The number of molecules per cell scales with the cell size. Therefore, it is important to convert for each cell line molecules per cell to the absolute nanomolar concentrations. The cellular volumes of H1975, H838 and H1650 cells expressing the green fluorescent protein (GFP) were determined by confocal imaging. Resulting z-stacks were used for 3D image reconstruction using the Imaris software (Bitplane) that allows segmentation of the cell borders in the 3D space (**Figure 2.20A**). With this method, the mean volume of H1975 cells was estimated as 6500 μm^3, for H838 cells as 3920 μm^3 and for H1650 cells as 5130 μm^3 (**Figure 2.20B**). That allowed the conversion of absolute amounts of Smad2, Smad3 and Smad4 per cell to the respective concentration in nM (**Figure 2.20C**).

The accurate quantification of the number of molecules per cell adjusted for the differences in the cell volumes between the examined three LUAD cell lines revealed that H838 cells had approximately three times higher Smad2 concentration (133 ± 26 nM) than H1975 and H1650 cells (41 ± 15 nM and 36 ± 12 nM, respectively). The cell line H1975 had the highest concentration of Smad3 (48 ± 21 nM), which was approximately four times higher than in H838 cells (15 ± 5.5 nM) and H1650 cells (11 ± 4 nM). The cell line H1650 had the lowest concentration of Smad4 (6.3 ± 2.7 nM), whereas H1975 and H838 cells had comparably high concentrations of Smad4 (31.5 ± 15 nM and 46 ± 12 nM, respectively).

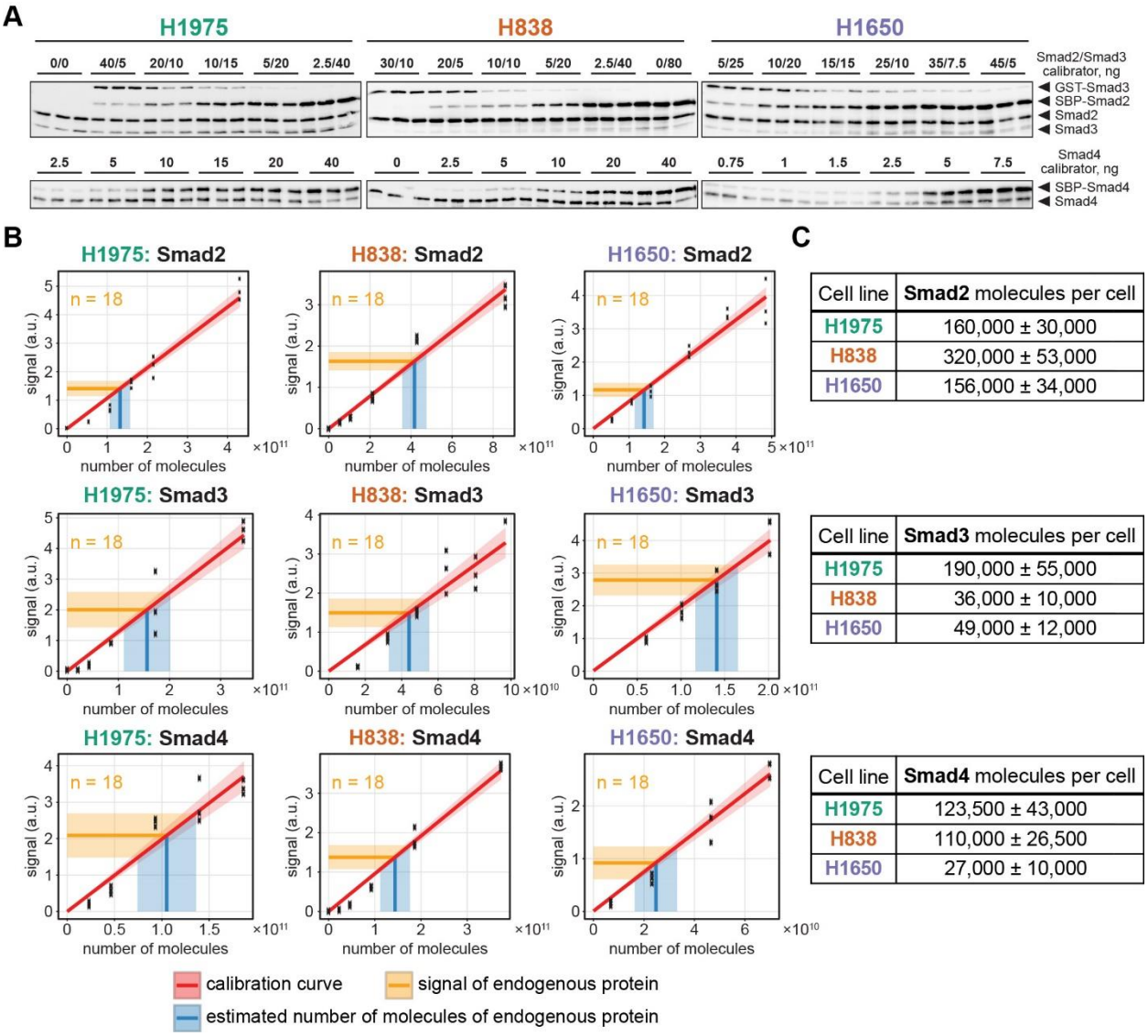

Cell line	**Smad2** molecules per cell
H1975	160,000 ± 30,000
H838	320,000 ± 53,000
H1650	156,000 ± 34,000

Cell line	**Smad3** molecules per cell
H1975	190,000 ± 55,000
H838	36,000 ± 10,000
H1650	49,000 ± 12,000

Cell line	**Smad4** molecules per cell
H1975	123,500 ± 43,000
H838	110,000 ± 26,500
H1650	27,000 ± 10,000

Figure 2.19. Absolute quantification of TGFβ/Smad pathway components. (**A**) Representative immunoblot of a dilution series of recombinant Smad2, Smad3 and Smad4 calibrator proteins. 8.3×10^5 H1975 cells, or 1.3×10^6 H838 cells, or 7.7×10^5 H1650 cells were lysed in whole-cell lysis buffer and subjected to immunoprecipitation (IP). Prior to IP, a dilution series of the recombinant streptavidine-binding peptide (SBP)- or glutathione S-transferase (GST)-tagged calibrators was spiked into the lysates. Smad2, Smad3 and Smad4 were visualized with chemiluminescence and detected using ImageQuant LAS 4000 imager. (**B**) Standard curves. The orange horizontal lines display the mean of 18 lysates probed for endogenous protein. Band intensities are converted to absolute numbers by using a calibration curve (red line). Black dots correspond to signals derived from spiked-in calibrators. Transparent ribbons correspond to standard deviations. Since a background subtraction was performed during immunoblot quantification, the linear regression was forced through zero. (**C**) Number of molecules per cell for Smad2, Smad3 and Smad4 as determined by IP from H1975, H838 and H1650 cell lysates. Data correspond to mean and standard deviation.

A

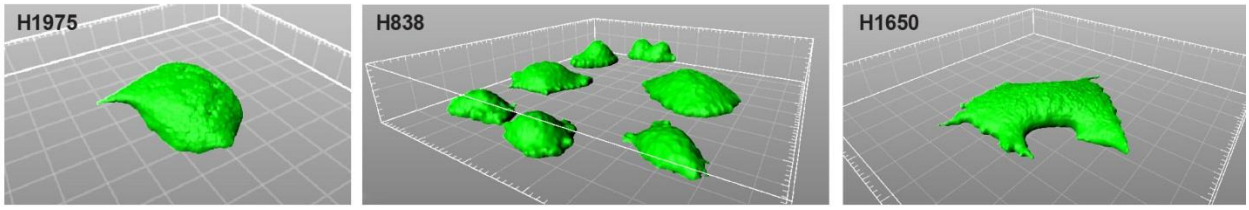

B

Cell line	Cell volume, µm³	n
H838	3920 ± 1245	21
H1975	6500 ± 2050	4
H1650	5130 ± 650	6

C

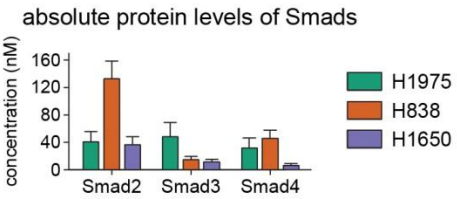

Figure 2.20. Conversion of absolute protein amounts to intracellular concentrations. (**A**) Representative reconstructed 3D microscopy images of H1975, H838 and H1650 cells. Cell constitutively expressing GFP were fixed with 3.7% paraformaldehyde and imaged using a LSM710 confocal microscope (Zeiss). 3D image reconstruction and volume estimation was performed with the Imaris software. Grid spacing corresponds to 10 µm. (**B**) Averaged values of cell volumes of H1975, H838 and H1650 cells. n indicates the number of analyzed cells. Data are presented as mean and standard deviation. (**C**) nM concentrations of the Smad2, Smad3 and Smad4 proteins in the examined LUAD cell lines. Error bars were calculated using an error propagation algorithm (**section 4.2.3**) to represent the uncertainty of the calibration curve, cell volume estimation and the number of lysed cells.

Overall, H1975 cells had comparable concentrations of all Smad signaling components, H838 cells had greater excess of Smad2 than Smad3 protein, while H1650 cells appeared to have the lowest levels of TGFβ/Smad pathway components among the studied LUAD cell lines. All resulting concentration values were used in the model to set the absolute scale for the model trajectories.

2.3.4.3 Identification of potential cell type-specific model parameters

In the first approximation the mathematical model was calibrated on the experimental data obtained in all three LUAD cell lines and did not include any cell type-specific parameters. Such model failed to describe all experimental data (**Figure S6.3**). To quantitatively assess potential cell type-specific differences in the regulation of the TGFβ pathway, the mRNA expression levels of "Feedback 1" and "Feedback 2" candidates as well as the levels of deubiquitinating enzymes controlling TGFβ receptor stability (227) were examined in unstimulated H1975, H838 and H1650 cells by whole-transcriptome RNA sequencing.

The mRNA expression of the inhibitory Smads, *SMAD6* and *SMAD7*, was the lowest in the H1975 cell line, and significantly higher in H838 and H1650 cells (**Figure 2.21A**). The mRNA abundance of the E3

ubiquitin ligases *SMURF1* and *SMURF2* was approximately twice higher in H1975 cells than in H838 and H1650 cells (**Figure 2.21A**). Additionally, mRNA levels of the *USP4* and *USP11* deubiquitinating enzymes that counteract the action of Smurf1/2 were twice higher in H838 cells than in H1975 and H1650 cells (**Figure 2.21B**). Overall, the "Feedback 1" was least pronounced H838 cells due to the highest expression levels of *USP4* and *USP11* combined with the lowest expression of *SMURF1* and *SMURF2*, whereas H1975 and H1650 cells had intermediate expression levels of "Feedback 1" candidates.

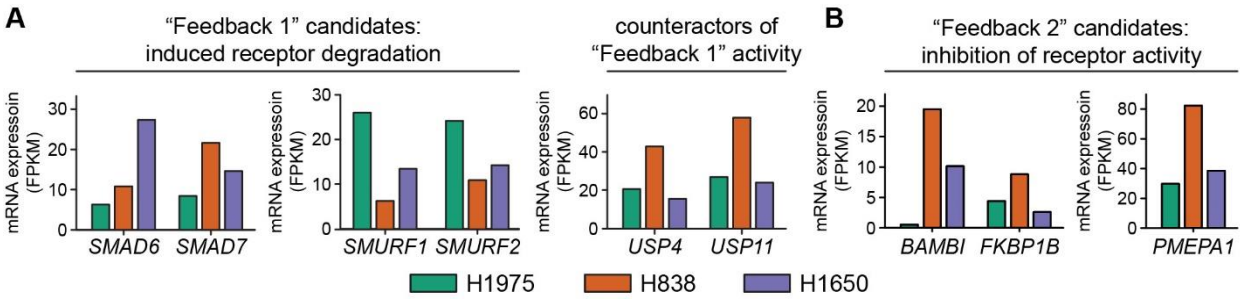

Figure 2.21. mRNA expression of genes controlling TGFβ pathway dynamics. Comparison of mRNA expression levels of genes mediating TGFβ receptor degradation (**A**), TGFβ receptor-specific deubiquitinating enzymes (**B**), and genes that reduce the ability of the receptor to phosphorylate Smads (**C**). H1975, H838 and H1650 cells were seeded two days prior the experiment. The following day cells were growth factor depleted for three hours, total RNA was extracted and sequenced using HiSeq 2000 (Illumina) by the Genomics & Proteomics Core Facility (DKFZ Heidelberg). Only one replicate per cell line was performed. The RNA sequencing results were aligned to the GRCh38 reference genome (Ensembl Release 79) and transcript quantification was performed using kallisto (228). Subsequent transcript abundances were summarized to the gene level for analysis using tximport (229). All ID mapping was performed using biomaRt (230) and genes with read counts <10 were filtered out. FPKM corresponds to "fragments per kilobase of transcript per million mapped reads". RNA extraction was performed by Ruth Merkle (DKFZ, Heidelberg). The analysis of RNA-Seq data was performed by Naveed Ishaque in the group of Benedikt Brors (DKFZ Heidelberg).

Expression of the "Feedback 2" candidates such as *BAMBI*, *FKBP1B* and *PMEPA1* was the lowest in the cell line H1975 (**Figure 2.21B**). Strikingly, *BAMBI*, a gene encoding a decoy TGFβ pseudoreceptor, was not expressed in H1975 cells. In contrast, the cell line H838 had the highest *BAMBI* mRNA expression, while the expression of *FKBP1B* and *PMEPA1* genes was two–three fold higher in H838 cells than in H1975 cells. H1650 cells had intermediate expression levels of "Feedback 2" candidates (**Figure 2.21B**). In sum, the "Feedback 2" candidates were most expressed in H838 cells, intermediate in H1650 cells, and the least expressed in H1975.

Based on these data as well on the differential responses of the cell lines to the inhibitor treatment (**Figure 2.17B**), four cell type-specific parameters were introduced: parameters describing the strength of "Feedback 1" (*k_rec_deg_feedback*) and "Feedback 2" (*k_inh*) feedback loops, parameters describing

ligand independent receptor degradation (*k_deg_Rec*) and feedback-independent degradation of the activated receptor (*k_deg_Rec_TGFb_const*).

The mathematical model was calibrated with 1703 data points that comprised data of TGFβ-induced dose- and time-resolved Smad2/3 phosphorylation and inhibitor perturbation experiments performed in H1975, H838 and H1650 cell lines. This dataset was used to estimate 19 dynamic parameters of the model, including four parameters that were cell type-specific.

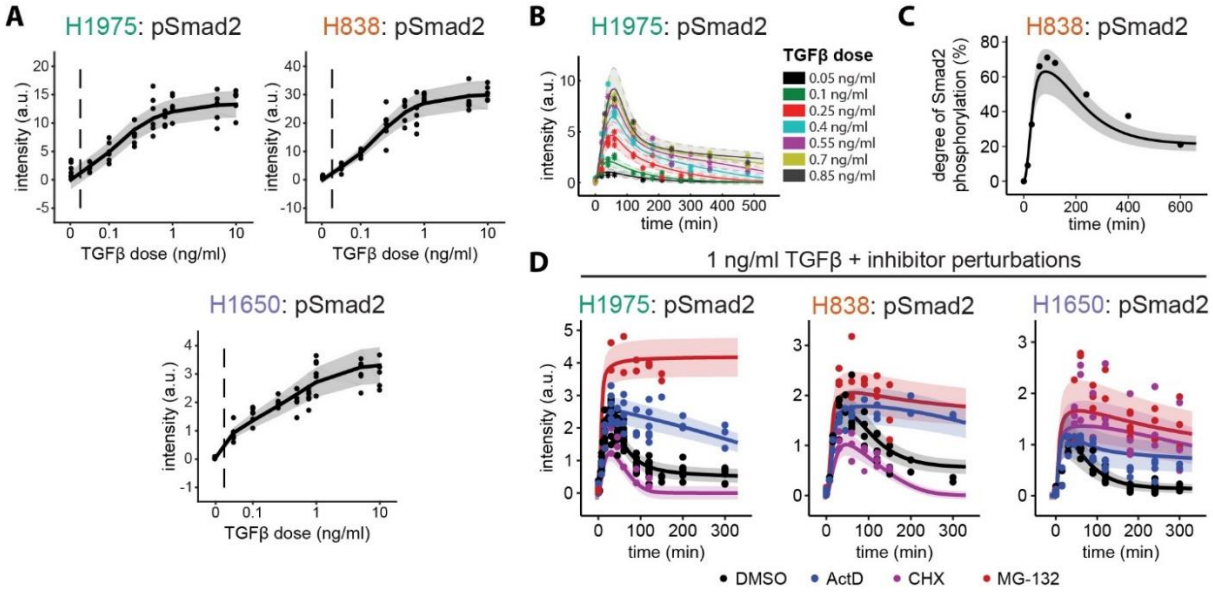

Figure 2.22. Model calibration with dose- and time-resolved experimental data of TGFβ-induced Smad2/3 phosphorylation in LUAD cell lines. For all experiments, growth factor-depleted H1975, H838 and H1650 cells were stimulated with indicated doses of TGFβ and Smad2/3 phosphorylation was measured with quantitative immunoblotting (**A**, **B** and **D**) or quantitative mass spectrometry (**C**). (**A**) Model fits of the dose-dependent Smad2/3 phosphorylation in H1975, H838 and H1650 cells that were stimulated with indicated TGFβ concentrations for 90 min. (**B**) Model fits of the dose- and time-dependent Smad2/3 phosphorylation in H1975 cells. (**C**) Model fits of the degree of Smad2 phosphorylation from whole-cell lysates of H838 cell stimulated with 1 ng/ml TGFβ. (**D**) Model fits of the inhibitor perturbations on the Smad2/3 time-resolved phosphorylation dynamics in H1975, H838 and H1650 cells stimulated with 1 ng/ml TGFβ. Experimental data are represented by circles; shaded areas correspond to 95% confidence interval estimated by the model. Solid lines are model trajectories. Representatively, just the model fits for Smad2 phosphorylation (pSmad2) are shown. Mass spectrometry measurements of Smad2 degree of phosphorylation were performed by Martin Böhm (DKFZ, Heidelberg). Model analysis was performed by Raphael Engesser (AG Timmer, Freiburg University).

When calibrated to the experimental data of this work, the model was able to recapitulate the dose-dependent Smad2/3 phosphorylation in H1975, H838 and H1650 cells (**Figure 2.22A**), as well as the densely sampled dose-resolved Smad2/3 phosphorylation time course in H1975 cells (**Figure 2.22B**). Relative intensities of Smad2 phosphorylation obtained with quantitative immunoblotting were

converted to absolute values by measuring the degree of Smad2 phosphorylation from whole-cell lysates of H838 cells using quantitative mass spectrometry. After 60 min of stimulation with 1 ng/ml TGFβ, ≈70% of Smad2 was phosphorylated (**Figure 2.22C**). Importantly, with cell type-specific parameters incorporated, the mathematical model successfully reproduced the cell type-specific differences of the inhibitor perturbations on the TGFβ-induced Smad2/3 phosphorylation dynamics in the cell lines H1975, H838 and H1650 (**Figure 2.22D**).

2.3.5 Model identifiability and profile likelihood analysis

To compare the cell type-specific parameters that define the distinct dynamic behavior of TGFβ-induced Smad2/3 phosphorylation and the impact of inhibitors in the examined LUAD cell lines, a model identifiability analysis was performed. The identifiability of model parameters is highly desired as only a model with a majority of identifiable parameters can make predictions about the dynamic behavior of model species that are not experimentally measured. A parameter is termed identifiable if its value can be estimated within certain a confidence interval (231). Importantly, when experimental data from several cell lines are used, only identifiable parameters can be compared in order to infer the cell type-specific wiring of the network.

The identifiability analysis of the model parameters was performed by calculating the profile likelihood estimates (PLEs). PLEs are calculated by iterative shifting a value of one parameter within $\vec{\theta}$ range around its previously defined optimum θ_0 and refitting all the other parameter values of the model for each θ_i (231). The procedure is repeated until either the threshold of the likelihood is reached or a maximal number of allowed iterations has passed. In case the likelihood of the fits is not changing within $\vec{\theta}$ range, the parameter is termed not identifiable. Structural and practical non-identifiabilities are distinguished (231). Practical non-identifiabilities emerge from insufficient amount or quality of the experimental data, while structural non-identifiabilities are theoretical properties of the model structure and originate from functionally-related and inter-dependent model parameters. Practical non-identifiabilities can be solved by performing new sufficiently information-rich experiments. To tackle structural non-identifiability, the model structure has to be reformulated or some parameter values have to be fixed (232).

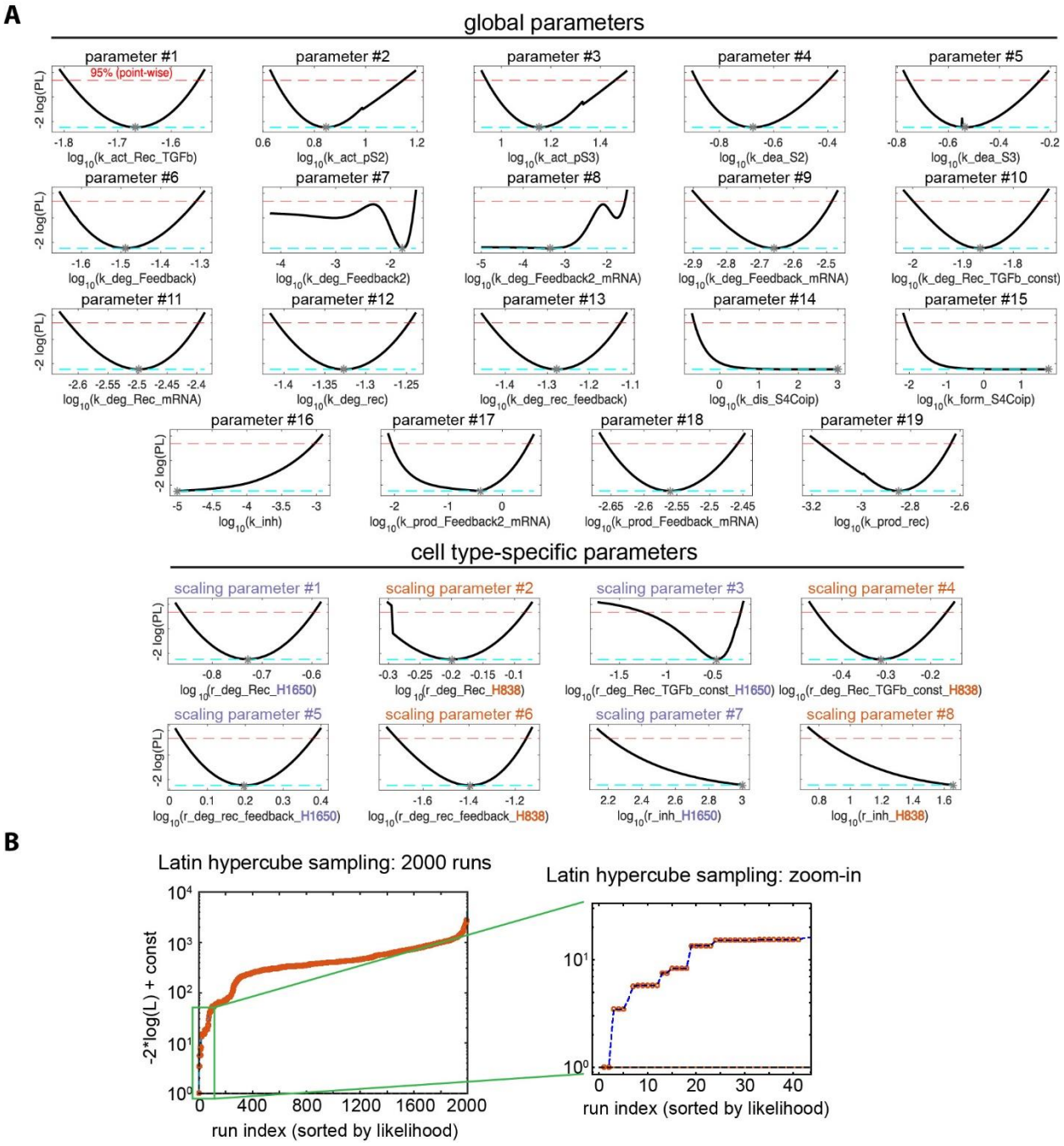

Figure 2.23. Model identifiability analysis for the calibrated TGFβ/Smad mathematical model. (**A**) Profile likelihood estimates of the model parameters. Solid black lines indicate the profile likelihood estimates. The upper red dashed lines indicate 95% confidence interval. The asterisks indicate the parameter of the best bit. Parameters written in black (1–19) are global, *r* parameters in orange and lilac (#20–26) are scaling factors for corresponding global dynamic parameters in H838 and H1650 cell lines, respectively. (**B**) Dynamic parameters of the model were iteratively randomly sampled 2000 times and goodness of the resulting fits were compared. Zoom-in plot demonstrates that among several local minima, potential global minimum was found at least twice. Model analysis was performed by Raphael Engesser (AG Timmer, Freiburg University).

Parameter identifiability analysis of the established mathematical model of TGFβ/Smad signal transduction was performed by calculating the PLEs (**Figure 2.23A**). The majority of the parameters were identifiable. Several practically not identifiable parameters included: (a) degradation rate of "Feedback 2" mRNA (parameter #8, *k_deg_Feedback2_mRNA*) and inhibition constant of "Feedback 2" (parameter #16, *k_inh*), suggesting the absence of a pronounced "Feedback 2" loop in the H1975 cell line; (b) the association and dissociation rates of Smad4 with phosphorylated Smad2/3 (parameters #14 and #15*,* *k_dis_S4Coip* and *k_form_S4Coip*, respectively) were interdependent, therefore the parameter value of the dissociation rate was fixed *k_dis_S4Coip* = 3, resulting in an identifiable parameter *k_form_S4Coip*.

The significant differences in cell type-specific parameter values were observed (**Figure 2.23A lower panel**). The rate of basal receptor turnover (dynamic parameter #12, and scaling parameters 20 and 21) was predicted to be the fastest in H1975 cells and 1.6 and 5.2 times slower in H838 and H1650 cells, respectively. Similarly, feedback-independent degradation of the activated receptor (dynamic parameter #10, and scaling parameters 22 and 23) was suggested to be most pronounced in H1975 cells, and two- and three-fold weaker in H838 and H1650 cells, respectively. Additionally, the model suggested that cell lines rely on different feedbacks to downregulate the TGFβ-induced pathway activation. The "Feedback 2" loop (dynamic parameter #16, and scaling parameters 26 and 27) was predicted to be completely absent in H1975 cells, while strongly pronounced in H1650 cells and less pronounced in H838 cells. The "Feedback 1" loop (dynamic parameter #13, and scaling parameters 24 and 25) was almost equally strong in H1650 and H1975 cells, but almost 25 times weaker in H838 cells.

Taken together, the model-based analysis suggested cell type-specific differences in the prevalence of "Feedback 1" and "Feedback 2" negative regulators, and in the processes that control TGFβ receptor turnover and stability.

2.3.6 Experimental validation of model predictions

2.3.6.1 Transcriptional negative feedback candidates

To test whether the model reliably predicted the differential prevalence of "Feedback 1" and "Feedback 2" transcriptional negative feedbacks between the cell lines, time-resolved mRNA expression of potential candidates, corresponding to both feedback branches, in response to TGFβ stimulation was assessed using qRT-PCR. Particularly, inhibitory Smads, *SMAD6* and *SMAD7* as well as the TβR1-specific

E3 ubiquitin ligases *SMURF1* and *SMURF2* were examined as "Feedback 1" candidates, whereas the mRNA expression of *SKI* and *SKIL* that interfere with formation of activated Smad complexes, as well as the expression of the pseudoreceptor *BAMBI* that forms an inactive complex with the TGFβ receptor, and *PMEPA1* that sequesters Smads from accessing the receptors were examined as potential "Feedback 2" candidates.

Unstimulated H1975 and H838 cells had comparable levels of *SMAD6* mRNA that was four times upregulated after two hours of TGFβ stimulation (**Figure 2.24A**). In H1650 cells, the basal expression of *SMAD6* was eight-fold higher than in H1975 and H838 cells, but in response to TGFβ stimulation the increase was only two-fold. The baseline expression of *SMAD7* mRNA was comparable in H838 and H1650 cells and was equally three-fold induced in both cell lines one hour after TGFβ stimulation (**Figure 2.24A**). In H1975 cells the initial *SMAD7* mRNA level was three times lower than in H838 and H1650 cells, but after one hour of TGFβ stimulation it increased to comparable level as in the TGFβ-treated H838 and H1650 cells.

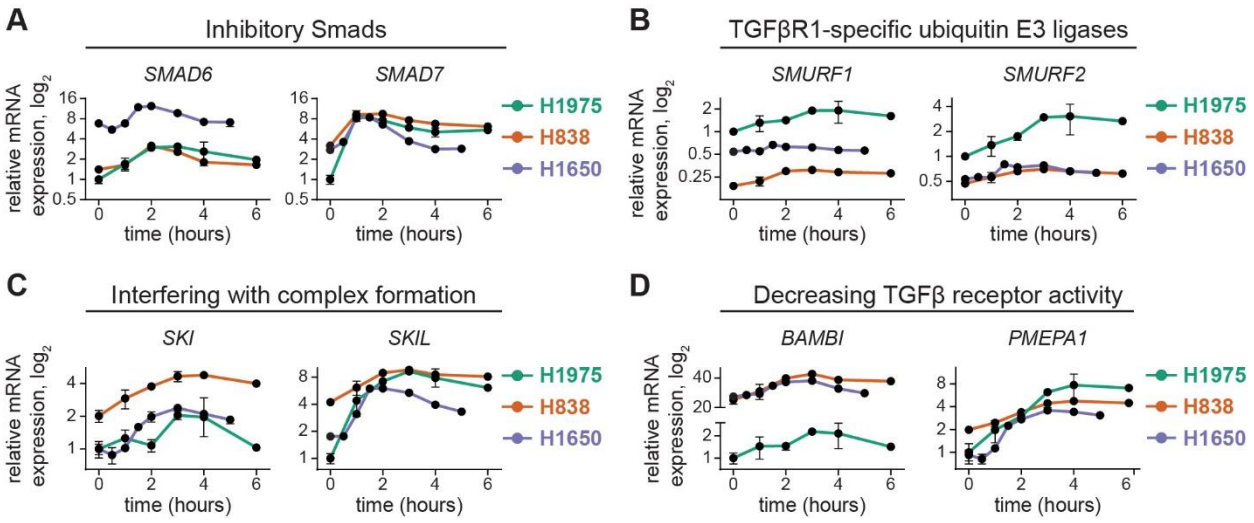

Figure 2.24. Upregulation of multiple negative feedback regulators in response to TGFβ treatment. H1975, H838 and H1650 cells were growth factor depleted for three hours and stimulated with 1 ng/ml TGFβ. Total RNA was extracted at the indicated time points and analyzed using qRT-PCR. Expression of the inhibitory Smads (**A**), TGFβR1-specific E3 ubiquitin ligases (**B**), Smad2/3-binding transcriptional co-repressors (**C**) and inhibitors of the TGFβ receptor activity (**D**) was examined. Error bars represent standard deviation of four biological replicates. mRNA expression was normalized to the geometric mean of four housekeepers: *GUSB*, *HPRT*, *GAPDH* and *G6PD*, and scaled to H1975 expression values.

Basal *SMURF1* expression differed between the three examined LUAD cell lines (**Figure 2.24B**). H1975 cells had the highest *SMURF1* mRNA abundance, H1650 cells – twice lower than H1975 cells, and H838 cells – eight times lower than H1975 cells. TGFβ stimulation resulted in two-fold upregulation of

SMURF1 mRNA in H1975 and H838 cells, while in H1650 it remained unchanged. Similarly to *SMURF1* expression, H1975 cells had the highest level of *SMURF2* mRNA that was further three-fold upregulated after three hours of TGFβ stimulation (**Figure 2.24B**). In contrast, the basal expression of *SMURF2* in H838 and H1650 cells was twice lower than in H1975 cells and was only slightly increased in response to TGFβ treatment.

Expression of the *SKI* and *SKIL* genes that encode proteins that interfere with Smad complex formation was the highest in H838 cells and further two-fold increased after three hours of TGFβ stimulation (**Figure 2.24C**). Basal level of *SKI* mRNA in H1975 and H1650 cells was twice lower than in H838 cells and was also two-fold upregulated in response to TGFβ treatment. *SKIL* expression in unstimulated H1975 cells was eight times lower than in H838 cells, but increased eight times after three hours of TGFβ stimulation and reached the same level as in TGFβ-treated H838 cells (**Figure 2.24C**). Basal level of *SKIL* mRNA in H1650 cells was twice higher than in H1650 cells and was two-fold induced after two hours of TGFβ treatment.

Strikingly, *BAMBI* expression in H1975 was 20-fold lower than in H838 and H1650 cells (**Figure 2.24D**). TGFβ stimulation caused two-fold increase in *BAMBI* mRNA amount after three hours of treatment in all three cell lines. Baseline expression of *PMEPA1* was twice higher in H838 cells than in H1975 and H1650 cell lines (**Figure 2.24D**). In response to TGFβ treatment *PMEPA1* mRNA expression increased eight-fold in H1975 cells, four-fold in H1650 cells and two-fold in H838 cells.

Overall, these results confirmed the model prediction that the “Feedback 1” is the major control mechanism of TGFβ-induced Smad2/3 phosphorylation dynamics in H1975 cells, since H1975 cells contain the highest initial levels of *SMURF1/2*, the highest fold induction of *SMAD6* and *SMAD7* (three-fold and eight-fold, respectively), and the lowest expression of *BAMBI*.

Similarly, these data confirmed the model prediction that “Feedback 2” was most pronounced in H838 cells because H838 cells contained the lowest levels of *SMURF1* and *SMURF2*, the lowest fold change in *SMAD6* and *SMAD7* expression (two-fold for both), and the highest basal expression of “Feedback 2” genes: *SKI*, *SKIL*, *BAMBI* and *PMEPA1*.

Finally, the cell line H1650 showed reliance on “Feedback 1” and “Feedback 2” because H1650 cells contained the highest level of *SMAD6* expression and intermediate *SMURF1* mRNA expression, a high level of *BAMBI*, and an intermediate basal expression of *SKIL*.

Taken together, these results revealed that the examined LUAD cell lines differ with respect to the prevalence of “Feedback 1” and “Feedback 2” candidates. This highlighted that the examined lung cancer cell lines utilize different negative regulators and their combinations to downregulate the TGFβ-induced Smad2/3 phosphorylation.

2.3.6.2 siRNA knockdown of negative feedback players

The time-resolved analysis of mRNA expression in TGFβ-treated H1975, H1650 and H838 cells revealed that multiple transcriptional negative feedbacks are differentially upregulated in response to TGFβ treatment. In particular, inhibitory Smads, *SMAD6* and *SMAD7*, both belong to “Feedback 1”, showed differences in basal mRNA expression as well as in fold change induction in response to TGFβ treatment (**Figure 2.24A**). Importantly, Smad7 is widely considered as the predominant negative regulator that antagonizes TGFβ signaling (37, 233). Therefore, to investigate the functional importance of Smad6 and Smad7 as negative feedback regulators in the context of lung cancer cell lines, siRNA-mediate knockdown of either *SMAD6*, or *SMAD7*, or their combination, was performed and the resulting Smad2/3 phosphorylation dynamics was measured by quantitative immunoblotting.

Knockdown of *SMAD6* or *SMAD7* with corresponding siRNAs in unstimulated H1975, H838 and H1650 cells resulted in 85–95% reduction of basal *SMAD6* or *SMAD7* mRNA levels (**Figure 2.25A**). However, only a 50% reduction of *SMAD7* mRNA was achieved in H1975 cells. After stimulation with TGFβ for 1 hour the amount of *SMAD7* mRNA increased to 611% in H1975 cells, to 307% in H838 cells and to 383% in H1650 cells. A similar induction was observed in cells transfected with *SMAD7* siRNA, but the overall amount of *SMAD7* mRNA remained four–six times lower than in TGFβ-treated cells transfected with non-targeting siRNA. TGFβ stimulation caused a 120% increase in *SMAD6* mRNA abundance in H1975 cells, 28% increase in H838 cells and 20% increase in H1650 cells. In cells with *SMAD6* knockdown, TGFβ stimulation also triggered the upregulation of the *SMAD6* mRNA amount, but to a lower degree. Overall, knockdown of both *SMAD6* and *SMAD7* was more effective in H838 and H1650 cells than in the cell line H1975.

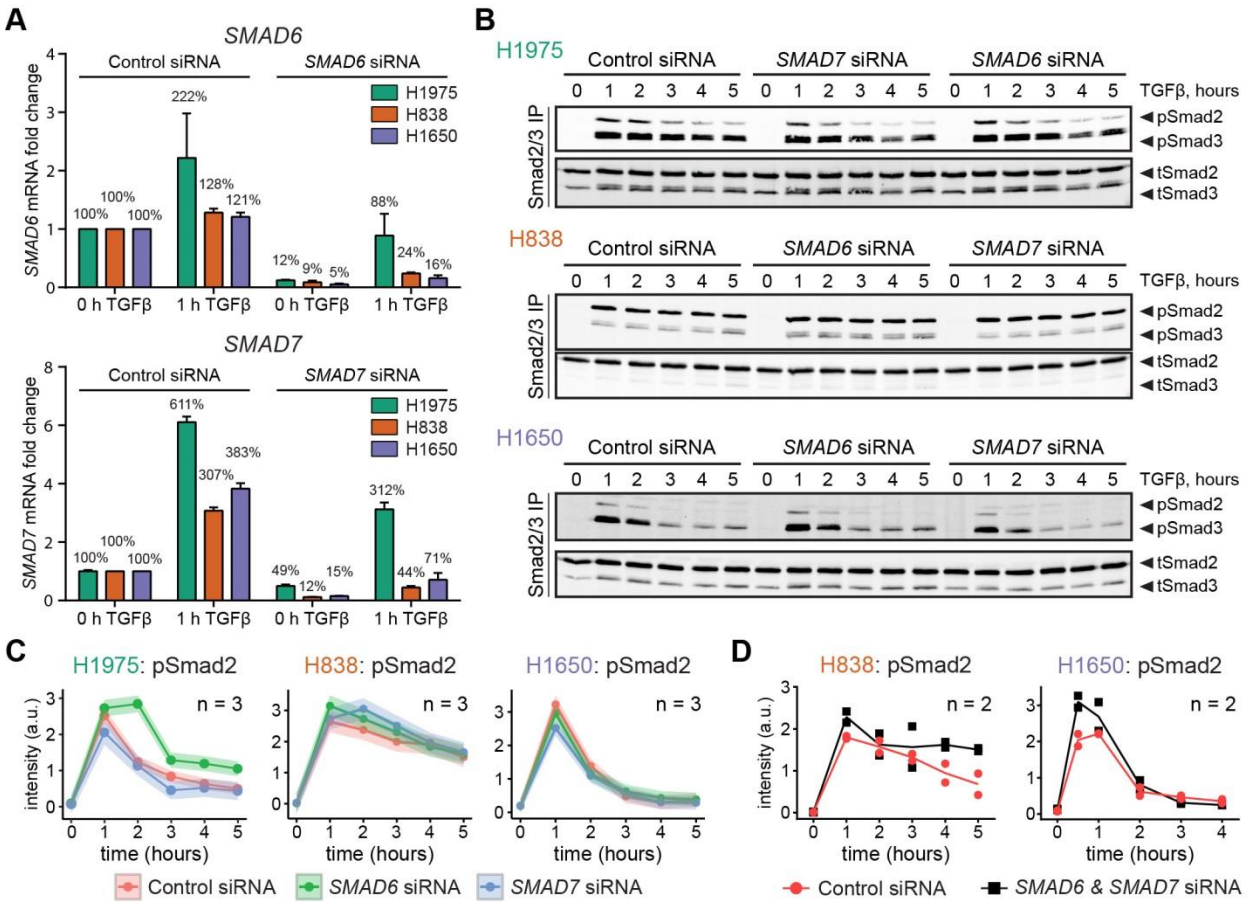

Figure 2.25. Effect of knockdown of inhibitory Smads on the dynamic behavior of TGFβ-induced Smad2/3 phosphorylation. H1975, H838 and H1650 cells were transfected with 10 nM siRNA directed against either Smad6, or Smad7. Experiments started 36 hours after siRNA transfection. (**A**) Efficiency of the *SMAD6* and *SMAD7* knockdowns. Cells were growth factor depleted for three hours and stimulated for 1 hour with 1 ng/ml TGFβ or left untreated, mRNA was extracted and expression of *SMAD6* and *SMAD7* genes was analyzed using qRT-PCR. Error bars represent standard deviation of six biological replicates. mRNA expression was normalized to the geometric mean of four housekeepers: *GUSB*, *HPRT*, *GAPDH* and *G6PD*. For each cell line the data data were scaled to TGFβ-untreated cells transfected with non-targeting siRNA. (**B**) Representative immunoblots of Smad2/3 phosphorylation dynamics. Cell were growth factor depleted for three hours, stimulated with 1 ng/ml TGFβ and lysed at the indicated time points. Subsequently, cellular lysates were subjected to immunoprecipitation with antibodies against Smad2/3 and analyzed using quantitative immunoblotting. Proteins were visualized with far-red fluorescence and detected using Odyssey infrared imager. Total (tot) and phosphorylated (p) levels of Smad2 and Smad3 were assessed. (**C** and **D**) Scaled pSmad2 intensities from several independent experiments using BlotIt script (210). For simplicity only pSmad2 quantifications are shown, because dynamics of Smad2 and Smad3 phosphorylation were similar. Error bars correspond to standard error estimated by the BlotIt package for R developed by Dr. Daniel Kaschek; n indicates number of independent experiments.

Next, the TGFβ-induced Smad2/3 phosphorylation dynamics was examined in H1975, H838 and H1650 cells transfected with either *SMAD6*, or *SMAD7*, or control non-targeting siRNAs (**Figure 2.25B**). Downregulation of *SMAD7* expression in H1975 cells resulted in a slight decrease in the TGFβ-induced Smad2/3 phosphorylation, while *SMAD6* knockdown in H1975 cells prolonged the peak duration of

TGFβ-induced Smad2/3 phosphorylation (**Figure 2.25C**). In H838 cells, knockdown of either *SMAD6* or *SMAD7* only marginally increased the amplitude of Smad2/3 phosphorylation and reduced the extent of signal decline. A marginal decrease in Smad2/3 phosphorylation in response to TGFβ stimulation was observed in H1650 cells upon siRNA-mediated *SMAD6* or *SMAD7* downregulation.

To exclude the possibility that Smad6 and Smad7 have redundant roles and might compensate for each other, the double knockdown was performed. In H838 cells, the combined downregulation of *SMAD6* and *SMAD7* mRNA expression, increased the amplitude of TGFβ-induced Smad2/3 phosphorylation as well as decreased the extent of signal decline (**Figure 2.25D**). This effect was more pronounced than in the case of the single *SMAD6* and *SMAD7* knockdowns. In contrast to single *SMAD6* and *SMAD7* knockdowns that showed only a marginal effect on the TGFβ-induced Smad2/3 phosphorylation dynamics in H1650 cells (**Figure 2.25C**), the combined knockdown of both negative regulators increased the maximal amplitude of Smad2/3 phosphorylation by 50%, but did not affect the signal decrease afterwards (**Figure 2.25D**).

Overall, these results showed that although Smad6 and Smad7 proteins contribute to the negative regulation of the TGFβ-induced Smad2/3 phosphorylation in the examined LUAD cell lines.

2.3.6.3 TGFβ receptor mRNA stability

Implementing constant ligand-independent receptor turnover into the model structure was essential to explain the discrepancies between the effects of cycloheximide and actinomycin D inhibitors on the TGFβ-induced Smad2/3 phosphorylation dynamics in the cell lines H1975 and H838 (**Figure 2.17**). The model-based hypothesis suggested that the TGFβ receptor protein has a relatively short half-life and undergoes constant cycles of production from relatively stable mRNA followed by rapid proteasome-mediated degradation. The inhibition of mRNA translation with actinomycin D does not affect the protein abundance of the TGFβ receptor because the corresponding mRNA is still present, whereas inhibition of protein translation with cycloheximide results in the decrease of the TGFβ receptor protein level.

To confirm the model-predicted high stability of the TGFβ receptor mRNA, the half-lives of *TGFBR1* and *TGFBR2* mRNAs were measured by treating growth factor-depleted H1975, H838 and H1650 cells with 2 ng/ml actinomycin D and extracting RNA at specific time points to up to ten hours. Gene expression was

measured using qRT-PCR and a two-parameter exponential decay function was fitted to the mRNA expression data. Additionally, the stability of *SMAD7* mRNA was assessed as an example of a gene with a relatively short mRNA half-life (234).

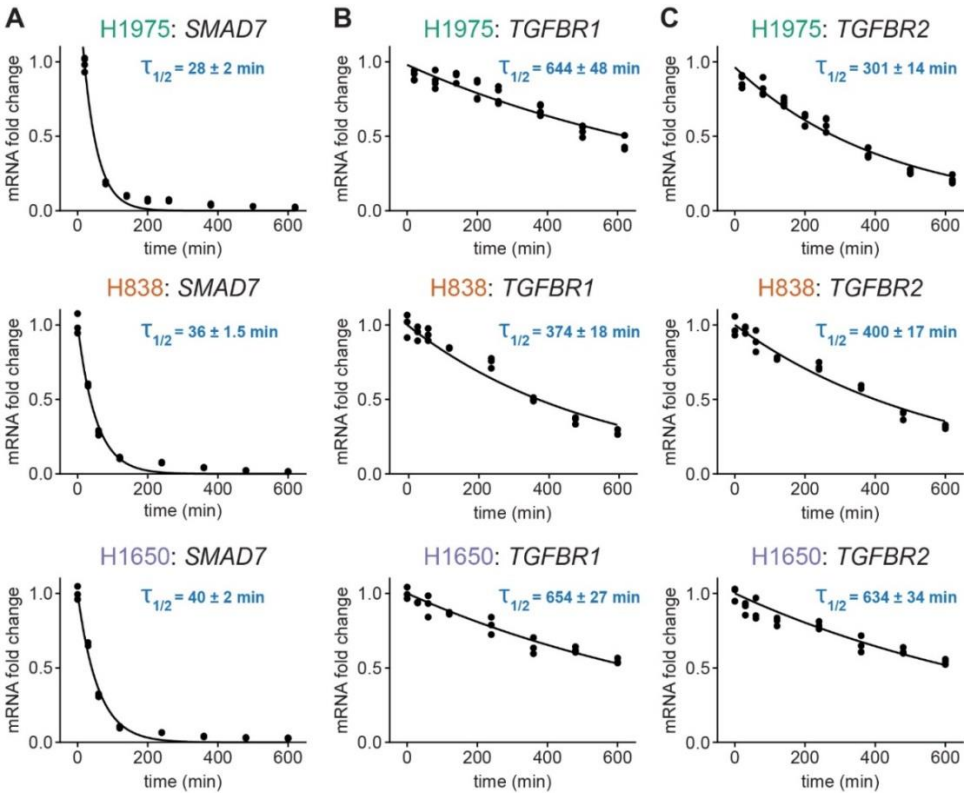

Figure 2.26. Quantification of mRNA half-lives. H1975, H838 and H1650 cells were growth factor depleted for three hours and treated with 2 ng/ml actinomycin D for the indicated time points. Total RNA was extracted and analyzed by qRT-PCR. mRNA stability of *SMAD7* (**A**), *TGFBR1* (**B**) and *TGFBR2* (**C**) genes was assessed. Each filled circle corresponds to a biological replicate. Regression line: two-parameter exponential decay function. mRNA expression was not normalized to the housekeeper genes. *SMAD7* mRNA half-life is displayed as an example of a gene with a very short half-life time.

The mRNA half-life of the *SMAD7* mRNA in the H1975, H838 and H1650 cell lines was in the range of 28–40 min (**Figure 2.26A**). These estimations were in line with the literature values of approximately 40 min (234). These results confirmed that the established assay provides reliable values of mRNA half-lives.

The half-life of the *TGFBR1* mRNA was estimated as 650 min in H1975 and H1650 cell lines, and as 370 min in H838 cells (**Figure 2.26B**), while the half-life of *TGFBR2* mRNA was 300 min in H1975 cells, 400 min in H838 cells and 630 min in H838 cells (**Figure 2.26C**).

In sum, the measured *TGFBR1* and *TGFBR2* mRNA half-lives well exceed the time frame of the signaling experiments (**Figure 2.17**). Therefore, these results confirmed the model-based assumption of a high stability of TGFβ receptor mRNA.

2.3.6.4 TGFβ depletion

The mathematical model predicted that the inhibition of ubiquitin-dependent protein degradation with MG-132 increases the amount of the TGFβ receptor, blocking protein translation with cycloheximide reduces its levels, while actinomycin D does not affect the TGFβ receptor protein expression. The change in the receptor amount directly affects the receptor-mediated TGFβ ligand depletion from the cell culture supernatants of TGFβ-treated cells.

To experimentally test the impact of actinomycin D, cycloheximide and MG-132 inhibitors on TGFβ depletion, H1975, H838 and H1650 cells were pre-treated for 30 min with the respective inhibitors and were stimulated with 1 ng/ml TGFβ. Medium supernatants were collected at the indicated time points, were centrifuged to eliminate cellular debris and were analyzed using multiplex bead-based array.

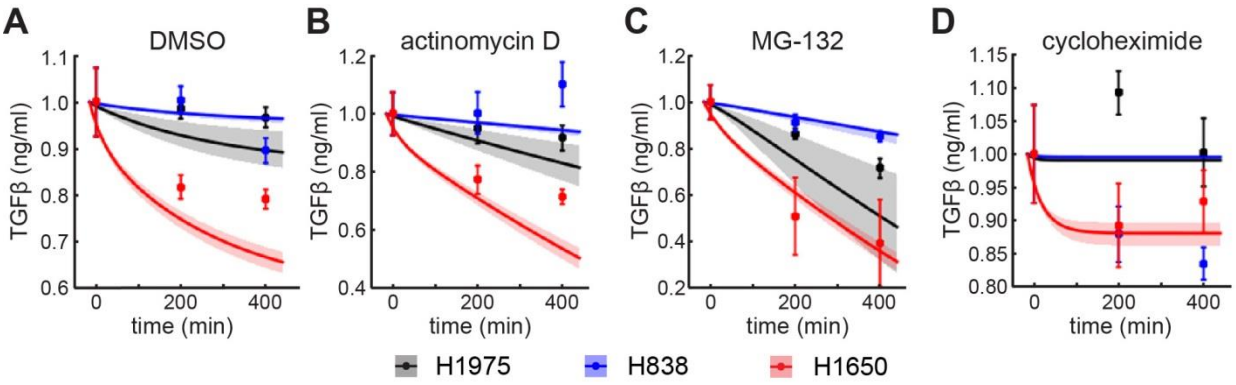

Figure 2.27. Model prediction and experimental validation for TGFβ depletion. H1975, H838 and H1650 cells were growth factor depleted for three hours, pre-treated for 30 min with either DMSO (**A**), or actinomycin D (**B**), or MG-132 (**C**) or cycloheximide (**D**) and stimulated with 1 ng/ml TGFβ. The medium supernatant at the indicated time points was collected and TGFβ concentration was measured using multiplex bead-based array. Experimental data are represented by filled circles, error bars correspond to standard deviation from biological triplicates. Solid lines represent model predictions. Shaded areas correspond to 95% confidence interval estimated by the model. Model analysis was performed by Raphael Engesser (AG Timmer, Freiburg University).

In unperturbed cells, TGFβ ligand was depleted the fastest by H1650 cells, intermediate by H1975 cells and the least depleted by H838 cells (**Figure 2.27A**). In all tested cell lines inhibition of mRNA transcription with actinomycin D (ActD) did not significantly change ligand depletion in comparison with

DMSO-treated cells (**Figure 2.27B**). In comparison with DMSO-treated cells, inhibition of proteosomal protein degradation with MG-132 increased the TGFβ depletion, especially in H1650 and H1975 cells (**Figure 2.27C**). Blocking protein translation with cycloheximide completely abolished ligand depletion by H1975, H838 and H1650 cells (**Figure 2.27D**). Overall, the model simulations were in line with the experimental data. However, the model slightly overestimated the TGFβ depletion by unperturbed and ActD-treated H1650 cells suggesting the existence of additional levels of regulation present in this cell line that was not yet represented in the model.

In sum, these results indirectly confirmed the model-predicted change in the abundance of the TGFβ receptor in the examined LUAD cell lines upon treatment with MG-132 and cycloheximide inhibitors.

2.3.6.5 TGFβR1 protein abundance

To directly validate the model-predicted increase in the TGFβ receptor levels upon inhibition of the proteasome-mediated degradation with MG-132, the protein level of the receptor has to be experimentally assessed. Particularly, the expression of TβR1 is of prime interest as it controls the canonical TGFβ/Smad pathway, while TβR2 initiates mainly non-Smad pathways (235).

However, it is very difficult to accurately quantify the abundance of the receptor with conventional antibody-based techniques due to specific features of the TβR1. The receptor has low abundance as the number of total receptor molecules per cell was estimated at around 10,000 in the lung adenocarcinoma cell line A549 based on iodinated-TGFβ binding assay (236). There are no reliable antibodies available (237) and its molecular size of 52 kDa is relatively close to the molecular weight of the heavy chain of antibodies making the immunoblot detection of the TGFβR1 protein difficult after immunoprecipitation-based enrichment. Therefore, a mass spectrometric (MS)-based approach was chosen to measure the TGFβ receptor abundance.

The most commonly used method in mass spectrometric proteomics is the untargeted shotgun approach. In this mode, the mass spectrometer always selects the most abundant peptides that elute at a given time from a chromatography column for fragmentation analysis. Up to 10,000–12,000 proteins can be identified per a sample with such approach (238). However, very low abundant proteins are very unlikely to be discovered in a shotgun mode because their peptides very seldom range among the most abundant. In a targeted mode the mass spectrometer is programmed to measure MS/MS of only certain

peptides at certain times defined by an inclusion list. This way it is able to detect even very low abundant peptides in complex samples, but is “blind” for all other peptides. Parallel reaction monitoring (PRM) has emerged as a reliable targeted method to detect and quantify low-abundant proteins (**Figure 2.28A**) (239).

Stable heavy isotope-labeled internal standards can be applied to normalize peptide signals in MS measurements and hence improve quantification (240). Such standards have the same chemical properties and therefore the same retention time on HPLC column as the endogenous peptides, but a different m/z ratio and therefore can be discriminated by the mass spectrometer. When spiked into samples early in the sample preparation procedure, it helps to normalize for peptide losses during sample preparation, digestion and dilution and allows the confident comparison of protein levels across different samples.

To create a heavy standard, the intracellular domain of TβR1 tagged with glutathione S-transferase (GST) was expressed in *E. coli* growing in the minimal medium containing stable ^{15}N heavy isotopes and subsequently purified using affinity purification (**Figure 2.28B**). The mass spectrometer was scheduled to detect five TβR1 peptides originating from its intracellular domain as well as their N^{15}-heavy-labeled counterparts (**Figure 2.28C**). For each measured peptide, six most abundant fragments were used to quantify the intensity of the precursor peptide (**Figure 2.28D left panel**).

For each of the six fragments, the light-to-heavy ratio was measured and the median of six ratios was used to estimate light-to-heavy ratio of the given peptide (**Figure 2.28D right panel**). Similarly, the median ratio of all TβR1 peptides was calculated to estimate the receptor abundance in the given sample. Finally, because the amount of heavy calibrator used per sample was known, as well as the number of lysed cells per sample and their corresponding cell sizes (**Figure 2.20**), resulting light-to-heavy ratios (**Figure 2.28E**) can be converted to absolute nM concentration of TβR1 protein in examined LUAD cell lines (**Figure 2.28F**).

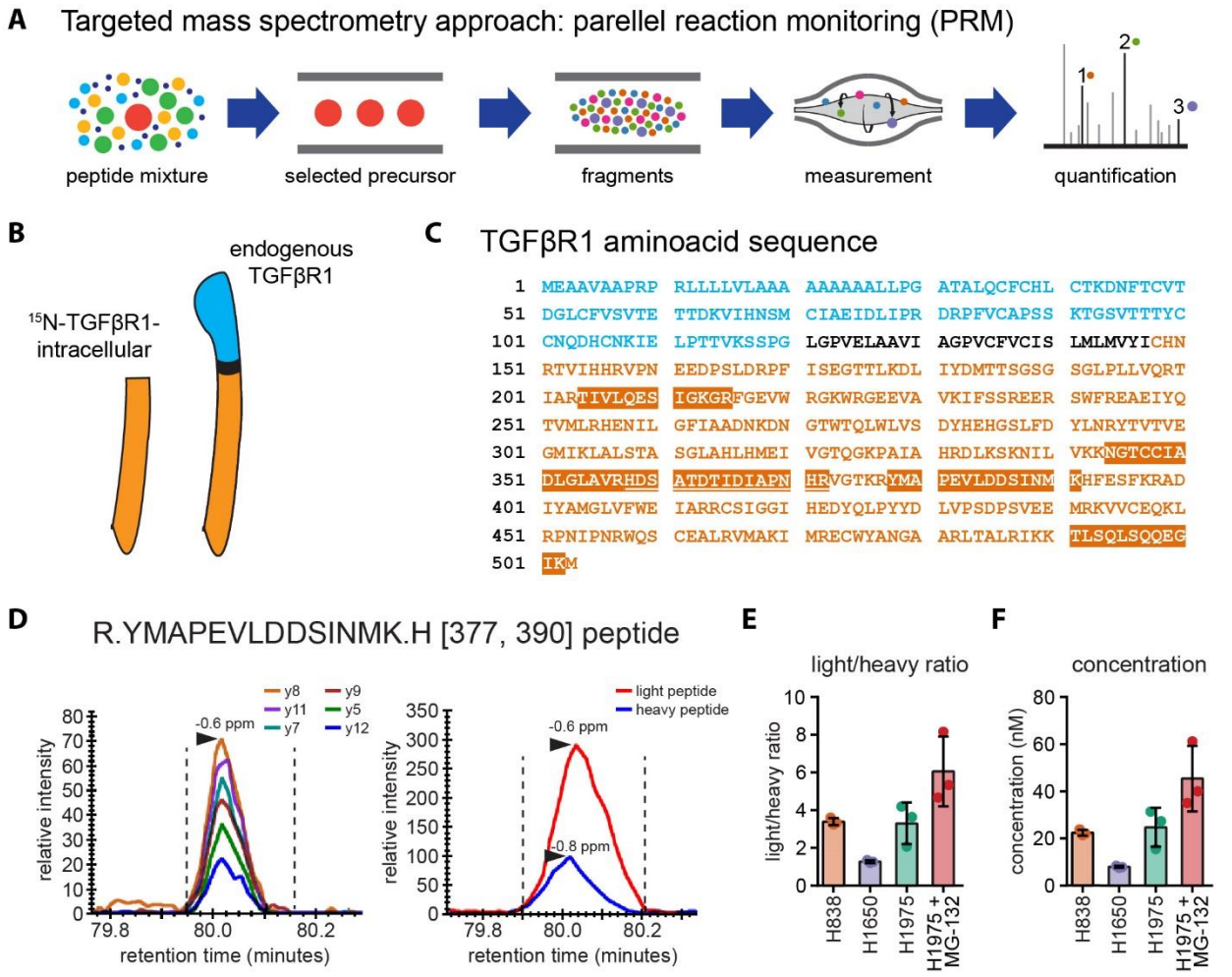

Figure 2.28. Measuring TGFβR1 protein abundance using targeted mass spectrometry. (**A**) Scheme of PRM approach. Low abundant peptides of interest are scheduled with a given m/z ratio and retention time. Selected precursors are fragmented and measured on orbitrap. Intensities of the selected fragments are used for quantification. (**B**) Scheme of endogenous TGFβR1 protein structure and recombinant ^{15}N-labeled calibrator consisting of cytoplasmic domain of the receptor. Cytoplasmic domain is orange, transmembrane domain is black, extracellular part is blue. (**C**) TGFβR1 aminoacid sequence. Five peptides that were measured using PRM approach are highlighted. In case two peptides follow each other in a sequence, the second peptide is underscored. (**D**) Exemplary elution profiles of one TGFβR1 peptide (YMAPEVLDDSINMK) measured in PRM mode. Left, six most abundant precursor fragments used for quantification of a given peptide. Accuracy of measured and theoretical masses is indicated on top of the peak. Right, profiles of co-eluting endogenous and corresponding ^{15}N-heavy labeled peptide. 2.5 ng of the calibrator was added per sample. Summed intensity of all six transitions is compared, and light-to-heavy ratio is quantified for every selected peptide. (**E**) Light-to-heavy TGFβR1 ratios in the LUAD cell lines. H1975, H838 and H1650 cells were growth factor depleted for three hours, H1975 cells were additionally treated for 30 min with proteasome inhibitor MG-132. Cells were lysed in whole cell lysis buffer containing 0.1% Rapigest. The entire lysate was used for IP against TGFβR1. Additionally, 2.5 ng of ^{15}N-labeled TGFβR1 calibrator comprising the intracellular domain the receptor was spiked-in per sample. After overnight IP, samples were on-beads digested with LysC and trypsin, desalted using self-made StageTips (241) and measured using Q Exactive Plus Hybrid Quadrupole-Orbitrap mass spectrometer. Data analysis performed in Skyline (242). Data presented as mean and SD. Filled circles correspond to biological replicates. Heavy calibrator was produced and purified by Elinor Boos (DKFZ, Heidelberg). (**F**) Conversion from light/heavy ratio to TGFβR1 concentrations was performed by using the cell volume of H1975, H838 and H1650 cells that was previously measured by confocal microscopy.

Using this approach the basal concentration of the type I TGFβ receptor was estimated approximately at 23 nM in both H1975 and H838 cells (**Figure 2.28F**). Surprisingly, despite the highest rate of TGFβ ligand depletion among the examined LUAD cell lines (**Figure 2.27A**), H1650 cells had an approximately three-fold lower TβR1 concentration (8 ± 0.45 nM) than H1975 and H838 cells (**Figure 2.28F**). Most importantly, the inhibition of proteasome-mediated protein degradation with MG-132 in unstimulated H1975 cells resulted in a two-fold increase of TGFβR1 expression level reaching 45 nM (**Figure 2.28F**). In sum, these results directly confirmed the model-predicted increase in the abundance of the TGFβ receptor in H1975 cells treated with MG-132, and confirmed a differential expression of the TβR1 protein in the examined LUAD cell lines.

Taken together, the presented mathematical modeling approach combined with iterative quantitative experiments uncoved the underlying mechanisms controlling the dynamic properties of the TGFβ signal transduction pathway in lung adenocarcinoma cell lines. The systematic analysis revealed distinct dynamic behavior of TGFβ-induced Smad2/3 phosphorylation and a differential impact of inhibitors in the examined LUAD cell lines. These features were mediated by the different prevalence of negative feedbacks that induce the degradation of the TGFβ receptor or reduce its ability to phosphorylate Smads. Importantly, the model-based analysis predicted that the TGFβ receptor protein undergoes constant turnover: the unstable receptor protein is constantly degraded and produced again from the stable receptor mRNA. High stability of the TGFβ receptor mRNA was confirmed by mRNA half-life analysis, while the accumulation of the TGFβ receptor protein upon inhibition of the proteasome function was validated using targeted quantitative mass spectrometry. These findings highlighted that the TGFβ receptor is one of the most sensitive nodes that controls pathway activation. Therefore, targeting processes that control receptor abundance rather than using conventional TGFβ receptor kinase inhibitors could be a promising therapeutic approach.

3 Discussion

3.1 Mechanisms causing TGFβ pathway deregulation in lung cancer

The results reported in this subsection have been previously published in their original or modified form in Marwitz*, Depner*, Dvornikov* et al. 2016 (189).

3.1.1 Activation of the TGFβ pathway in human lung tumors

In the context of carcinogenesis the TGFβ signaling cascade is viewed as a double-edged sword. At pre-malignant stages this pathway promotes anti-proliferative and pro-apoptotic responses. However in advanced tumors TGFβ mediated immunosuppression and enhancement of invasion promote metastatic spread (243). In lung cancer, high TGFβ serum levels correlate with poor prognosis, lymph node metastasis and tumor progression (124). Furthermore, the expression of TGFβ was identified as an independent risk factor for the occurrence of pulmonary metastasis in NSCLC (244).

In this work, a comprehensive in-depth analysis of the status of the TGFβ signaling pathway in lung cancer tissues is presented. Strikingly, downregulation of the TGFβ pseudoreceptor BAMBI was found to be the most consistent feature among multiple lung cancer samples. In line with this observation abundant activation of the TGFβ signaling pathway, indicated by the phosphorylation of both R-Smads, was observed. On the contrary, in colon carcinomas mutations in *TGFBR2* (245) and *SMAD4* (100, 101) are frequently observed resulting in the deactivation of the signaling pathway. In NSCLC mutations in the receptor (167), the intracellular signal mediators Smad2 (246) or Smad4 (247) are rare. Therefore NSCLC seem to retain a functional and active signaling cascade similarly to breast cancer (243) supporting a pro-tumorigenic role of TGFβ in both types of carcinomas.

The pseudoreceptor BAMBI is a classical decoy receptor: it consists of the extracellular domain that is highly homologous to type I TGFβ receptor, but lacks the intracellular kinase domain (60) (**Figure 3.1**). Therefore, BAMBI can form an inactive complex with type II TGFβ receptor upon binding to the TGFβ ligand, limiting the downstream pathway activation. Currently the role of BAMBI in various cancers is controversially discussed. Increased BAMBI expression has been reported for colorectal cancer tissues (248, 249) and ovarian cancer cells (250). In contrast, BAMBI was observed to be epigenetically silenced in high-grade bladder cancer (251) and absent in metastasizing melanoma cells (252) and breast cancer tissues (253). Similarly, the results of this work demonstrate that in lung cancer tissues in contrast to matched tumor-free controls, the *BAMBI* gene is epigenetically silenced by increased methylation of the CpG islands in the promoter region of the gene. This resulted in the loss of *BAMBI* mRNA and protein expression. In line with this observation, aberrant epigenetic regulation was recently proposed as one of the key hallmarks of cancer initiation and progression (254). Mutations in the proteins maintaining the epigenetic landscape such as the polycomb repressor EZH2, histone lysine demethylases and chromatin remodeling enzymes SWI/SNF are frequently observed in a wide a range of cancers (255-257). Additionally, pronounced alterations in the abundance of the metabolites that are used as substrates by DNA- and histone-modifying enzymes (α-ketoglutarate and acetyl-CoA) are frequently observed in different tumor types (258). Such changes disrupt the homeostatic balance of the chromatin modifications and decrease the chromatin "resistance" to change. This allows cancer cells to alterate gene regulatory programs to boost their proliferative, chemoresistant or invasive properties. Thus, epigenetic silencing of *BAMBI* apparently contributes to malignant development, tumor progression and invasion by promoting the activation of the TGFβ-dependent epithelial-to-mesenchymal transition (EMT) program (251, 252).

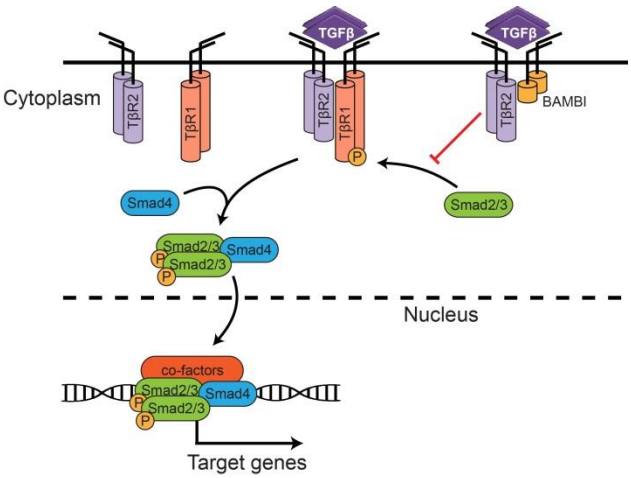

Figure 3.1 Inhibition of the TGFβ signal transduction by the negative pathway regulator BAMBI. Decoy receptor BAMBI lacks the intracellular kinase domain and forms an inactive complex with type II TGFβ receptor and prevents the downstream pathway activation.

3.1.2 BAMBI downregulation sensitizes NSCLC cells for TGFβ-induced invasion

The observed activation of the TGFβ signal transduction pathway in lung tumors with concomitant downregulation of the negative regulator BAMBI suggest that the loss of BAMBI sensitizes lung cancer cells to TGFβ and thereby promotes EMT-dependent malignant processes. A central role of TGFβ signal transduction in EMT regulation has already been observed in breast cancer (259) and esophageal cancer (260). For lung cancer it was shown that long term TGFβ treatment induces EMT transition in A549 and LC31 lung cancer cell lines (261). Furthermore, Prudkin et al. observed that the EMT phenotype is commonly expressed in primary squamous cell carcinoma and adenocarcinoma of the lung (153). The results of this study revealed that BAMBI-negative lung cancer tissue display a mixed EMT phenotype as indicated by the expression of the typical EMT markers: the retained expression of epithelial marker proteins (E-cadherin) along with the upregulation of the mesenchymal marker proteins (N-cadherin) and EMT-associated markers such as HMGA1 (262) and Osteopontin (SPP1) (263). This is in line with the observation that in some metastatic cancers partial EMT is observed (264) and is associated with a more aggressive phenotype (194). It has been proposed that EMT is a highly dynamic and reversible multi-step process. The mixed expression of both epithelial and mesenchymal markers within human lung tumor tissue suggests that in lung cancer EMT is only required for a limited time-frame to seed metastases. Alternatively, the EMT occurs primarily at the invading front of tumors and hence is only active at the time of invasive behavior. These possibilities is supported by the immunohistochemistry and immunofluorescence data wherein SPP1 and N-cadherin are observed at the invading front of tumor cells. The EMT program has been linked to chemotherapy resistance in ovarian carcinomas (265) and it was reported for the A549 lung cell line that chemoresistance in this cell line was associated with TGFβ-induced EMT (266). The presentedwork showed that the restoration of BAMBI expression in NSCLC cell lines reduced TGFβ induced phosphorylation of the R-Smads. As a consequence TGFβ-mediated expression of EMT markers was markedly attenuated and the induction of cell migration and invasion was significantly reduced. Furthermore, the results of the mouse lung colonization experiment that is the closest proxy for an *in vivo* metastasis strongly suggest a pivotal role of BAMBI in processes of metastasis and tumor growth. These observations identify BAMBI as a negative regulator of TGFβ-induced EMT responses in NSCLC.

The in-depth analysis of patient samples and mechanistic insights from *in vitro* studies presented in this report suggest that TGFβ pathway might be a promising therapeutic target in lung cancer. There are currently no completed clinical trials targeting the TGFβ pathway in lung cancer patients. However, in a

mouse model of breast cancer, radiotherapy-induced increase of the TGFβ serum levels favored cancer metastasis that was prevented by co-administration of TGFβ-targeting antibodies (267). In addition, the targeting of EGFR signaling by the EGFR antibody Cetuximab in a xenograft model of head and neck cancer resulted in emergence of resistant tumor cells that expressed relatively higher levels of TGFβ. The elevated levels of TGFβ in the tumor microenvironment enabled the tumor cells to evade antibody-dependent cell-mediated cytotoxicity and to resist the antitumor activity of Cetuximab *in vivo*. These results suggest that TGFβ is a possible molecular determinant of resistance of cancers to EGFR-targeted therapy (268).

A recent study identified MED12, a component of the transcriptional MEDIATOR complex that is mutated in cancers, as a determinant of response to ALK and EGFR inhibitors. Similar to BAMBI, MED12 negatively regulates TGFβ receptor through physical interaction and its suppression results in activation of TGFβ signaling, which is both necessary and sufficient for drug resistance. MED12 loss induces an EMT-like phenotype, which has been associated with chemotherapy resistance in colon cancer patients and with gefitinib-resistance in lung cancer (141).

The epigenetic silencing of BAMBI by promoter hypermethylation might comprise a promising target for epigenetic therapy to restore BAMBI expression in lung cancer tissue, and therefore desensitize cancer cells against TGFβ-mediated cancer cell invasion. The DNA demethylation agent 5-azacytidine (5-azaC) restored the expression of the miRNA miR-200 that controls the epithelial state of the cells and reverted the aggressive mesenchymal phenotype of lung cancer cells (269, 270). Similarly, inhibitors of the histone deacetylase SIRT1 halted the progression of leukemia by re-activating tumor-suppressor genes and programs of cellular differentiation (271, 272).

Taken together, this work reports overactivation of the TGFβ signal transduction pathway in lung cancer tissue and suggests that epigenetic silencing of the negative regulator BAMBI might be the major cause for it. Loss of BAMBI sensitizes lung cancer cells for TGFβ-dependent EMT and thereby promotes cancer spread and metastasis. Thus, therapeutic targeting of altered TGFβ signal transduction in lung cancer might offer new possibilities of limiting the metastatic potential and chemotherapy resistance of lung cancer.

3.2 Mechanisms underlying TGFβ-mediated pro-tumorigenic effects in squamous cell lung cancer

TGFβ-induced changes in signal transduction, gene expression and phenotypic responses in the LUSC cell line SK-MES1 were examined to uncover mechanisms promoting tumor progression in LUSC. The analysis identified the TGFβ-inducible non-muscle myosin MYO10 as essential for cancer cell invasion and showed that a high *MYO10* mRNA expression ratio is an independent biomarker for patients at risk for a more aggressive course of the disease.

3.2.1 TGFβ-induced cytoskeleton rearrangements govern invasive spread of LUSC cells

Previous reports regarding the importance of TGFβ signaling in LUSC progression are contradictory. It was shown that increased immunohistochemistry staining of the TGFβ1 ligand in 194 NSCLC tumors is an independent prognostic biomarker for poor patient prognosis (273). In another study, the expression of the TGFβ-induced EMT markers Twist and Slug was assessed in 137 resected stage I NSCLC tumors using tissue microarray and was prognostic for shorter overall and progression-free patient survival (161). In contrast, a recent study of Malkoski et al. examined the expression of the type II TGFβ receptor on protein and mRNA levels in 187 NSCLC tumors and reported that reduced TGFβRII immunostaining in LUSC patients is associated with a more aggressive tumor behavior and reduced patient survival (168). However, neither of the studies discriminated between LUAD and LUSC subtypes of lung cancer and such studies examine the correlations, but do not provide mechanistic insights into observed phenomena.

Therefore, in this work mechanistic phenotypic and transcriptome-wide studies of the TGFβ-stimulated LUSC cell line SK-MES1 were combined with the analysis of the paired tumor and non-tumor tissue from a clinical cohort comprising 362 NSCLC patients, including 151 LUSC cases. The exposure of the LUSC cell line SK-MES1 to TGFβ triggered changes in cell morphology that were accompanied by increased chemoresistance as well as an increase in migratory and invasive properties of the cells. These observations support a pro-metastatic role of TGFβ signaling in the context of LUSC.

There is growing evidence that aberrant upregulation of actin cytoskeleton proteins plays a central role in metastatic progression in different types of cancers (274, 275). Particularly, non-muscle myosins are implicated in tumor progression through their roles in cell migration and invasion (208). It was reported that TGFβ1 stimulation of the epithelial-like lung adenocarcinoma cell line H1437 triggered upregulation

of cytoskeletal proteins and induced a more aggressive cell phenotype (194). By integration of transcriptome and methylome data it was shown that an enrichment of actin cytoskeleton proteins correlated with poor survival of lung adenocarcinoma patients. Others observed that high expression of the actin-binding filopodial-crosslinking protein fascin was prognostic for an aggressive metastatic disease and for poor survival of patients with breast and esophageal squamous cell tumors (276, 277). Here, siRNA-mediated knockdowns of either *MYO10*, *MYH9* or *MYO1E* was sufficient to abrogate TGFβ-induced 3D collagen invasion of the LUSC cell line SK-MES1. These observations are in agreement with previous work demonstrating that shRNA knockdown of *MYO10* in the breast cancer cell line MDA-MB-231 inhibited Matrigel invasion and *in vivo* invasion in lung colonization and mammary fat pads assays (278). siRNA depletion of *MYH9* in the esophageal squamous cell line KYSE-510 impaired migratory and invasive abilities in gap closure and transwell assays, respectively (279). Dominant negative inhibition of MYO1E in RSV-transformed BHK-21 cells compromised the formation of invadosomes that are involved in matrix degradation and invasion (280).

Existing evidence suggests that the pro-metastatic role of MYO10 is mediated by its function in filopodia and invadopodia structures. Both structures represent actin-rich protrusions promoting invasive and migratory spread of cancer cells (281). MYO10 was reported to transport β-integrins to filopodia tips, facilitating their extension and contraction (278). Similarly, MYO10 expression was shown to be the essential for invadopodia formation. Silencing of MYO10, not only reduced the amount of filopodia, but also reduced the expression of MMP2, MMP9 and MMP14 proteases that are the major proteolytic enzymes recruited to invadopodia to degrade extracellular matrix (282). Previous works showed that MYO10 expression is controlled by early growth response-1 (EGR1) transcription factor in tumors with mutant p53 (278). However, an elevated MYO10 expression was also reported in breast tumors with wild-type p53 (282). In this study, TGFβ-dependent upregulation of MYO10 expression in LUSC cells is reported.

Therefore, it appears that the activation of the TGFβ signal transduction pathway in LUSC context enhances the invasive phenotype of the cells by up-regulating actin cytoskeleton proteins that are crucial for formation and function of the invadopodia and filopodia structures.

3.2.2 Novel biomarkers for LUSC patient survival and chemotherapy response

Analysis of a cohort of 362 lung cancer patients, including 151 LUSC patients, revealed that the *MYO10* mRNA expression ratio between tumor and adjacent tumor-free tissues is an independent prognostic factor that is associated with a poor overall survival in patients with resected LUSC.

Expression of several other myosin motor proteins was previously reported to be prognostic for overall survival in patients with several cancer types. MYH9 expression examined by immunohistochemistry was an independent prognostic factor for overall survival in patients with resected NSCLC (279), esophagus and bladder cancers (207, 283). Investigation of gene expression signatures in basal-like breast tumors showed a correlation between *MYO1E* mRNA expression level and poor prognosis (206). However, to date there are no studies linking *MYO10* expression to patient survival. Yet, the results of this study show that *MYO10* mRNA expression ratio in tumor versus tumor-free tissue might represent a new promising prognostic factor for survival of LUSC patients, especially considering the fact that *MYO10* was upregulated at the mRNA level in almost 30% of LUSC patients in the TCGA dataset, which appears to be the highest rate of *MYO10* upregulation among all the cancer entities reported in TCGA. Furthermore, LUSC patients with high *MYO10* mRNA expression ratio and pre-existing lymph node metastases have significantly poorer overall survival (**Figure 2.14C**) alongside with increased chemotherapy resistance (**Figure 2.13A**). Similar observations that tumor cells with increased metastatic potential are more resistant to chemotherapy treatment were previously made across several cancer types, including lung and breast cancers (284-286). This was attributed to decreased proliferation rate and upregulation of resistance-related genes in cells undergoing EMT (140). Therefore, the *MYO10* mRNA expression ratio could be used to discriminate between LUSC patients that will benefit from platinum-based adjuvant chemotherapy from those that should rather be directly treated with immunotherapy as a new emerging treatment approach in LUSC (15). Finally, as it appears that a large fraction of LUSC tumors rely on TGFβ signals to promote their tumorigenesis, this suggests that in addition to *MYO10*, several other metastasis- and resistance-related TGFβ-inducible genes that were identified in this time-resolved transcriptome-wide study, including the non-muscle myosins *MYO1E* and *MYH9*, might comprise a promising robust prognostic gene signature for patients with resected LUSC.

Concluding, this study demonstrates that activation of the TGFβ signal transduction pathway in LUSC context promotes tumor invasiveness and chemoresistance. The non-muscle myosin MYO10 was identified as a TGFβ target gene that mediates TGFβ-induced cancer cell invasion. The study shows that the *MYO10* mRNA expression ratio in tumor versus tumor-free tissue can be used as an independent

prognostic factor for survival of patients with resected lung squamous cell carcinoma and propose that MYO10 may represent a new molecular target for therapeutic intervention. Importantly, the presented study also suggests that therapeutic targeting of the invadopodia- and filopodia-specific myosin motors, including MYO10, MYO1E and MYH9 might limit TGFβ-mediated cancer spread without causing adverse side effects in normal tissue.

3.3 Dynamic features of TGFβ signal transduction in LUAD cell lines

Having previously established that TGFβ signal transduction pathway is over-activated in the lung tumors in comparison to adjacent tumor-free lung tissue due to the loss of the negative pathway regulator BAMBI (**sections 2.1 and 3.1**), and demonstrated that TGFβ pathway activation exerts pro-tumorigenic effects in the context of LUSC by promoting cancer cell invasion and chemoresistance (**sections 2.2 and 3.2**), I aimed to understand the dynamic behavior and regulation of the TGFβ-induced Smad2/3 phosphorylation in lung cancer cell lines by combining quantitative experiments and mathematical modeling to identify new potential intervention strategies.

3.3.1 Abundance of TGFβ/Smad signaling pathway components in LUAD cell lines

Traditionally, dynamic processes such as signal transduction have been investigated in a qualitative way, while quantitative information including the abundance of pathway components has rarely been recorded. However, the concentrations of the key components of signal transduction networks are crucial parameters that determine the network wiring, its dynamic behavior and induced cellular responses (226, 287). Therefore, information on cell type-specific abundance of the key pathway components is essential for establishing the mathematical model based on ordinary differential equations that aim to elucidate the mechanisms underlying differential dynamic behavior of the pathway in the examined LUAD cell lines.

In the presented work, pronounced differences in the absolute abundance of TGFβ pathway components Smad2, Smad3 and Smad4 between LUAD cell lines H1975, H838 and H1650 were revealed using quantitative immunoblotting combined with dilution series of recombinant calibrators. The absolute concentrations of Smad proteins were previously examined in several other cell lines. Similarly to H838 and H1650 cells, Smad2 was found in a greater excess than Smad3 in human hepatocellular carcinoma cell line HepG2 (10:1 ratio), gastric carcinoma cell line SNU-16 (8:1 ratio) as well as in non-cancer cells such as mink lung epithelial cells (100,000 versus 15,000) and mouse hepatocytes (80,000 versus 5,000) (181, 288-290). However in H1975 cells, Smad2 and Smad3 proteins were equally expressed that was also observed in human HaCaT keratinocyte cell line and human SNU-620 gastric carcinoma cell line (288). Such differential abundance of the Smad molecules in the examined LUAD cell lines should have profound differences on TGFβ-induced gene expression, since Smad2 and Smad3 proteins interact with distinct set of transcriptional co-factors and therefore supposedly control different transcriptional responses (291). In line with it, increase in relative Smad3 to Smad2 ratio in

HaCaT human keratinocytes using siRNA knockdown enhanced TGFβ-mediated cytostatic responses by causing higher induction of cell cycle inhibitors $p15^{INK4B}$ and $p21^{CIP1}$ and greater reduction of cMyc expression (288). Therefore, the presented data suggest that the abundance of key TGFβ/Smad pathway species might critically influence the dynamic behavior of TGFβ signaling pathway in LUAD cell lines. Furthermore, observed differences in Smad abundance in the examined LUAD cell lines might in part explain differential induction of the target genes that was experimentally observed (**section 2.3.8.1**).

3.3.2 Dynamics and regulation of the TGFβ/Smad signal transduction in LUAD cell lines

To generate time-resolved quantitative data for model calibration, the time frame and the optimal stimulation dose for the respective measurements has to be defined. In the presented work the dose of 1 ng/ml TGFβ induced the maximal amplitude of pathway activation after acute TGFβ stimulation for 60 minutes. The chosen dose is within the range of the TGFβ concentrations commonly used in the literature. For instance, Goumans et al. (292), who studied pro- and anti-angiogenic properties of TGFβ, showed that 0.5 ng/ml TGFβ is sufficient to yield a maximal response of Smad2 phosphorylation after 1 hour TGFβ treatment in mouse endothelial and fibroblast cell lines, while Frick et al. demonstrated that 2 ng/ml TGFβ results in the highest fold change of Smad3 nuclear translocation in the mouse myoblast cell line C2C12 (293). Additionally, a dose of 1 ng/ml TGFβ1 is in the range of physiologically relevant concentrations reported in the plasma of LUAD patients assessed by ELISA (154, 294-297).

Time-resolved experiments demonstrated a transient dynamic behavior of TGFβ-induced Smad2/3 phosphorylation in all studied LUAD cell lines when stimulated with a saturating dose of 1 ng/ml TGFβ. The maximal pathway activation was observed after 60–90 minutes of stimulation followed by a signal decline afterwards. Similar transient pathway dynamics was previously reported in multiple cell lines, including lung adenocarcinoma cell line A549, human HaCaT keratinocyte cell line and mouse C2C12 immortalized myoblast cell line when Smad2/3 phosphorylation was assessed by immunoblotting (185, 187, 298, 299). Likewise, studies that utilized genetically-encoded fluorescence Smad reporters that translocate into the nucleus in response to stimulation with TGFβ, also reported transient Smad2/3 phosphorylation dynamics on a single cell level (300, 301). Several mechanisms were proposed to explain such signal attenuation. One of the most prominent ones include transcriptional negative feedback loop mediated by inhibitory Smad7 and Smurf1/2 E3 ubiquitin ligases that result in the degradation of the activated TβR1 (50, 51), and constitutively active mechanisms mediating receptor and Smad2/3 dephosphorylation (64, 211). However, the importance and cell type specificity of these feedbacks is controversially discussed in the literature (185, 186, 302).

In this work, the effect of several molecular inhibitors on TGFβ-induced Smad phosphorylation dynamics were comprehensively compared in three distinct LUAD cell lines to examine the nature of the negative feedbacks that are responsible for signal attenuation. Obtained quantitative data was used to calibrate the mathematical model that suggested the existence of constant ligand-independent receptor turnover: the receptor protein with relatively short half-life constantly produced from stable mRNA and degraded in a proteasome-dependent manner independently of gene transcription. As a consequence, inhibition of protein translation using cycloheximide, not only inhibited TGFβ-induced transcriptional negative feedbacks, but also reduced the receptor abundance. Therefore, transient pathway activation with lower maximal amplitude was observed. Similarly, transient TGFβ-induced Smad dynamics in response to cycloheximide treatment was reported in several studies performed in HaCaT and NIH3T3 cells (183, 185, 303). However, in these works the authors used separate immunoblot membranes to detect TGFβ-induced Smad phosphorylation dynamics in cycloheximide-treated and control untreated cells. Therefore, reduced amplitude of pathway activation upon cycloheximide treatment was not observed in those cases. In contrast to cycloheximide treatment, the inhibition of mRNA transcription using actinomycin D only suppressed transcriptional negative feedback loops without affecting TGFβ receptor abundance due to the high stability of the receptor mRNA as predicted by the developed mathematical model. As a result, actinomycin D treatment resulted in a switch from transient to sustained Smad dynamics in the examined LUAD cell lines. This observation is in an agreement with the study of Wang et al., who reported that the use of actinomycin D in MDA-MB-231 breast cancer cell line abrogated TGFβ pathway attenuation, highlighting the importance of transcriptional negative feedback loops (304). Predicted high stability of the receptor mRNA is line with the recent results of the genome-wide analysis of mRNA stability performed in HeLa cells that estimated the half-life of *TGFBR1* mRNA as 8.13 hours, which was among the 25% most stable mRNAs (305). Here, the model prediction was further experimentally validated by measuring the mRNA half-life of *TGFBR1* and *TGFBR2* mRNAs in actinomycin D-treated LUAD cell lines.

The model-based analysis suggested that the TGFβ receptor is constantly targeted for proteasome-dependent degradation. Therefore, treatment with proteasome inhibitors such as MG-132 would lead to the accumulation of the receptor protein resulting in higher amplitude of pathway activation upon stimulation with TGFβ. Several studies previously reported enhanced TGFβ pathway activation in presence of MG-132. For instance, co-treatment of HaCaT cells with TGFβ and proteasome inhibitor MG-132 resulted in sustained pathway activation when Smad2/3 phosphorylation was assessed by quantitative immunoblotting (185), or sustained overactivation when nuclear Smad4 accumulation was

assessed by quantitative time-lapse microscopy (301). Likewise, Zieba et al. demonstrated using *in situ* proximity ligation assay that co-treatment of mouse embryonic fibroblasts with 10 ng/ml TGFβ and MG-132 inhibitor for 45 min increased the abundance of nuclear-localized Smad2/3-Smad4 complexes in comparison with TGFβ stimulation alone (306). However, all these observations were mostly attributed to the inhibition of the proteasome-dependent negative feedbacks by MG-132. Here, using targeted mass-spectrometry approach in combination with absolute quantification based on the heavy-labeled internal standards, the increase of the TGFβ receptor abundance after MG-132 pre-treatment was validated according to the model prediction.

To date, extensive experimental evidence is accumulated regarding multiple potential mechanisms that play role in a negative regulation of the TGFβ signaling pathway (37, 50, 62-64, 66, 211, 215, 307-309). However, combined synergistic effects of different feedbacks are poorly understood. In this work, a comprehensive mathematical model of the TGFβ signaling pathway was developed that includes multiple negative feedback loops that act at the same time: (i) transcriptional proteasome-dependent (mediated by I-Smads and Smurfs); (ii) transcriptional proteasome-independent (mediated by BAMBI and PMEPA1); (iii) and constitutively active transcription-independent (pre-existing phosphatases such as PPM1A and GADD34-PP1c). The prevalence of such negative feedbacks is highly cell type-specific, which was reflected in the differential response of the examined LUAD cell lines to MG-132, cycloheximide and actinomycin D inhibitors. This explained the long-standing controversies regarding mechanisms that are responsible for the attenuation of the TGFβ signaling pathway. For instance, on the one hand TGFβ stimulation of cycloheximide-treated C2C12 cells resulted in sustained nuclear accumulation of Smad4 (301), while on the other hand cycloheximide treatment did not prevent pSmad2 signal attenuation in HaCaT cells (185). Likewise, inhibition of the proteasome-mediated protein degradation showed either no effect (66, 185, 310), or resulted in a switch from transient to sustained Smad signaling (211, 215, 216, 301). Similarly, several studies reported significant reduction of the TβR1, TβR2 and Smad2/3 levels upon stimulation with TGFβ (50, 53, 185), while others did not observe such effect (184, 310). These seemingly contradictory reports are both consistent with the developed mathematical model of the pathway and could be explained by differential abundance and non-linear interplay of the negative regulators as well as different rates of the receptor turnover.

In conclusion, the established mathematical model that was calibrated on extensive quantitative data of the TGFβ-induced Smad2/3 phosphorylation measured in three distinct NSCLC cell lines revealed differential mechanisms that mediate cell type-specific dynamic behavior of the TGFβ-induced Smad2/3

phosphorylation. This approach revealed a different prevalence of negative feedbacks that induce the degradation of the TGFβ receptor or reduce its ability to phosphorylate Smads in the examined NSCLC cell lines. The model-based analysis predicted that the TGFβ receptor protein undergoes constant turnover: the unstable receptor protein is constantly degraded and produced again from the stable receptor mRNA. High stability of the TGFβ receptor mRNA was confirmed by mRNA half-life analysis, while the accumulation of the TGFβ receptor protein upon inhibition of the proteasome function was validated using targeted quantitative mass spectrometry. These findings highlighted that the TGFβ receptor is one of the most sensitive nodes that controls pathway activation.

3.4 Conclusions and perspectives

Understanding the impact of the Transforming growth factor beta (TGFβ) signaling on lung cancer progression is essential for designing novel therapeutic approaches. Therefore, the presented study was focused on unraveling the mechanisms contributing to altered TGFβ signaling in lung cancer context and uncovering the mechanisms mediating pro-tumorigenic impact of the TGFβ signal transduction. Finally, the mathematical model combined with iterative quantitative experiments was used to infer the regulatory mechanisms controlling the dynamic behavior of TGFβ-induced Smad2/3 phosphorylation.

In the first part of this work, the activation status of the TGFβ signal transduction was examined at the protein and mRNA level in tumor tissue of lung cancer patients. This analysis revealed that the components of the TGFβ pathway were substantially activated in human lung cancer tissue with concomitant epigenetic silencing of a negative regulator of the TGFβ pathway, the decoy pseudoreceptor BAMBI. Reconstitution of BAMBI in NSCLC cells decreased TGFβ-induced Smad2/3 phosphorylation and TGFβ-induced *in vitro* cell migration and invasion. Furthermore, BAMBI reconstitution reduced the *in vivo* metastatic potential of NSCLC cell lines as assessed by a mouse lung colonization assay. These results demonstrated that the loss of the negative regulator BAMBI promotes the activation of the TGFβ pathway as well as TGFβ-driven invasiveness of lung tumors.

In the second part of the work, molecular components contributing to TGFβ-induced lung cancer progression remain were investigated in the context of squamous cell carcinoma of the lung (LUSC). The dynamics of gene expression in TGFβ-treated LUSC cells was assessed by next-generation mRNA sequencing. The examinations revealed up-regulation of motility- and actin cytoskeleton-related genes including the non-muscle myosin 10 (MYO10). Knockdown of MYO10 abrogated TGFβ-induced collagen gel invasion of LUSC cells. Examination of mRNA expression in paired surgically resected tissues of LUSC patients showed that the mRNA expression ratio of *MYO10* in tumor and tumor-free tissue is prognostic for patient overall survival and facilitates the prediction of the response of these patients to adjuvant chemotherapy. This work provided novel insights into key molecular mechanisms contributing to LUSC progression by identifying non-muscle myosins as important downstream mediators of TGFβ-mediated cancer cell invasion.

Lastly, the mechanisms controlling the dynamic properties of the deregulated TGFβ signal transduction pathway were examined in the context of lung cancer. The analysis of TGFβ-induced signal transduction in three LUAD cell lines showed a distinct dynamic behavior of the TGFβ-induced Smad2/3

phosphorylation and a differential impact of inhibitor perturbations. These results suggested a different prevalence of negative feedbacks that induce the degradation of the TGFβ receptor or reduce its ability to phosphorylate Smads in the examined cell lines. The model-based analysis predicted that the TGFβ receptor protein undergoes constant turnover: the unstable receptor protein is constantly degraded and produced again from the stable receptor mRNA. High stability of the TGFβ receptor mRNA was confirmed by mRNA half-life analysis, while the accumulation of the TGFβ receptor protein upon inhibition of the proteasome function was validated using targeted quantitative mass spectrometry. These findings highlighted that the TGFβ receptor is one of the most sensitive nodes that controls pathway activation. Therefore, targeting processes that control receptor abundance rather than using conventional TGFβ receptor kinase inhibitors could be a promising therapeutic approach.

The results of this work could be used for interpreting the complex dynamic behavior of TGFβ-induced Smad2/3 phosphorylation that was previously observed in different cellular model systems as well as for rational design of novel intervention strategies targeting TGFβ signal transduction pathway. The developed mathematical model represents a central building block that can be further extended by incorporating TGFβ-induced non-Smad signaling pathways such as MAPK/Erk and PI3K/Akt axes. These both signaling pathways are essential in mediating tumorigenic properties of cancer cells (311, 312). Therefore, the mathematical model that enables to quantitatively examine the cross-talks between these essential pro-tumorigenic signal transduction pathways would provide invaluable insights into molecular networks that mediate cancer progression and therapy resistance.

To conclude, the presented work provides insights into molecular alterations that cause TGFβ pathway deregulation, suggests new potential biomarkers and showcases the potential of the mathematical modeling approach combined with quantitative experiments to uncover general principles of cell type-specific regulation of TGFβ-induced Smad2/3 phosphorylation in lung cancer cell lines.

4 Materials and methods

Unless stated otherwise, reagents were acquired from Sigma-Aldrich.

4.1 Cell biology

4.1.1 Cultivation of human cancer cell lines

Human lung cancer adenocarcinoma cell lines A549, H1975, H838, H1650 and human lung squamous cell carcinoma cell line SK-MES1 were purchased from ATCC. All cell lines were authenticated with Multiplex human Cell line Authentication Test (Multiplexion) (313). Cells were grown in culture medium: DMEM (Lonza) supplemented with 10% FCS (Gibco), 100 U/ml penicillin and 100 µg/ml streptomycin (Gibco). For stimulation, growth factor-depleted medium was used: DMEM without Phenol red (Lonza) supplemented with 1 mg/ml BSA (Sigma), 100 U/ml penicillin, 100 µg/ml streptomycin and 2 mM L-glutamine. Cells were kept in 5% CO_2 at 37°C and 95% relative humidity. Cells were passaged to a maximum of 25 passages and regularly controlled for mycoplasma contamination (Multiplexion).

4.1.2 Isolation of primary alveolar epithelial type II cells

Tumor-free lung tissues from surgical specimens of patients who underwent pneumectomy or lobectomy at the LungenClinic Grosshansdorf were used for isolation of primary alveolar epithelial type II cells (AECII). Fresh tissues were rinsed with sterile PBS to remove excess blood and stored in RPMI 1640 cell culture medium (Life Technologies) supplemented with 10% FCS and 1% penicillin/streptomycin. To extract AECII, the tissue was manually dissected with surgical razors and rinsed with AECII buffer (1.9 mM $CaCl_2$; 1.3 mM $MgSO_4$; 136 mM NaCl; 6.1 mM KCl; 3.2 mM Na_2HPO_4; 6.1 mM glucose and 9.9 mM HEPES) over a sieve to remove residual blood. Tissue pieces were dissociated by incubation for 60 min at 37°C and 5% CO_2 in AECII buffer supplemented with 2 mg/ml Dispase II (Roche Applied Sciences) under constant stirring. The lung tissue pieces were further filtered through nylon gaze of decreasing pore size (100-µm, 50-µm, 20-µm) and finally centrifuged for 15 min at 478 *g* at room temperature. The resulting cell pellet was resuspended in 50 ml of AECII buffer supplemented with 0.001% Accutase (MilliPore) (v/v) and 20 µg/ml DNAse I (Roche Applied Sciences). Each 10 ml of this suspension was applied onto 10 ml Biocoll gradient solution (Biochrome,) and centrifuged for 25 min at 478 *g* and room temperature. The resulting interphase was washed with AECII buffer at 478 *g* for 15 min at 4°C and finally resuspended in cell culture medium. Each 5×10^7 cells were seeded on 6-cm petri dishes and incubated for 20 min at 37°C in an incubator to allow adherence of

immune cells. 1×10^7 cells were resuspended in 80 µl MACS-buffer (PBS pH 7.2 with 0.5% BSA and 2 mM EDTA), mixed with 20 µl anti-CD45 conjugated para-magnetic beads (Miltenyi) and finally incubated on a rotating device for 15 min. Depletion of CD45 positive immune cells with LD columns (Miltenyi) was conducted according to manufacturer´s instructions. AECII isolation procedure was performed by Sebastian Marwitz (Research Center Borstel).

4.1.3 Retroviral transduction

Human BAMBI-GFP insert was obtained from the plasmid pCMV6-AC-GFP (RG200195, OriGene) using BamHI/Pme I restriction sites. The insert was cloned into the retroviral expression vector with a Tet-inducible promoter pMOWSIN-TREt (314). As control, pMOWSIN-TREt-GFP was used. Both pMOWSIN-TREt-BAMBI-GFP and pMOWSIN-TREt-GFP were used in combination with pMOWS-rtTAM2 encoding the cDNA for transactivator protein (315). Transfection of the Phoenix ampho packaging cell line was performed by calcium phosphate precipitation. Virus-containing supernatants were generated 24 h after transfection by passing through a 0.45-µm filter, supplemented with 8 µg/ml polybrene and applied in the proportion 1:3.5 (pMOWS-rtTAM2 : pMOWSIN-TREt-BAMBI-GFP or pMOWSIN-TREt-GFP) for spin infection of 1.5×10^5 A549 and H1975 cells seeded in 6-well plates. Stably transduced A549 and H1975 cells expressing GFP-tagged human BAMBI or GFP alone were selected in the presence of 1 µg/ml puromycin 48 h after transduction. Cloning was performed by Susen Lattermann (DKFZ, Heidelberg). Retroviral transduction was performed by Sofia Depner (DKFZ, Heidelberg).

4.1.4 siRNA transfection

A pool of four targeting siRNAs (5 nM; SMARTpool, Dharmacon) was in-solution transfected during cell seeding using Lipofectamine RNAiMAX (ThermoFisher Scientific, #13778150) according to the manufacturer's instructions. Approximately 5×10^5 or 15×10^3 cells were used per 6-cm dish or one well in 96-well plate respectively. A pool of four non-targeting siRNA was used as a negative control (5 nM, Dharmacon, #D-001810-10-20). Experiments were started 36 hours after transfection.

4.1.5 Cell viability assay and caspase activity assays

10×10^3 of SK-MES1 cells were seeded per well in 96-well plates, allowed to attach overnight and then stimulated for 3 days with 2 ng/ml TGFβ1 in growth factor-depleted medium or left untreated. Subsequently, the medium was replaced with culture DMEM, either with or without TGFβ and additionally supplemented with different concentrations of cisplatin (Teva). CellTiter-Blue Viability

(Promega) and Apo-ONE Homogeneous Caspase-3/7 (Promega) assays were used to measure the viability of cells and caspase 3/7 activity respectively. The resulting fluorescence was measured using an infinite F200 pro Reader (Tecan).

4.2 Protein biochemistry

4.2.1 Cell lysis

If not stated otherwise, cells were lysed in 500 µl of whole-cell lysis buffer (1% NP40, 150 mM NaCl, 50 mM Tris HCl pH 7.4, 2.5 mM NaF, 1 mM EDTA, 0.5 mM Na_3VO_4, 1 mg/ml deoxycholic acid, 2 µg/ml aprotinin and 200 µg/ml AEBSF). Lysates were kept on ice for 10 min, sonicated for 25 sec (Bandelin Sonopuls, 75% amplitude, 0.1 sec pulse "on", 0.5 sec pulse "off") and centrifuged for 10 min at 21,000 *g* at 4°C. Supernatants were transferred to new tubes.

4.2.2 Immunoprecipitation and quantitative immunoblotting

The cell lysates were either directly used as a total cell lysate (TCL) or subjected to immunoprecipitation (IP).

Protein concentration of the lysates was determined by BCA assay (Pierce, #23225). For IP 500–800 µg of protein lysate was mixed with 3.5 µl of antibodies against Smad2/3 (BD Biosciences, #610842) and 25 µl 50% Protein A sepharose slurry (GE Healthcare, #17-0963-03) in a final volume of 400–450 µl. The resulting mixture was rotated at 4°C overnight. After overnight rotation, samples were washed twice with whole-cell lysis buffer and once with TNE buffer (10 mM Tris, 100 mM NaCl, 1 mM EDTA and 100 µM Na_3VO_4). After washing, 35 µl of 2× SDS sample buffer (4% SDS, 50 mM Tris pH 7.4, 10% glycerol, 10% β-mercaptoethanol, 100 mM DTT, 0.01% bromphenol blue) was added per IP sample. For TCL samples, 15–25 µg of protein lysates were mixed with equal volumes of 2× SDS sample buffer. Samples were incubated at 95°C for 3 min, separated by 10% SDS-PAGE and transferred to nitrocellulose membranes (Amersham, #1060001). The membrane was blocked for 1 h with 33% (v/v) Odyssey blocking buffer (LI-COR, #927-40010) in PBS and subsequently incubated with the respective primary antibodies at 4°C overnight (**Table 4.1**). Afterwards, secondary antibodies coupled to IRDye infrared dyes (LI-COR, #926-32211 and #926-68070, 1:15,000) were used for detection with an infrared Odyssey imager (LI-COR). Both primary and secondary antibodies were diluted in 33% (v/v) Odyssey blocking

buffer (LI-COR, #927-40010) in 0.02% TBS-Tween 20. Signal quantification was performed using ImageQuant TL software (GE Healthcare). Independent replicates were scaled and averaged using an R script (210).

Target	Species	Dilution	Company	Catalog number
total Smad2/3	mouse	1:2,500	BD Biosciences	#610842
pSmad3	rabbit	1:2,500	Cell Signaling	#9520
SnoN	rabbit	1:1000	Santa Cruz	#sc-9141
Smad4	mouse	1:1000	Santa Cruz	#sc-7966
β-actin	mouse	1:10,000	Sigma-Aldrich	#A5441
GFP	mouse	1:1000	Roche	#11814460001
BAMBI	rabbit	1:1000	Sigma	#HPA010866

Table 4.1. Primary antibody used in this work.

4.2.3 Determination of absolute numbers of molecules per cell

8.3×10^5 of H1975 cells, 1.3×10^6 of H838 cells or 7.7×10^5 of H1650 cells were plated per well in 6-well plates three days prior to experiment. Cells were growth factor depleted for 3 h and lysed in whole-cell lysis buffer. The entire volume of cell lysate was taken for Smad2/3 immunoprecipitation. A dilution series of recombinant streptavidine-binding peptide (SBP)- or glutathione S-transferase (GST)-tagged calibrators was spiked into the lysates. Additionally, cells of each cell line were trypsinized and counted in duplicates to relate measured absolute amount of proteins of interest to number of cells used per immunoprecipitation.

Quantitative immunoblot data of number of molecules per cell were processed using an R script kindly provided by Lars Velten (DKFZ, Heidelberg). The script allows calculating the amount of endogenous proteins and respective nM concentration based on a regression function, accounting for the molecular weight of the recombinant and the endogenous proteins. It also takes into the account the errors derived from calibration curve, cell volume, number of lysed cells, as well as estimates the relative contribution of error sources.

To determine the cell volume of LUAD cell lines, cells stably expressing green fluorescent protein (GFP) were additionally stained with Hoechst 39522 to visualize the nuclear compartment. Subsequently, z-stacks of multiple cells were acquired by confocal microscopy. 3D image reconstruction was performed using Imaris software (Bitplane). Whole-cell and nuclear volumes were segmented using the surface

function based on GFP and Hoechst signals, respectively. This information allowed for the conversion of protein amounts from molecules per cell to absolute concentrations.

4.2.4 Mass spectrometry

4.2.4.1 Shotgun proteomics

2.1.×10^6 of H838 cells were seeded on 10-cm dishes 3 days prior the experiment, growth factor depleted for 3 h, stimulated with 1 ng/ml TGFβ and lysed at the indicated time points in 700 µl of whole-cell lysis buffer. The entire lysate was used for IP against total Smad2/3. Two IPs per each time point were performed and pooled during the IP washing step to obtain sufficient protein amount for mass spectrometric detection. Samples were separated for 1 h 35 mA/gel on 10% SDS-PAGE gel, stained with SimpleBlue SafeStain solution (Invitrogen) for 1 h at room temperature and destained overnight in dd$H_2$0.

Bands with expected Smad2/3 molecular weight were cut out of the gel and in-gel digestion was performed (316). Briefly, gel pieces were destained with buffer containing 30% acetonitrile in 100 mM NH_4HCO_3, reduced using 10 mM DTT for 30 minutes at 37°C and alkylated using 15 mM iodacetamide for 30 minutes in the dark followed and digested overnight with LysC (Promega) (1:100 dilution protein : enzyme ratio) at 37°C. Peptides were extracted by repeated addition of acetonitrile. The peptides were dried using a SpeedVac (Thermo Scientific), reconstituted in buffer containing 2% ACN (v/v) and 0.2% formic acid (v/v) and desalted using self-made stage-tips containing C18 material as described previously (316). The desalted peptide mix was reconstituted in buffer containing 20 mM citrate to enhance recovery of phosphopeptides.

Samples were measured using EASY-nLC 1000 (Thermo Scientific) coupled to a Q Exactive Plus Hybrid Quadrupole-Orbitrap mass spectrometer (Thermo Scientific). Peptides were separated on a 40-cm-long C18 column using one-hour 0–35% acetonitrile gradient. Survey MS scan (400–1600 m/z) was performed with a resolution of 70,000 m/z followed by MS/MS fragmentation top20 method with a resolution of 17,500 m/z. The obtained raw files were manually analyzed with Xcalibur software (Thermo Scientific) to quantify spectra corresponding to +2 and +3 charge states and three isotopic peaks of phosphorylated and unphosphorylated Smad2 C-terminal peptides. In-gel digestion, sample injection and quantification of Smad2 degree of phosphorylation in Xcalibur software was performed by Martin Böhm (DKFZ, Heidelberg).

4.2.4.2 Targeted proteomics

All samples for targeted mass spectrometry were prepared using an in-solution digestion protocol. For all steps low-binding reaction tubes (Nerbe Plus) and pipet tips (Nerbe Plus) were used. Cells were lysed in 200 µl lysis buffer (150 mM NaCl, 20 mM Tris pH 7.4, 10 mM NaF, 1 mM EDTA pH 8.0, 1 mM $ZnCl_2$ pH 4.0, 1 mM $MgCl_2$, 1 mM Na_3VO_4, 10% Glycerol and freshly added 0.1% Rapigest, 2 µg/ml aprotinin and 200 µg/ml AEBSF) by scraping, incubated on ice for 10 minutes, centrifuged (4°C, 15,000 *g*, 15 min) and the supernatant transferred to a new tube. The entire lysate was used for immunoprecipiration against TGFβR1. 25 µl of 50% protein G sepharose slurry (PGS, GE Healthcare), 5 µl of anti-TGFβR1 antibodies (Santa Cruz, #sc-398-G) and 2.5 ng of ^{15}N-labeled TGFβR1 calibrator comprising the intracellular domain of the type I TGFβ receptor were spiked-in per sample. After overnight rotation at 4°C, IPs were washed three times with TNE buffer (10 mM Tris, 100 mM NaCl, 1 mM EDTA and 100 µM Na_3VO_4). On-beads digestion was performed. Briefly, 100 µl of 4 M urea was added per sample. Afterwards, samples were reduced in 10 mM β-mercaptoethanol for 30 minutes at 37°C, alkylated in 20 mM chloracetamid (CAA) for 30 minutes at room temperature in the dark and quenched in 15 mM β-mercaptoethanol at 37°C for 30 minutes. Samples were digested with LysC (Promega) in an enzyme:protein ratio (w:w) of 1:50 at 37°C for 4 h, then diluted to 1 M urea using 3 volumes of 250 mM NH_4HCO_3 and digested with trypsin (Promega) in a 1:100 ratio at 37°C for 10 h. Enzymes were inactivated and Rapigest was precipitated by adding formic acid to pH 3.0, followed by incubation at 38°C for 30 min and centrifugation (17,000 *g*, 5 min, room temperature). The supernatant was transferred to a new tube and desalted using self-made stage-tips containing C18 material (241). Before mass spectrometric measurement peptides were reconstituted by adding 15 µl loading buffer (2% ACN, 0.1% FA), 5 minutes water bath sonication (Bandelin Sonorex) and 10 minutes shaking (Eppendorf). Samples were measured using EASY-nLC 1000 (Thermo Scientific) coupled to Q Exactive Plus Hybrid Quadrupole-Orbitrap mass spectrometer (Thermo Scientific). Peptides were separated on a 50-cm long C18 column using two-hour 0–35% acetonitril gradient.

All targeted parallel reaction monitoring (PRM) measurements were run in a Full MS–DIA (data-independent acquisition) mode to allow an alternation of full MS and PRM measurements. The number of scheduled peptides determined the loop count after how many PRM measurements a full MS was taken. For MS1 (full MS) resolution was set to 17,500 m/z, maximal ion collection time to 100 ms, maximal ion count to 3,000,000. For MS2 (PRM) optimized collision energy settings were used (19, 20, 21 NCE). Resolution was set to 35,000 m/z, maximal ion count to 200,000. Maximal ion collection time

depended on the number of peptides scheduled in parallel and was determined with the following equation:

$$\text{ion time} = \frac{\text{chromatographic peak width [s]}}{10 \times \text{ number of peptides}}$$

This measurement settings ensured that each eluting peptide of interest was measured at least 10 times over the course of its chromatographic peak. Chromatographic peak length was estimated as 30 s.

Data analysis was performed using Skyline (20147306). Peptide settings: 7–32 amino acid peptides from tryptic digestion with maximum of one missed cleavage site. Allowed structural modifications were "Carbamidomethylation (Cysteine)" and "Oxidation (Methionine)". Isotope label type was set to "heavy", isotope modification to "label: 15N". Peptides were matched to human proteome by SwissProt database. Transition settings: allowed precursor charges were 2, 3, 4; ion charges 1 or 2, ion type y, b and m/z range from 400 to 1600. Mass accuracy of MS1 and MS/MS filtering was both set to 10 ppm.

4.2.5 Bead-based immunoassay

5.5×10^5 of H1975 cells, or 7×10^5 of H838 cells, or 9×10^5 of H1650 cells were seeded in 6-cm dishes 2 days before the experiment, growth factor depleted for 3 h and stimulated with 1 ng/ml TGFβ1 (R&D Systems, #240-B-010). For time point "0 h" 1 ng/ml TGFβ1 was added to the 6-cm dish without cells. Medium was collected at indicated time points, centrifuged for 2 min at 13,000 *g* at 4°C to clear from cell debris. Supernatant was stored either overnight at 4°C in case experiment was performed the following day, or at -80°C until further usage.

TGFβ1 in supernatant was analyzed using the Bio-Plex Pro TGFβ kit (BioRad) according to the manufacturer's instructions. Briefly, samples were activated by adding 1 volume of 1 N HCl to 5 volumes of sample and incubated for 10 min at room temperature. Next, samples were neutralized by adding 1.2 N NaOH/0.5 M HEPES equal to the volume of HCl used. 50 µl of undiluted cell culture supernatant was used per sample. An eight-point standard dilution curve was prepared by serial two-fold dilution of growth factor-depleted DMEM containing 4 ng/ml TGFβ from the same aliquot that was used for cell stimulation. Data acquisition was performed with BioPlex 200 System (BioRad) and data analysis with BioPlex Manager (BioRad).

4.3 mRNA analysis

4.3.1 RNA extraction and cDNA synthesis

Frozen tumor cryosections were homogenized with the TissueLyser mixer-mill disruptor (2× 2 min, 25 Hz, Qiagen). Matched normal lung tissue pieces were homogenized using a Miccra D-8 rotor-stator homogenizer with DS-5/K1 (2× 30 sec, 20,000 *g*, Art-moderne Labortechnik). Total RNA was isolated from homogenized tissues or from cultured cells using an RNeasy Mini Kit (Qiagen) according to the manufacturer's instructions. RNA concentration was measured with NanoDrop ND-1000 Spectrophotometer (NanoDrop Technologies). The quality of the RNA extracted from the human tissues was controlled using a BioAnalyzed (Agilent Genomics). The samples we considered suitable for subsequent analysis if RNA integrity number (RIN) was at least 8.0. Complementary DNA synthesis was performed using High-Capacity cDNA Reverse Transcription Kit (Applied Biosystems, #4368813) with oligo(dT)18 primers (for human tissue samples) or random hexamer primers (for cell lines). In addition, a reaction without RNA and a reaction without reverse transcriptase enzyme were performed as controls for possible contamination by genomic DNA. RNA extraction of human tissues was performed by Marc Schneider (ThoraxKlinik, University Heidelberg) and Sebastian Marwitz (Research Center Borstel).

4.3.2 Quantitative real-time PCR

cDNA templates were analyzed by qRT-PCR on a LightCycler 480 (Roche Applied Science) cycler using the LightCycler 480 Probes Master with final 0.4 µM primer and 0.2 µM fluorescein-labeled hydrolysis probes (Universal Probe Library, Roche Applied Science). Crossing point values were calculated using the second-derivative-maximum method of the LightCycler 480 Basic Software (Roche Applied Science). Expression of target genes was normalized using the geometric mean of at least two housekeeper genes. All primers were designed using the UniversalProbe Library Assay Design Center (Roche Applied Science). Sequences of used PCR primers are listed in **Table 4.2**.

Gene ID	NCBI ID	Forward	Reverse	UPL #
BAMBI	NM_012342.2	cgccactccagctacatctt	cacagtagcatcgaatttca	71
CDH1	NM_004360.3	tggaggaattcttgctttgc	cgctctcctccgaagaaac	84
CDH2	NM_001792.3	ggtggaggagaagaagaccag	ggcatcaggctccacagt	66
ESD	NM_001984.1	tcagtctgcttcagaacatgg	cctttaatattgcagccacga	50
G6PD	NM_000402	ctgcagatgctgtgtctggt	tgcatttcaacaccttgacc	22
GAPDH	NM_002046	agccacatcgctcagacac	gcccaatacgaccaaatcc	60
GUSB	NM_000181.3	cgccctgcctatctgtattc	tccccacagggagtgtgtag	57
HPRT	NM_000194.2	tgaccttgatttattttgcatacc	cgagcaagacgttcagtcct	73
MYH9	NM_002473.5	tggaggaccagaactgcaa	ggttggtggtgaactcagcta	11
MYO10	NM_012334.2	cccagcagctgattcaagat	cgggttccgcttgtaaatc	31
MYO1E	NM_004998.3	gtgtcacagacgccagagag	gccgactggttgtttgtctc	24
PAI1	NM_000602	aaggcacctctgagaacttca	cccaggactaggcaggtg	19
PMEPA1	NM_020182.3	ctgcacggtccttcatcag	ttgcctgacactgtgctctc	76
RPS18	NM_022551.2	cttccacaggaggcctacac	cgcaaaatatgctggaacttt	46
SKI	NM_003036.3	gaagcaggaggagaagctcag	ccacgcgtaggaactcca	22
SKIL	NM_005414.4	gaggctgaatatgcaggacag	cttgcctatcggcctcag	13
SMAD6	NM_005585.4	gggcaaacccatagagacac	cgaggagacagccgagagt	10
SMAD7	NM_005904.3	acccgatggattttctcaaa	aggggccagataattcgttc	69
SMURF1	NM_020429.2	ttccgaaggcccatacct	cagcttctcgtagagcttctca	31
SMURF2	NM_022739.3	agaaattacatgagcagaacacattt	tgttgcgttgtcctctgttc	25
SNAI2	NM_003068.4	tggttgcttcaaggacacat	gcaaatgctctgttgcagtg	7
SPP1	NM_001040058.1	gagggcttggttgtcagc	caattctcatggtagtgagttttcc	18
TGFBR1	NM_004612	gcagacttaggactggcagtaag	agaacttcaggggccatgt	5
TGFBR2	NM_001024847	caccgcacgttcagaagtc	tggatgggcagtcctattaca	43
TWIST1	NM_000474.3	agctacgccttctcggtct	ccttctctggaaacaatgacatc	58
VIM	NM_003380.3	tacaggaagctgctggaagg	accagagggagtgaatccag	13
ZEB1	NM_001128128.2	aactgctgggaggatgacac	tcctgcttcatctgcctga	57

Table 4.2. List of primers for qRT-PCR. All genes are human. Sequences are shown in 5'–3' direction.

4.3.3 mRNA half-life analysis

5.5×10^5 of H1975 cells, or 7×10^5 of H838 cells, or 9×10^5 of H1650 cells were seeded in 6-cm dishes 2 days prior to experiment, growth factor depleted for 3 h and treated with 2 µg/ml actinomycin D (Sigma), an inhibitor of RNA polymerase. At the indicated time points, cells were lysed, total RNA was extracted and analyzed using qRT-PCR. mRNA fold change of the target genes was calculated relative to the time point

"0 h". For mRNA half-life analysis, mRNA expression values were not normalized to the housekeeper genes. mRNA half-life was determined by fitting the mRNA fold change expression values to an exponential decay two-parameter function:

$$N(t) = N_0 * e^{(-k*x)},$$

where *N(t)* is the mRNA quantity at time *t*, and N_0 is the starting amount of mRNA at time *t* = 0, and *K* is the decay constant. The half-life was calculated as:

$$\tau_{1/2} = \frac{\ln 2}{k}$$

4.3.4 RNA-Seq analysis

SK-MES1 cells were seeded on 6-cm dishes at a density of 10^6 cells/dish. Two days later, cells were growth factor-depleted for 3 h and stimulated with 2 ng/ml TGFβ1 or left untreated. Total RNA was extracted at the indicated time points and sequenced using HiSeq 4000 (Illumina). The RNA sequencing results were aligned to the GRCh38 reference genome (Ensembl Release 79) and transcript quantification was performed using kallisto (v0.43.0) (228). Subsequent transcript abundances were summarized to the gene level for analysis using tximport (v1.2.0) (229). All ID mapping was performed using biomaRt (v2.30.0) (230) and genes with read counts <10 were filtered out. Differential expression analysis was performed according to limma voom (v3.30.13) (317) to obtain *F*-values and adjusted *P*-values. Adjusted *P*-values were calculated by multiple testing correction according to the Benjamini–Hochberg procedure. Gene set enrichment analysis (GSEA) was performed on the *F*-values of the differential expression analysis according to GAGE (317). Upregulated GO cellular components terms (adjusted *P*-value <0.01) were used for network analysis and visualized using REVIGO with allowed similarity of 0.5 (199) and Cytoscape (318). The RNA-Seq data was deposited at the Sequence Read Archive (SRA) and is accessible via the Gene Expression Omnibus ID GSE95536. RNA sequencing was performed in the Genomics & Proteomics Core Facility (DKFZ, Heidelberg). RNA-Seq data processing and gene set enrichment analysis were performed by Sebastian Ohse (AG Busch/Börries, Freiburg University).

4.4 Microscopy

4.4.1 Fluorescence microscopy

SK-MES1 cells were seeded in 24-well plates (Zell Kontakt # 3231-20) with full DMEM containing no Phenol red (Lonza), allowed to attach overnight and then stimulated with 2 ng/ml TGFβ1 or left untreated. Three days later cells were washed with PBS, fixed with 3.7% PFA for 10 min and stained with Phalloidin-488 and Hoechst (Santa Cruz, #sc-396575). Imaging was performed using wide-field fluorescence microscope (IX81, Olympus) equipped with UPlanSApo 10×/0.4 NA objective lens (Olympus). Image analysis was performed using ImageJ (NIH).

4.4.2 2D migration assay

Cells were seeded in 24-well plate (Zell Kontakt #3231-20) at a density of 25,000 cells/well, allowed to attach overnight, growth factor depleted for 3 h, stained with Hoechst (Santa Cruz, #sc-396575), stimulated with 2 ng/ml TGFβ (R&D Systems, #240-B-010) alone or in combination with 5 µM SB-431542, an inhibitor of type I TGFβ receptor, and imaged on an environment-controlled microscope (IX81, Olympus). Nine positions per well (3×3 grid) were acquired with UPlanSApo 10×/0.4 NA objective lens (Olympus) in 20 min intervals for 60 h. Images were stitched with the Grid/Collection ImageJ plugin. Single cell tracking was performed with the ImageJ Mtrack2 plugin. The speed of each tracked cell was calculated by dividing total travelled distance by total time for which the cell was tracked. 2D migration experiments were performed by Irina Titkova (DKFZ, Heidelberg).

4.4.3 3D collagen invasion assay

3D collagen gels were prepared as described previously (319). Briefly, ice-cold 1 M HEPES buffer, 0.7 M NaOH, 10× PBS pH 8.0 and bovine skin collagen G solution (L1613, Biochrome) were mixed in 1:1:2:16 ratio. 50 µl of the resulting solution was added per well of a 96-well flat bottom plate (BD #353376). Plates were kept overnight at 4°C and subsequently at 37°C for 2 h to solidify the collagen. After gelation, 12,500 of SK-MES1 cells per well were seeded on top of the matrix, allowed to adhere overnight, stimulated with 2 ng/ml TGFβ1 in growth factor depleted medium and incubated for 4 days. Afterwards, cells were fixed in 3.7% paraffin for 1 h and subsequently stained with Hoechst (Santa Cruz, #sc-396575). Collagen embedded cells were imaged using a LSM710 confocal microscope (Carl Zeiss) equipped with a EC Plan-Neofluar DIC 10×/0.3 NA objective lens (Carl Zeiss). For each well, 2×2 tile z-stacks were acquired. Image analysis was performed using Imaris software (Bitplane). Spot detection

algorithm was applied to assign coordinates for the center of each cell nucleus. Coordinates of all detected nuclei were exported and corrected by a conical plane function using the InvasionCorrection R package (320). The threshold for invasion was set to 30 µm. Percentage of invaded cells and the invasion depth were the output. 3D collagen invasion experiments were performed by Magdalena Szczygieł (DKFZ, Heidelberg).

4.5 Mouse experiments

4.5.1 Lung colonization assay

All experiments were in accordance with the approved guidelines of the responsible national authority, the local Governmental Committee for Animal Experimentation (Regierungspräsidium Karlsruhe, Germany, license G193/10). Mice were maintained at a 12-hour light-dark cycle with unrestricted diet and water. 2×10^6 of A549-GFP and A549-BAMBI-GFP cells in 100 µl of PBS were intravenously (i.v.) injected into the lateral tail vein of 7–8-week-old female $NMRI^{nu/nu}$ mice purchased from Charles River (Sulzfeld) and kept on Kliba diet 3307 with n = 12 randomized mice/group. Three days prior to cell inoculation, mice were treated with 5 mg/ml doxycycline (DOX) in drinking water containing 5% saccharose for the duration of the entire experiment. TGFβ was intraperitoneally (i.p.) injected (4 µg/kg bodyweight, dissolved at 400 ng/ml in 4 mM HCl containing 0.1% mouse serum albumin, 10 µl/g mouse) once daily at days 1, 6, 11, and 16 post cell inoculation. Prior to cervical dislocation on day 70 post cell inoculation, blood was collected under isoflurane inhalation anesthesia (1–1.5% in O_2, 0.5 l/min) from the retrobulbar plexus. No mice were lost due to adverse effects of TGFβ. Mouse experiment were performed with assistance from the DKFZ tumor models core facility.

4.5.2 Mouse lung colonization assay analysis

Mouse lungs were dissected and separated into left and right lung and subsequently HOPE-fixed. All lung tissue specimens were randomly cut and mounted on SuperFrost slides for hematoxylin and eosin (H&E) staining. For the quantification of the lung tumor burden, the right and left lung of each animal were analyzed by histology-trained investigators and images were taken at 10× magnification. The area of tumors within the lungs was manually tagged within the Infinity Analyze software (Lumenera) and tumor area per animal was quantified using a calibrated micrometer slide. The total area of lung tumor burden was calculated from the sum of individual tumor nodule areas within the alveolar region of both

lungs from each animal. To calculate the metastatic potential of A549-GFP and A549-BAMBI-GFP cells the tumor nodules consisting of at least two connected tumor cells were manually counted. Human origin of lung tumor cells within the mouse lungs was verified via immunohistochemistry using rabbit anti human HLA-A antibody (Abcam, clone EP1395У). Activation of the TGFβ pathway within human lung tumor cells was investigated by immunohistochemical analysis of Smad3 phosphorylation. Histology staining and analysis was performed by Sebastian Marwitz (Research Center Borstel).

4.6 Human tissues analysis

4.6.1 Tissue sample collection and characterization

For the BAMBI study (**section 2.1**) lung tissue samples were obtained from patients who underwent lobectomy or pneumectomy due to therapeutic interventions at the LungenClinic Grosshansdorf, Germany. Residual tumor and tumor-free lung tissues not needed for diagnostic purposes were HOPE-fixed and paraffin-embedded according to manufacturer´s instructions (DCS Innovative Systeme). The use of patient materials was approved by local ethics committee of the University of Lübeck (AZ 12-220), Germany. For analysis in cancer tissues, 133 archived lung cancer specimens of either adenocarcinoma or squamous cell carcinoma diagnosis were randomly selected and subjected to immunohistochemistry. The gender ratio was 43 female vs. 90 male patients and the mean age at time of diagnosis was 66.06 years (± 9.9). Among the investigated lung cancer specimen, 74 were squamous cell carcinomas (55.6%) and 59 adenocarcinomas (44.4%). As controls, 23 cases of tumor-free lung specimen were included, four of which were paired with lung cancer specimen. Tissues and corresponding clinical data were collected by Sebastian Marwitz (Research Center Borstel).

For the MYO10 study (**section 2.2**) tissue samples were provided by Lung Biobank Heidelberg, a member of the accredited Tissue Bank of the National Center for Tumor Diseases (NCT) Heidelberg, the BioMaterialBank Heidelberg and the Biobank platform of the German Center for Lung Research (DZL). All patients provided written informed consent for the use of the tissue for research purpose. The study was approved by the local ethics committee of the University of Heidelberg (No. 270/2001). Tumor and matched distant (> 5 cm) normal lung tissue samples from NSCLC patients (n = 362) who underwent resection for primary lung cancer at the Thoraxklinik at University Hospital, Heidelberg, Germany were collected. All diagnoses were made according to the 2004 WHO classification for lung cancer (321) by at

least two experienced pathologists. Tissues were snap-frozen within 30 minutes after resection and stored at -80°C until the time of analysis. Only samples with a viable tumor content of ≥ 50% were used for subsequent analyses. Tissues and corresponding clinical data were collected by Marc Schneider (ThoraxKlinik, University Heidelberg).

4.6.2 Histology analysis

Fixed, paraffin-embedded tissues and tissue microarrays were cut on a microtome (Leica SM 2000) to obtain 1-µm thick sections that were mounted on SuperFrost (Menzel Gläser) glass slides. Subsequent deparaffinization was done by incubation in 100% isopropanol for 10 min at 65°C. Sections were shortly air dried, rehydrated in 70% acetone for 10 min at 4°C and transferred into distilled water for 10 min at 4°C. Endogenous peroxidases were blocked by incubation in 3% H_2O_2 for 10 min. Primary antibodies were diluted with antibody diluent (Zytomed Systems) and incubated overnight with primary antibodies (**Table 4.3**). For visualization, a HRP-conjugated polymer kit was used according to manufacturer`s instructions (ZytoChemPlus Kit, Zytomed Systems). Chromogenic reaction was conducted with permanent AEC (Permanent AEC Kit, Zytomed Sytems) and stopped with distilled water. The slides were subsequently dehydrated in graded series of ethanol (70%, 90%, 2× 95%, 2× 100%, xylene) and mounted with Pertex (Medite). Negative controls were included by omission of primary antibody in each staining and photomicrographs were taken with a CCD camera (Infinity 4, Lumenera). Contrast and brightness of images were adjusted using FixFoto software (Joachim Koopman Software).

Target	Species	Dilution	Company	Clone number
BAMBI	mouse	1:100	eBioscience	clone 4e8
BAMBI	rabbit	1:100	Sigma-Aldrich	clone 3C1-1D1
Smad2	rabbit	1:100	Cell Signaling	clone D43B4
pSmad2	rabbit	1:100	Cell Signaling	clone 138D4
Smad3	rabbit	1:100	Cell Signaling	clone C67H9
pSmad3	rabbit	1:100	Cell Signaling	clone C25A9
Smad4	rabbit	1:100	Cell Signaling	clone EP618Y
TGFβ	rabbit	1:100	Abcam	#ab92486
SnoN	rabbit	1:100	Abcam	clone 2F6
Smad7	mouse	1:100	R&D Systems	clone 293039

Table 4.3. List of primary antibodies used for immunohistochemistry.

For evaluation of target expression, a semi-quantitative score was applied based on histology analysis of the whole specimen as following: negative (0), focal and weak expression (1), frequent intermediate expression (2), strong expression and dominating feature of specimen (3). The whole specimen was considered for evaluation of microscopic slides. Histology staining and analysis was performed by Sebastian Marwitz (Research Center Borstel).

4.6.3 Kaplan–Meier survival analysis

Patient survival was calculated from the date of surgery until the last date of contact or death. Univariate analysis of survival data was performed according to Kaplan and Meier (322) and using Cox proportional hazard models. Multivariate survival analysis was performed using the Cox proportional hazards model. The non-parametric Mann-Whitney U test was used to investigate significant differences between the patient groups. Survival analysis was performed by Thomas Muley (ThoraxKlinik, University Heidelberg).

4.7 Mathematical dynamic pathway modeling

The assumed structure of TGFβ signal transduction pathway was translated into a system of ordinary differential equations (ODEs) using the D2D MatLab software package (323). All reactions were implemented as mass-action kinetics. The dynamic parameters of the model were estimated using a multi-start approach based on Latin hypercube sampling (324). The steady state concentrations of the signaling components in unstimulated cells were analytically calculated and did not change within the time scale of experiments. Concentrations of Smad2, Smad3 and Smad4 were fixed to the absolute concentrations that were determined experimentally (**section 2.3.1**). Absolute degree of Smad2 phosphorylation determined by mass spectrometry was modeled without any scaling and offset parameters. To describe cell line-specific differences an additional scaling parameter *r* was introduced in the reactions that were assumed to be different in comparison to H1975 cell line. The full list of the dynamic variables, model reactions, conditions and equations is provided in the **section 6.3**. Quantitative mathematical modeling of the TGFβ signaling pathway was performed by Raphael Engesser (AG Timmer, Freiburg University).

5 References

1. Torre LA, Siegel RL, Jemal A. Lung Cancer Statistics. Advances in experimental medicine and biology. 2016;893:1-19.

2. Travis WD. Pathology of lung cancer. Clinics in chest medicine. 2011;32(4):669-92.

3. A genomics-based classification of human lung tumors. Sci Transl Med. 2013;5(209):209ra153.

4. Law MR, Morris JK, Watt HC, Wald NJ. The dose-response relationship between cigarette consumption, biochemical markers and risk of lung cancer. Br J Cancer. 1997;75(11):1690-3.

5. Samet JM, Avila-Tang E, Boffetta P, Hannan LM, Olivo-Marston S, Thun MJ, et al. Lung cancer in never smokers: clinical epidemiology and environmental risk factors. Clin Cancer Res. 2009;15(18):5626-45.

6. Kandoth C, McLellan MD, Vandin F, Ye K, Niu B, Lu C, et al. Mutational landscape and significance across 12 major cancer types. Nature. 2013;502(7471):333-9.

7. Govindan R, Ding L, Griffith M, Subramanian J, Dees ND, Kanchi KL, et al. Genomic landscape of non-small cell lung cancer in smokers and never-smokers. Cell. 2012;150(6):1121-34.

8. Stratton MR, Campbell PJ, Futreal PA. The cancer genome. Nature. 2009;458(7239):719-24.

9. Lawrence MS, Stojanov P, Mermel CH, Robinson JT, Garraway LA, Golub TR, et al. Discovery and saturation analysis of cancer genes across 21 tumour types. Nature. 2014;505(7484):495-501.

10. Devarakonda S, Morgensztern D, Govindan R. Genomic alterations in lung adenocarcinoma. Lancet Oncol. 2015;16(7):e342-51.

11. Cancer Genome Atlas Research N. Comprehensive genomic characterization of squamous cell lung cancers. Nature. 2012;489(7417):519-25.

12. Mok T, Yang JJ, Lam KC. Treating patients with EGFR-sensitizing mutations: first line or second line--is there a difference? J Clin Oncol. 2013;31(8):1081-8.

13. Shaw AT, Kim DW, Nakagawa K, Seto T, Crino L, Ahn MJ, et al. Crizotinib versus chemotherapy in advanced ALK-positive lung cancer. N Engl J Med. 2013;368(25):2385-94.

14. Borghaei H, Paz-Ares L, Horn L, Spigel DR, Steins M, Ready NE, et al. Nivolumab versus Docetaxel in Advanced Nonsquamous Non-Small-Cell Lung Cancer. N Engl J Med. 2015;373(17):1627-39.

15. Brahmer J, Reckamp KL, Baas P, Crino L, Eberhardt WE, Poddubskaya E, et al. Nivolumab versus Docetaxel in Advanced Squamous-Cell Non-Small-Cell Lung Cancer. N Engl J Med. 2015;373(2):123-35.

16. Siegel R, Naishadham D, Jemal A. Cancer statistics, 2013. CA Cancer J Clin. 2013;63(1):11-30.

17. Rami-Porta R, Crowley JJ, Goldstraw P. The revised TNM staging system for lung cancer. Ann Thorac Cardiovasc Surg. 2009;15(1):4-9.

18. Sandler A, Gray R, Perry MC, Brahmer J, Schiller JH, Dowlati A, et al. Paclitaxel-carboplatin alone or with bevacizumab for non-small-cell lung cancer. N Engl J Med. 2006;355(24):2542-50.

19. Jackman D, Pao W, Riely GJ, Engelman JA, Kris MG, Janne PA, et al. Clinical definition of acquired resistance to epidermal growth factor receptor tyrosine kinase inhibitors in non-small-cell lung cancer. J Clin Oncol. 2010;28(2):357-60.

20. Doebele RC, Pilling AB, Aisner DL, Kutateladze TG, Le AT, Weickhardt AJ, et al. Mechanisms of resistance to crizotinib in patients with ALK gene rearranged non-small cell lung cancer. Clin Cancer Res. 2012;18(5):1472-82.

21. Sequist LV, Waltman BA, Dias-Santagata D, Digumarthy S, Turke AB, Fidias P, et al. Genotypic and histological evolution of lung cancers acquiring resistance to EGFR inhibitors. Sci Transl Med. 2011;3(75):75ra26.

22. Voulgari A, Pintzas A. Epithelial-mesenchymal transition in cancer metastasis: mechanisms, markers and strategies to overcome drug resistance in the clinic. Biochim Biophys Acta. 2009;1796(2):75-90.

23. Singh A, Settleman J. EMT, cancer stem cells and drug resistance: an emerging axis of evil in the war on cancer. Oncogene. 2010;29(34):4741-51.

24. Sekine I, Minna JD, Nishio K, Tamura T, Saijo N. A literature review of molecular markers predictive of clinical response to cytotoxic chemotherapy in patients with lung cancer. J Thorac Oncol. 2006;1(1):31-7.

25. Reck M, Heigener DF, Mok T, Soria JC, Rabe KF. Management of non-small-cell lung cancer: recent developments. Lancet. 2013;382(9893):709-19.

26. Roberts AB, Anzano MA, Lamb LC, Smith JM, Sporn MB. New class of transforming growth factors potentiated by epidermal growth factor: isolation from non-neoplastic tissues. Proc Natl Acad Sci U S A. 1981;78(9):5339-43.

27. Alexandrow MG, Moses HL. Transforming growth factor beta and cell cycle regulation. Cancer Res. 1995;55(7):1452-7.

28. Morikawa M, Derynck R, Miyazono K. TGF-beta and the TGF-beta Family: Context-Dependent Roles in Cell and Tissue Physiology. Cold Spring Harbor perspectives in biology. 2016;8(5).

29. Massague J. TGFbeta signalling in context. Nat Rev Mol Cell Biol. 2012;13(10):616-30.

30. Radaev S, Zou Z, Huang T, Lafer EM, Hinck AP, Sun PD. Ternary complex of transforming growth factor-beta1 reveals isoform-specific ligand recognition and receptor recruitment in the superfamily. J Biol Chem. 2010;285(19):14806-14.

31. Wrana JL, Attisano L, Wieser R, Ventura F, Massague J. Mechanism of activation of the TGF-beta receptor. Nature. 1994;370(6488):341-7.

32. Abdollah S, Macias-Silva M, Tsukazaki T, Hayashi H, Attisano L, Wrana JL. TbetaRI phosphorylation of Smad2 on Ser465 and Ser467 is required for Smad2-Smad4 complex formation and signaling. J Biol Chem. 1997;272(44):27678-85.

33. Feng XH, Derynck R. Specificity and versatility in tgf-beta signaling through Smads. Annu Rev Cell Dev Biol. 2005;21:659-93.

34. Heldin CH, Moustakas A. Signaling Receptors for TGF-beta Family Members. Cold Spring Harbor perspectives in biology. 2016;8(8).

35. Hanyu A, Ishidou Y, Ebisawa T, Shimanuki T, Imamura T, Miyazono K. The N domain of Smad7 is essential for specific inhibition of transforming growth factor-beta signaling. J Cell Biol. 2001;155(6):1017-27.

36. Goto K, Kamiya Y, Imamura T, Miyazono K, Miyazawa K. Selective inhibitory effects of Smad6 on bone morphogenetic protein type I receptors. J Biol Chem. 2007;282(28):20603-11.

37. Nakao A, Afrakhte M, Moren A, Nakayama T, Christian JL, Heuchel R, et al. Identification of Smad7, a TGFbeta-inducible antagonist of TGF-beta signalling. Nature. 1997;389(6651):631-5.

38. Imamura T, Takase M, Nishihara A, Oeda E, Hanai J, Kawabata M, et al. Smad6 inhibits signalling by the TGF-beta superfamily. Nature. 1997;389(6651):622-6.

39. Yagi K, Goto D, Hamamoto T, Takenoshita S, Kato M, Miyazono K. Alternatively spliced variant of Smad2 lacking exon 3. Comparison with wild-type Smad2 and Smad3. J Biol Chem. 1999;274(2):703-9.

40. Qin BY, Lam SS, Correia JJ, Lin K. Smad3 allostery links TGF-beta receptor kinase activation to transcriptional control. Genes Dev. 2002;16(15):1950-63.

41. Massague J, Seoane J, Wotton D. Smad transcription factors. Genes Dev. 2005;19(23):2783-810.

42. Moustakas A, Heldin CH. The regulation of TGFbeta signal transduction. Development. 2009;136(22):3699-714.

43. Xu P, Lin X, Feng XH. Posttranslational Regulation of Smads. Cold Spring Harbor perspectives in biology. 2016;8(12).

44. ten Dijke P, Hill CS. New insights into TGF-beta-Smad signalling. Trends Biochem Sci. 2004;29(5):265-73.

45. Groppe J, Hinck CS, Samavarchi-Tehrani P, Zubieta C, Schuermann JP, Taylor AB, et al. Cooperative assembly of TGF-beta superfamily signaling complexes is mediated by two disparate mechanisms and distinct modes of receptor binding. Mol Cell. 2008;29(2):157-68.

46. Miyazono K, Olofsson A, Colosetti P, Heldin CH. A role of the latent TGF-beta 1-binding protein in the assembly and secretion of TGF-beta 1. Embo J. 1991;10(5):1091-101.

47. Annes JP, Munger JS, Rifkin DB. Making sense of latent TGFbeta activation. J Cell Sci. 2003;116(Pt 2):217-24.

48. Zhang YE. Non-Smad Signaling Pathways of the TGF-beta Family. Cold Spring Harbor perspectives in biology. 2016.

49. Di Guglielmo GM, Le Roy C, Goodfellow AF, Wrana JL. Distinct endocytic pathways regulate TGF-beta receptor signalling and turnover. Nat Cell Biol. 2003;5(5):410-21.

50. Kavsak P, Rasmussen RK, Causing CG, Bonni S, Zhu H, Thomsen GH, et al. Smad7 binds to Smurf2 to form an E3 ubiquitin ligase that targets the TGF beta receptor for degradation. Mol Cell. 2000;6(6):1365-75.

51. Ebisawa T, Fukuchi M, Murakami G, Chiba T, Tanaka K, Imamura T, et al. Smurf1 interacts with transforming growth factor-beta type I receptor through Smad7 and induces receptor degradation. J Biol Chem. 2001;276(16):12477-80.

52. Ohashi N, Yamamoto T, Uchida C, Togawa A, Fukasawa H, Fujigaki Y, et al. Transcriptional induction of Smurf2 ubiquitin ligase by TGF-beta. FEBS Lett. 2005;579(12):2557-63.

53. Eichhorn PJ, Rodon L, Gonzalez-Junca A, Dirac A, Gili M, Martinez-Saez E, et al. USP15 stabilizes TGF-beta receptor I and promotes oncogenesis through the activation of TGF-beta signaling in glioblastoma. Nat Med. 2012;18(3):429-35.

54. Zhang L, Zhou F, Drabsch Y, Gao R, Snaar-Jagalska BE, Mickanin C, et al. USP4 is regulated by AKT phosphorylation and directly deubiquitylates TGF-beta type I receptor. Nat Cell Biol. 2012;14(7):717-26.

55. Al-Salihi MA, Herhaus L, Macartney T, Sapkota GP. USP11 augments TGFbeta signalling by deubiquitylating ALK5. Open biology. 2012;2(6):120063.

56. Millet C, Yamashita M, Heller M, Yu LR, Veenstra TD, Zhang YE. A negative feedback control of transforming growth factor-beta signaling by glycogen synthase kinase 3-mediated Smad3 linker phosphorylation at Ser-204. J Biol Chem. 2009;284(30):19808-16.

57. Wrighton KH, Feng XH. To (TGF)beta or not to (TGF)beta: fine-tuning of Smad signaling via post-translational modifications. Cell Signal. 2008;20(9):1579-91.

58. Gao S, Alarcon C, Sapkota G, Rahman S, Chen PY, Goerner N, et al. Ubiquitin ligase Nedd4L targets activated Smad2/3 to limit TGF-beta signaling. Mol Cell. 2009;36(3):457-68.

59. Aragon E, Goerner N, Zaromytidou AI, Xi Q, Escobedo A, Massague J, et al. A Smad action turnover switch operated by WW domain readers of a phosphoserine code. Genes Dev. 2011;25(12):1275-88.

60. Onichtchouk D, Chen YG, Dosch R, Gawantka V, Delius H, Massague J, et al. Silencing of TGF-beta signalling by the pseudoreceptor BAMBI. Nature. 1999;401(6752):480-5.

61. Huse M, Chen YG, Massague J, Kuriyan J. Crystal structure of the cytoplasmic domain of the type I TGF beta receptor in complex with FKBP12. Cell. 1999;96(3):425-36.

62. Watanabe Y, Itoh S, Goto T, Ohnishi E, Inamitsu M, Itoh F, et al. TMEPAI, a transmembrane TGF-beta-inducible protein, sequesters Smad proteins from active participation in TGF-beta signaling. Mol Cell. 2010;37(1):123-34.

63. Nakano N, Maeyama K, Sakata N, Itoh F, Akatsu R, Nakata M, et al. C18 ORF1, a novel negative regulator of transforming growth factor-beta signaling. J Biol Chem. 2014;289(18):12680-92.

64. Shi W, Sun C, He B, Xiong W, Shi X, Yao D, et al. GADD34-PP1c recruited by Smad7 dephosphorylates TGFbeta type I receptor. J Cell Biol. 2004;164(2):291-300.

65. Griswold-Prenner I, Kamibayashi C, Maruoka EM, Mumby MC, Derynck R. Physical and functional interactions between type I transforming growth factor beta receptors and Balpha, a WD-40 repeat subunit of phosphatase 2A. Mol Cell Biol. 1998;18(11):6595-604.

66. Lin X, Duan X, Liang YY, Su Y, Wrighton KH, Long J, et al. PPM1A functions as a Smad phosphatase to terminate TGFbeta signaling. Cell. 2006;125(5):915-28.

67. Yu J, Pan L, Qin X, Chen H, Xu Y, Chen Y, et al. MTMR4 attenuates transforming growth factor beta (TGFbeta) signaling by dephosphorylating R-Smads in endosomes. J Biol Chem. 2010;285(11):8454-62.

68. Stroschein SL, Wang W, Zhou S, Zhou Q, Luo K. Negative feedback regulation of TGF-beta signaling by the SnoN oncoprotein. Science. 1999;286(5440):771-4.

69. Luo K, Stroschein SL, Wang W, Chen D, Martens E, Zhou S, et al. The Ski oncoprotein interacts with the Smad proteins to repress TGFbeta signaling. Genes Dev. 1999;13(17):2196-206.

70. Wotton D, Lo RS, Lee S, Massague J. A Smad transcriptional corepressor. Cell. 1999;97(1):29-39.

71. Deheuninck J, Luo K. Ski and SnoN, potent negative regulators of TGF-beta signaling. Cell Res. 2009;19(1):47-57.

72. Luo T, Cui S, Bian C, Yu X. Crosstalk between TGF-beta/Smad3 and BMP/BMPR2 signaling pathways via miR-17-92 cluster in carotid artery restenosis. Molecular and cellular biochemistry. 2014;389(1-2):169-76.

73. Huang S, He X, Ding J, Liang L, Zhao Y, Zhang Z, et al. Upregulation of miR-23a approximately 27a approximately 24 decreases transforming growth factor-beta-induced tumor-suppressive activities in human hepatocellular carcinoma cells. Int J Cancer. 2008;123(4):972-8.

74. Swingler TE, Wheeler G, Carmont V, Elliott HR, Barter MJ, Abu-Elmagd M, et al. The expression and function of microRNAs in chondrogenesis and osteoarthritis. Arthritis and rheumatism. 2012;64(6):1909-19.

75. Li L, Shi JY, Zhu GQ, Shi B. MiR-17-92 cluster regulates cell proliferation and collagen synthesis by targeting TGFB pathway in mouse palatal mesenchymal cells. J Cell Biochem. 2012;113(4):1235-44.

76. Yang H, Fang F, Chang R, Yang L. MicroRNA-140-5p suppresses tumor growth and metastasis by targeting transforming growth factor beta receptor 1 and fibroblast growth factor 9 in hepatocellular carcinoma. Hepatology. 2013;58(1):205-17.

77. Massague J. TGF-beta signaling in development and disease. FEBS Lett. 2012;586(14):1833.

78. Lebrun JJ. The Dual Role of TGFbeta in Human Cancer: From Tumor Suppression to Cancer Metastasis. ISRN molecular biology. 2012;2012:381428.

79. Seoane J, Pouponnot C, Staller P, Schader M, Eilers M, Massague J. TGFbeta influences Myc, Miz-1 and Smad to control the CDK inhibitor p15INK4b. Nat Cell Biol. 2001;3(4):400-8.

80. Gomis RR, Alarcon C, He W, Wang Q, Seoane J, Lash A, et al. A FoxO-Smad synexpression group in human keratinocytes. Proc Natl Acad Sci U S A. 2006;103(34):12747-52.

81. Chen CR, Kang Y, Siegel PM, Massague J. E2F4/5 and p107 as Smad cofactors linking the TGFbeta receptor to c-myc repression. Cell. 2002;110(1):19-32.

82. Staller P, Peukert K, Kiermaier A, Seoane J, Lukas J, Karsunky H, et al. Repression of p15INK4b expression by Myc through association with Miz-1. Nat Cell Biol. 2001;3(4):392-9.

83. Ohgushi M, Kuroki S, Fukamachi H, O'Reilly LA, Kuida K, Strasser A, et al. Transforming growth factor beta-dependent sequential activation of Smad, Bim, and caspase-9 mediates physiological apoptosis in gastric epithelial cells. Mol Cell Biol. 2005;25(22):10017-28.

84. Jang CW, Chen CH, Chen CC, Chen JY, Su YH, Chen RH. TGF-beta induces apoptosis through Smad-mediated expression of DAP-kinase. Nat Cell Biol. 2002;4(1):51-8.

85. Saltzman A, Munro R, Searfoss G, Franks C, Jaye M, Ivashchenko Y. Transforming growth factor-beta-mediated apoptosis in the Ramos B-lymphoma cell line is accompanied by caspase activation and Bcl-XL downregulation. Exp Cell Res. 1998;242(1):244-54.

86. Francis JM, Heyworth CM, Spooncer E, Pierce A, Dexter TM, Whetton AD. Transforming growth factor-beta 1 induces apoptosis independently of p53 and selectively reduces expression of Bcl-2 in multipotent hematopoietic cells. J Biol Chem. 2000;275(50):39137-45.

87. Wang J, Yang L, Yang J, Kuropatwinski K, Wang W, Liu XQ, et al. Transforming growth factor beta induces apoptosis through repressing the phosphoinositide 3-kinase/AKT/survivin pathway in colon cancer cells. Cancer Res. 2008;68(9):3152-60.

88. Sorrentino A, Thakur N, Grimsby S, Marcusson A, von Bulow V, Schuster N, et al. The type I TGF-beta receptor engages TRAF6 to activate TAK1 in a receptor kinase-independent manner. Nat Cell Biol. 2008;10(10):1199-207.

89. Perlman R, Schiemann WP, Brooks MW, Lodish HF, Weinberg RA. TGF-beta-induced apoptosis is mediated by the adapter protein Daxx that facilitates JNK activation. Nat Cell Biol. 2001;3(8):708-14.

90. Franklin CC, Rosenfeld-Franklin ME, White C, Kavanagh TJ, Fausto N. TGFbeta1-induced suppression of glutathione antioxidant defenses in hepatocytes: caspase-dependent post-translational and caspase-independent transcriptional regulatory mechanisms. FASEB J. 2003;17(11):1535-7.

91. Yang H, Kyo S, Takatura M, Sun L. Autocrine transforming growth factor beta suppresses telomerase activity and transcription of human telomerase reverse transcriptase in human cancer cells. Cell growth & differentiation : the molecular biology journal of the American Association for Cancer Research. 2001;12(2):119-27.

92. Lacerte A, Korah J, Roy M, Yang XJ, Lemay S, Lebrun JJ. Transforming growth factor-beta inhibits telomerase through SMAD3 and E2F transcription factors. Cell Signal. 2008;20(1):50-9.

93. Markowitz S, Wang J, Myeroff L, Parsons R, Sun L, Lutterbaugh J, et al. Inactivation of the type II TGF-beta receptor in colon cancer cells with microsatellite instability. Science. 1995;268(5215):1336-8.

94. Ogino S, Kawasaki T, Ogawa A, Kirkner GJ, Loda M, Fuchs CS. TGFBR2 mutation is correlated with CpG island methylator phenotype in microsatellite instability-high colorectal cancer. Human pathology. 2007;38(4):614-20.

95. Shima K, Morikawa T, Yamauchi M, Kuchiba A, Imamura Y, Liao X, et al. TGFBR2 and BAX mononucleotide tract mutations, microsatellite instability, and prognosis in 1072 colorectal cancers. PLoS One. 2011;6(9):e25062.

96. Chen T, Carter D, Garrigue-Antar L, Reiss M. Transforming growth factor beta type I receptor kinase mutant associated with metastatic breast cancer. Cancer Res. 1998;58(21):4805-10.

97. Goggins M, Shekher M, Turnacioglu K, Yeo CJ, Hruban RH, Kern SE. Genetic alterations of the transforming growth factor beta receptor genes in pancreatic and biliary adenocarcinomas. Cancer Res. 1998;58(23):5329-32.

98. Wang D, Kanuma T, Mizunuma H, Takama F, Ibuki Y, Wake N, et al. Analysis of specific gene mutations in the transforming growth factor-beta signal transduction pathway in human ovarian cancer. Cancer Res. 2000;60(16):4507-12.

99. Kim SJ, Im YH, Markowitz SD, Bang YJ. Molecular mechanisms of inactivation of TGF-beta receptors during carcinogenesis. Cytokine & growth factor reviews. 2000;11(1-2):159-68.

100. Hahn SA, Schutte M, Hoque AT, Moskaluk CA, da Costa LT, Rozenblum E, et al. DPC4, a candidate tumor suppressor gene at human chromosome 18q21.1. Science. 1996;271(5247):350-3.

101. Sjoblom T, Jones S, Wood LD, Parsons DW, Lin J, Barber TD, et al. The consensus coding sequences of human breast and colorectal cancers. Science. 2006;314(5797):268-74.

102. Derynck R, Akhurst RJ, Balmain A. TGF-beta signaling in tumor suppression and cancer progression. Nat Genet. 2001;29(2):117-29.

103. Wakefield LM, Roberts AB. TGF-beta signaling: positive and negative effects on tumorigenesis. Current opinion in genetics & development. 2002;12(1):22-9.

104. Nagata H, Hatano E, Tada M, Murata M, Kitamura K, Asechi H, et al. Inhibition of c-Jun NH2-terminal kinase switches Smad3 signaling from oncogenesis to tumor- suppression in rat hepatocellular carcinoma. Hepatology. 2009;49(6):1944-53.

105. Akhurst RJ, Derynck R. TGF-beta signaling in cancer--a double-edged sword. Trends Cell Biol. 2001;11(11):S44-51.

106. Seoane J, Le HV, Shen L, Anderson SA, Massague J. Integration of Smad and forkhead pathways in the control of neuroepithelial and glioblastoma cell proliferation. Cell. 2004;117(2):211-23.

107. Blobe GC, Schiemann WP, Lodish HF. Role of transforming growth factor beta in human disease. N Engl J Med. 2000;342(18):1350-8.

108. Acloque H, Adams MS, Fishwick K, Bronner-Fraser M, Nieto MA. Epithelial-mesenchymal transitions: the importance of changing cell state in development and disease. J Clin Invest. 2009;119(6):1438-49.

109. Yang J, Weinberg RA. Epithelial-mesenchymal transition: at the crossroads of development and tumor metastasis. Dev Cell. 2008;14(6):818-29.

110. Lamouille S, Xu J, Derynck R. Molecular mechanisms of epithelial-mesenchymal transition. Nat Rev Mol Cell Biol. 2014;15(3):178-96.

111. Friedl P, Locker J, Sahai E, Segall JE. Classifying collective cancer cell invasion. Nat Cell Biol. 2012;14(8):777-83.

112. Pece S, Tosoni D, Confalonieri S, Mazzarol G, Vecchi M, Ronzoni S, et al. Biological and molecular heterogeneity of breast cancers correlates with their cancer stem cell content. Cell. 2010;140(1):62-73.

113. Merlos-Suarez A, Barriga FM, Jung P, Iglesias M, Cespedes MV, Rossell D, et al. The intestinal stem cell signature identifies colorectal cancer stem cells and predicts disease relapse. Cell Stem Cell. 2011;8(5):511-24.

114. Baccelli I, Schneeweiss A, Riethdorf S, Stenzinger A, Schillert A, Vogel V, et al. Identification of a population of blood circulating tumor cells from breast cancer patients that initiates metastasis in a xenograft assay. Nature biotechnology. 2013;31(6):539-44.

115. Al-Hajj M, Wicha MS, Benito-Hernandez A, Morrison SJ, Clarke MF. Prospective identification of tumorigenic breast cancer cells. Proc Natl Acad Sci U S A. 2003;100(7):3983-8.

116. Anido J, Saez-Borderias A, Gonzalez-Junca A, Rodon L, Folch G, Carmona MA, et al. TGF-beta Receptor Inhibitors Target the CD44(high)/Id1(high) Glioma-Initiating Cell Population in Human Glioblastoma. Cancer cell. 2010;18(6):655-68.

117. Penuelas S, Anido J, Prieto-Sanchez RM, Folch G, Barba I, Cuartas I, et al. TGF-beta increases glioma-initiating cell self-renewal through the induction of LIF in human glioblastoma. Cancer cell. 2009;15(4):315-27.

118. You H, Ding W, Rountree CB. Epigenetic regulation of cancer stem cell marker CD133 by transforming growth factor-beta. Hepatology. 2010;51(5):1635-44.

119. Yu M, Bardia A, Wittner BS, Stott SL, Smas ME, Ting DT, et al. Circulating breast tumor cells exhibit dynamic changes in epithelial and mesenchymal composition. Science. 2013;339(6119):580-4.

120. Aktas B, Tewes M, Fehm T, Hauch S, Kimmig R, Kasimir-Bauer S. Stem cell and epithelial-mesenchymal transition markers are frequently overexpressed in circulating tumor cells of metastatic breast cancer patients. Breast cancer research : BCR. 2009;11(4):R46.

121. Pertovaara L, Kaipainen A, Mustonen T, Orpana A, Ferrara N, Saksela O, et al. Vascular endothelial growth factor is induced in response to transforming growth factor-beta in fibroblastic and epithelial cells. J Biol Chem. 1994;269(9):6271-4.

122. Shimo T, Nakanishi T, Nishida T, Asano M, Sasaki A, Kanyama M, et al. Involvement of CTGF, a hypertrophic chondrocyte-specific gene product, in tumor angiogenesis. Oncology. 2001;61(4):315-22.

123. de Jong JS, van Diest PJ, van der Valk P, Baak JP. Expression of growth factors, growth-inhibiting factors, and their receptors in invasive breast cancer. II: Correlations with proliferation and angiogenesis. The Journal of pathology. 1998;184(1):53-7.

124. Hasegawa Y, Takanashi S, Kanehira Y, Tsushima T, Imai T, Okumura K. Transforming growth factor-beta1 level correlates with angiogenesis, tumor progression, and prognosis in patients with nonsmall cell lung carcinoma. Cancer. 2001;91(5):964-71.

125. Letterio JJ, Roberts AB. Regulation of immune responses by TGF-beta. Annual review of immunology. 1998;16:137-61.

126. Valderrama-Carvajal H, Cocolakis E, Lacerte A, Lee EH, Krystal G, Ali S, et al. Activin/TGF-beta induce apoptosis through Smad-dependent expression of the lipid phosphatase SHIP. Nat Cell Biol. 2002;4(12):963-9.

127. Ranges GE, Figari IS, Espevik T, Palladino MA, Jr. Inhibition of cytotoxic T cell development by transforming growth factor beta and reversal by recombinant tumor necrosis factor alpha. The Journal of experimental medicine. 1987;166(4):991-8.

128. Chaouchi N, Arvanitakis L, Auffredou MT, Blanchard DA, Vazquez A, Sharma S. Characterization of transforming growth factor-beta 1 induced apoptosis in normal human B cells and lymphoma B cell lines. Oncogene. 1995;11(8):1615-22.

129. Ahmadzadeh M, Rosenberg SA. TGF-beta 1 attenuates the acquisition and expression of effector function by tumor antigen-specific human memory CD8 T cells. J Immunol. 2005;174(9):5215-23.

130. Thomas DA, Massague J. TGF-beta directly targets cytotoxic T cell functions during tumor evasion of immune surveillance. Cancer cell. 2005;8(5):369-80.

131. Ojeda-Fernandez L, Recio-Poveda L, Aristorena M, Lastres P, Blanco FJ, Sanz-Rodriguez F, et al. Mice Lacking Endoglin in Macrophages Show an Impaired Immune Response. PLoS Genet. 2016;12(3):e1005935.

132. Che J, Yang Y, Xiao J, Zhao P, Yan B, Dong S, et al. Decreased expression of claudin-3 is associated with a poor prognosis and EMT in completely resected squamous cell lung carcinoma. Tumour biology : the journal of the International Society for Oncodevelopmental Biology and Medicine. 2015;36(8):6559-68.

133. Shintani Y, Okimura A, Sato K, Nakagiri T, Kadota Y, Inoue M, et al. Epithelial to mesenchymal transition is a determinant of sensitivity to chemoradiotherapy in non-small cell lung cancer. Ann Thorac Surg. 2011;92(5):1794-804; discussion 804.

134. Yauch RL, Januario T, Eberhard DA, Cavet G, Zhu W, Fu L, et al. Epithelial versus mesenchymal phenotype determines in vitro sensitivity and predicts clinical activity of erlotinib in lung cancer patients. Clin Cancer Res. 2005;11(24 Pt 1):8686-98.

135. Yao Z, Fenoglio S, Gao DC, Camiolo M, Stiles B, Lindsted T, et al. TGF-beta IL-6 axis mediates selective and adaptive mechanisms of resistance to molecular targeted therapy in lung cancer. Proc Natl Acad Sci U S A. 2010;107(35):15535-40.

136. Buck E, Eyzaguirre A, Barr S, Thompson S, Sennello R, Young D, et al. Loss of homotypic cell adhesion by epithelial-mesenchymal transition or mutation limits sensitivity to epidermal growth factor receptor inhibition. Molecular cancer therapeutics. 2007;6(2):532-41.

137. Black PC, Brown GA, Inamoto T, Shrader M, Arora A, Siefker-Radtke AO, et al. Sensitivity to epidermal growth factor receptor inhibitor requires E-cadherin expression in urothelial carcinoma cells. Clin Cancer Res. 2008;14(5):1478-86.

138. Frederick BA, Helfrich BA, Coldren CD, Zheng D, Chan D, Bunn PA, Jr., et al. Epithelial to mesenchymal transition predicts gefitinib resistance in cell lines of head and neck squamous cell carcinoma and non-small cell lung carcinoma. Molecular cancer therapeutics. 2007;6(6):1683-91.

139. Kemper K, de Goeje PL, Peeper DS, van Amerongen R. Phenotype switching: tumor cell plasticity as a resistance mechanism and target for therapy. Cancer Res. 2014;74(21):5937-41.

140. Zheng X, Carstens JL, Kim J, Scheible M, Kaye J, Sugimoto H, et al. Epithelial-to-mesenchymal transition is dispensable for metastasis but induces chemoresistance in pancreatic cancer. Nature. 2015;527(7579):525-30.

141. Huang S, Holzel M, Knijnenburg T, Schlicker A, Roepman P, McDermott U, et al. MED12 controls the response to multiple cancer drugs through regulation of TGF-beta receptor signaling. Cell. 2012;151(5):937-50.

142. Shull MM, Ormsby I, Kier AB, Pawlowski S, Diebold RJ, Yin M, et al. Targeted disruption of the mouse transforming growth factor-beta 1 gene results in multifocal inflammatory disease. Nature. 1992;359(6397):693-9.

143. Dickson MC, Martin JS, Cousins FM, Kulkarni AB, Karlsson S, Akhurst RJ. Defective haematopoiesis and vasculogenesis in transforming growth factor-beta 1 knock out mice. Development. 1995;121(6):1845-54.

144. Bragado P, Estrada Y, Parikh F, Krause S, Capobianco C, Farina HG, et al. TGF-beta2 dictates disseminated tumour cell fate in target organs through TGF-beta-RIII and p38alpha/beta signalling. Nat Cell Biol. 2013;15(11):1351-61.

145. Laping NJ, Everitt JI, Frazier KS, Burgert M, Portis MJ, Cadacio C, et al. Tumor-specific efficacy of transforming growth factor-beta RI inhibition in Eker rats. Clin Cancer Res. 2007;13(10):3087-99.

146. Spain L, Diem S, Larkin J. Management of toxicities of immune checkpoint inhibitors. Cancer treatment reviews. 2016;44:51-60.

147. Cohn A, Lahn MM, Williams KE, Cleverly AL, Pitou C, Kadam SK, et al. A phase I dose-escalation study to a predefined dose of a transforming growth factor-beta1 monoclonal antibody (TbetaM1) in patients with metastatic cancer. Int J Oncol. 2014;45(6):2221-31.

148. Morris JC, Tan AR, Olencki TE, Shapiro GI, Dezube BJ, Reiss M, et al. Phase I study of GC1008 (fresolimumab): a human anti-transforming growth factor-beta (TGFbeta) monoclonal antibody in patients with advanced malignant melanoma or renal cell carcinoma. PLoS One. 2014;9(3):e90353.

149. Van der Jeught K, Joe PT, Bialkowski L, Heirman C, Daszkiewicz L, Liechtenstein T, et al. Intratumoral administration of mRNA encoding a fusokine consisting of IFN-beta and the ectodomain of the TGF-beta receptor II potentiates antitumor immunity. Oncotarget. 2014;5(20):10100-13.

150. Triplett TA, Tucker CG, Triplett KC, Alderman Z, Sun L, Ling LE, et al. STAT3 Signaling Is Required for Optimal Regression of Large Established Tumors in Mice Treated with Anti-OX40 and TGFbeta Receptor Blockade. Cancer immunology research. 2015;3(5):526-35.

151. Gueorguieva I, Cleverly AL, Stauber A, Sada Pillay N, Rodon JA, Miles CP, et al. Defining a therapeutic window for the novel TGF-beta inhibitor LY2157299 monohydrate based on a pharmacokinetic/pharmacodynamic model. Br J Clin Pharmacol. 2014;77(5):796-807.

152. Kawasaki K, Freimuth J, Meyer DS, Lee MM, Tochimoto-Okamoto A, Benzinou M, et al. Genetic variants of Adam17 differentially regulate TGFbeta signaling to modify vascular pathology in mice and humans. Proc Natl Acad Sci U S A. 2014;111(21):7723-8.

153. Prudkin L, Liu DD, Ozburn NC, Sun M, Behrens C, Tang X, et al. Epithelial-to-mesenchymal transition in the development and progression of adenocarcinoma and squamous cell carcinoma of the lung. Modern pathology : an official journal of the United States and Canadian Academy of Pathology, Inc. 2009;22(5):668-78.

154. Barthelemy-Brichant N, David JL, Bosquee L, Bury T, Seidel L, Albert A, et al. Increased TGFbeta1 plasma level in patients with lung cancer: potential mechanisms. Eur J Clin Invest. 2002;32(3):193-8.

155. Hou YL, Chen H, Dong ZH, Xue CJ, Wu YF, Luo HX, et al. Clinical significance of serum transforming growth factor-beta1 in lung cancer. Cancer epidemiology. 2013;37(5):750-3.

156. Maeng YI, Kim KH, Kim JY, Lee SJ, Sung WJ, Lee CK, et al. Transcription factors related to epithelial mesenchymal transition in tumor center and margin in invasive lung adenocarcinoma. Int J Clin Exp Pathol. 2014;7(7):4095-103.

157. Dohadwala M, Yang SC, Luo J, Sharma S, Batra RK, Huang M, et al. Cyclooxygenase-2-dependent regulation of E-cadherin: prostaglandin E(2) induces transcriptional repressors ZEB1 and snail in non-small cell lung cancer. Cancer Res. 2006;66(10):5338-45.

158. Gemmill RM, Roche J, Potiron VA, Nasarre P, Mitas M, Coldren CD, et al. ZEB1-responsive genes in non-small cell lung cancer. Cancer letters. 2011;300(1):66-78.

159. Hung JJ, Yang MH, Hsu HS, Hsu WH, Liu JS, Wu KJ. Prognostic significance of hypoxia-inducible factor-1alpha, TWIST1 and Snail expression in resectable non-small cell lung cancer. Thorax. 2009;64(12):1082-9.

160. Zeng J, Zhan P, Wu G, Yang W, Liang W, Lv T, et al. Prognostic value of Twist in lung cancer: systematic review and meta-analysis. Translational lung cancer research. 2015;4(3):236-41.

161. Jiang W, Pang XG, Wang Q, Shen YX, Chen XK, Xi JJ. Prognostic role of Twist, Slug, and Foxc2 expression in stage I non-small-cell lung cancer after curative resection. Clin Lung Cancer. 2012;13(4):280-7.

162. Dauphin M, Barbe C, Lemaire S, Nawrocki-Raby B, Lagonotte E, Delepine G, et al. Vimentin expression predicts the occurrence of metastases in non small cell lung carcinomas. Lung Cancer. 2013;81(1):117-22.

163. Al-Saad S, Al-Shibli K, Donnem T, Persson M, Bremnes RM, Busund LT. The prognostic impact of NF-kappaB p105, vimentin, E-cadherin and Par6 expression in epithelial and stromal compartment in non-small-cell lung cancer. Br J Cancer. 2008;99(9):1476-83.

164. Gong L, Wu D, Zou J, Chen J, Chen L, Chen Y, et al. Prognostic impact of serum and tissue MMP-9 in non-small cell lung cancer: a systematic review and meta-analysis. Oncotarget. 2016;7(14):18458-68.

165. Osada H, Tatematsu Y, Masuda A, Saito T, Sugiyama M, Yanagisawa K, et al. Heterogeneous transforming growth factor (TGF)-beta unresponsiveness and loss of TGF-beta receptor type II expression caused by histone deacetylation in lung cancer cell lines. Cancer Res. 2001;61(22):8331-9.

166. Hougaard S, Norgaard P, Abrahamsen N, Moses HL, Spang-Thomsen M, Skovgaard Poulsen H. Inactivation of the transforming growth factor beta type II receptor in human small cell lung cancer cell lines. Br J Cancer. 1999;79(7-8):1005-11.

167. Anumanthan G, Halder SK, Osada H, Takahashi T, Massion PP, Carbone DP, et al. Restoration of TGF-beta signalling reduces tumorigenicity in human lung cancer cells. Br J Cancer. 2005;93(10):1157-67.

168. Malkoski SP, Haeger SM, Cleaver TG, Rodriguez KJ, Li H, Lu SL, et al. Loss of transforming growth factor beta type II receptor increases aggressive tumor behavior and reduces survival in lung adenocarcinoma and squamous cell carcinoma. Clin Cancer Res. 2012;18(8):2173-83.

169. de Jonge RR, Garrigue-Antar L, Vellucci VF, Reiss M. Frequent inactivation of the transforming growth factor beta type II receptor in small-cell lung carcinoma cells. Oncology research. 1997;9(2):89-98.

170. Borczuk AC, Papanikolaou N, Toonkel RL, Sole M, Gorenstein LA, Ginsburg ME, et al. Lung adenocarcinoma invasion in TGFbetaRII-deficient cells is mediated by CCL5/RANTES. Oncogene. 2008;27(4):557-64.

171. Borczuk AC, Kim HK, Yegen HA, Friedman RA, Powell CA. Lung adenocarcinoma global profiling identifies type II transforming growth factor-beta receptor as a repressor of invasiveness. American journal of respiratory and critical care medicine. 2005;172(6):729-37.

172. Kitano H. Systems biology: a brief overview. Science. 2002;295(5560):1662-4.

173. Wolkenhauer O, Mesarovic M. Feedback dynamics and cell function: Why systems biology is called Systems Biology. Molecular bioSystems. 2005;1(1):14-6.

174. Bruggeman FJ, Westerhoff HV. The nature of systems biology. Trends in microbiology. 2007;15(1):45-50.

175. Bornholdt S. Systems biology. Less is more in modeling large genetic networks. Science. 2005;310(5747):449-51.

176. Edda Klipp WL, Christoph Wierling, Axel Kowald Systems Biology: A Textbook. 2nd ed: Wiley-VCH; 2016.

177. Kitano H. Computational systems biology. Nature. 2002;420(6912):206-10.

178. Vilar JM, Jansen R, Sander C. Signal processing in the TGF-beta superfamily ligand-receptor network. PLoS Comput Biol. 2006;2(1):e3.

179. Zi Z, Klipp E. Constraint-based modeling and kinetic analysis of the Smad dependent TGF-beta signaling pathway. PLoS One. 2007;2(9):e936.

180. Mitchell H, Choudhury A, Pagano RE, Leof EB. Ligand-dependent and -independent transforming growth factor-beta receptor recycling regulated by clathrin-mediated endocytosis and Rab11. Mol Biol Cell. 2004;15(9):4166-78.

181. Clarke DC, Betterton MD, Liu X. Systems theory of Smad signalling. Systems biology. 2006;153(6):412-24.

182. Schmierer B, Hill CS. Kinetic analysis of Smad nucleocytoplasmic shuttling reveals a mechanism for transforming growth factor beta-dependent nuclear accumulation of Smads. Mol Cell Biol. 2005;25(22):9845-58.

183. Inman GJ, Nicolas FJ, Hill CS. Nucleocytoplasmic shuttling of Smads 2, 3, and 4 permits sensing of TGF-beta receptor activity. Mol Cell. 2002;10(2):283-94.

184. Clarke DC, Brown ML, Erickson RA, Shi Y, Liu X. Transforming growth factor beta depletion is the primary determinant of Smad signaling kinetics. Mol Cell Biol. 2009;29(9):2443-55.

185. Vizan P, Miller DS, Gori I, Das D, Schmierer B, Hill CS. Controlling long-term signaling: receptor dynamics determine attenuation and refractory behavior of the TGF-beta pathway. Science signaling. 2013;6(305):ra106.

186. Khatibi S, Zhu HJ, Wagner J, Tan CW, Manton JH, Burgess AW. Mathematical model of TGF-betasignalling: feedback coupling is consistent with signal switching. BMC systems biology. 2017;11(1):48.

187. Zi Z, Feng Z, Chapnick DA, Dahl M, Deng D, Klipp E, et al. Quantitative analysis of transient and sustained transforming growth factor-beta signaling dynamics. Mol Syst Biol. 2011;7:492.

188. Zhang J, Tian XJ, Zhang H, Teng Y, Li R, Bai F, et al. TGF-beta-induced epithelial-to-mesenchymal transition proceeds through stepwise activation of multiple feedback loops. Science signaling. 2014;7(345):ra91.

189. Marwitz S, Depner S, Dvornikov D, Merkle R, Szczygiel M, Muller-Decker K, et al. Downregulation of the TGFbeta Pseudoreceptor BAMBI in Non-Small Cell Lung Cancer Enhances TGFbeta Signaling and Invasion. Cancer Res. 2016;76(13):3785-801.

190. Lin C, Song H, Huang C, Yao E, Gacayan R, Xu SM, et al. Alveolar type II cells possess the capability of initiating lung tumor development. PLoS One. 2012;7(12):e53817.

191. Borok Z, Crandall ED. More life for a "terminal" cell. Am J Physiol Lung Cell Mol Physiol. 2009;297(6):L1042-4.

192. Gronroos E, Hellman U, Heldin CH, Ericsson J. Control of Smad7 stability by competition between acetylation and ubiquitination. Mol Cell. 2002;10(3):483-93.

193. Gruber T, Hinterleitner R, Hermann-Kleiter N, Meisel M, Kleiter I, Wang CM, et al. Cbl-b mediates TGFbeta sensitivity by downregulating inhibitory SMAD7 in primary T cells. Journal of molecular cell biology. 2013;5(6):358-68.

194. Schliekelman MJ, Taguchi A, Zhu J, Dai X, Rodriguez J, Celiktas M, et al. Molecular portraits of epithelial, mesenchymal, and hybrid States in lung adenocarcinoma and their relevance to survival. Cancer Res. 2015;75(9):1789-800.

195. Rooney M, Devarakonda S, Govindan R. Genomics of squamous cell lung cancer. The oncologist. 2013;18(6):707-16.

196. Quail DF, Joyce JA. Microenvironmental regulation of tumor progression and metastasis. Nat Med. 2013;19(11):1423-37.

197. Sterlacci W, Wolf D, Savic S, Hilbe W, Schmid T, Jamnig H, et al. High transforming growth factor beta expression represents an important prognostic parameter for surgically resected non-small cell lung cancer. Human pathology. 2012;43(3):339-49.

198. Arumugam T, Ramachandran V, Fournier KF, Wang H, Marquis L, Abbruzzese JL, et al. Epithelial to mesenchymal transition contributes to drug resistance in pancreatic cancer. Cancer Res. 2009;69(14):5820-8.

199. Supek F, Bosnjak M, Skunca N, Smuc T. REVIGO summarizes and visualizes long lists of gene ontology terms. PLoS One. 2011;6(7):e21800.

200. Makowska KA, Hughes RE, White KJ, Wells CM, Peckham M. Specific Myosins Control Actin Organization, Cell Morphology, and Migration in Prostate Cancer Cells. Cell reports. 2015;13(10):2118-25.

201. Ruiz de Garibay G, Herranz C, Llorente A, Boni J, Serra-Musach J, Mateo F, et al. Lymphangioleiomyomatosis Biomarkers Linked to Lung Metastatic Potential and Cell Stemness. PLoS One. 2015;10(7):e0132546.

202. Lauden L, Siewiera J, Boukouaci W, Ramgolam K, Mourah S, Lebbe C, et al. TGF-beta-induced (TGFBI) protein in melanoma: a signature of high metastatic potential. The Journal of investigative dermatology. 2014;134(6):1675-85.

203. Look MP, van Putten WL, Duffy MJ, Harbeck N, Christensen IJ, Thomssen C, et al. Pooled analysis of prognostic impact of urokinase-type plasminogen activator and its inhibitor PAI-1 in 8377 breast cancer patients. J Natl Cancer Inst. 2002;94(2):116-28.

204. Haider S, Wang J, Nagano A, Desai A, Arumugam P, Dumartin L, et al. A multi-gene signature predicts outcome in patients with pancreatic ductal adenocarcinoma. Genome medicine. 2014;6(12):105.

205. Chen CH, Fong LW, Yu E, Wu R, Trott JF, Weiss RH. Upregulation of MARCKS in kidney cancer and its potential as a therapeutic target. Oncogene. 2017.

206. Hallett RM, Dvorkin-Gheva A, Bane A, Hassell JA. A gene signature for predicting outcome in patients with basal-like breast cancer. Sci Rep. 2012;2:227.

207. Katono K, Sato Y, Jiang SX, Kobayashi M, Nagashio R, Ryuge S, et al. Prognostic significance of MYH9 expression in resected non-small cell lung cancer. PLoS One. 2015;10(3):e0121460.

208. Ouderkirk JL, Krendel M. Non-muscle myosins in tumor progression, cancer cell invasion, and metastasis. Cytoskeleton (Hoboken). 2014;71(8):447-63.

209. Soltermann A, Tischler V, Arbogast S, Braun J, Probst-Hensch N, Weder W, et al. Prognostic significance of epithelial-mesenchymal and mesenchymal-epithelial transition protein expression in non-small cell lung cancer. Clin Cancer Res. 2008;14(22):7430-7.

210. von der Heyde S, Sonntag J, Kaschek D, Bender C, Bues J, Wachter A, et al. RPPanalyzer toolbox: an improved R package for analysis of reverse phase protein array data. BioTechniques. 2014;57(3):125-35.

211. Alarcon C, Zaromytidou AI, Xi Q, Gao S, Yu J, Fujisawa S, et al. Nuclear CDKs drive Smad transcriptional activation and turnover in BMP and TGF-beta pathways. Cell. 2009;139(4):757-69.

212. Wotton D, Massague J. Smad transcriptional corepressors in TGF beta family signaling. Current topics in microbiology and immunology. 2001;254:145-64.

213. Wan Y, Liu X, Kirschner MW. The anaphase-promoting complex mediates TGF-beta signaling by targeting SnoN for destruction. Mol Cell. 2001;8(5):1027-39.

214. Sun Y, Liu X, Ng-Eaton E, Lodish HF, Weinberg RA. SnoN and Ski protooncoproteins are rapidly degraded in response to transforming growth factor beta signaling. Proc Natl Acad Sci U S A. 1999;96(22):12442-7.

215. Lo RS, Massague J. Ubiquitin-dependent degradation of TGF-beta-activated smad2. Nat Cell Biol. 1999;1(8):472-8.

216. Lin X, Liang M, Feng XH. Smurf2 is a ubiquitin E3 ligase mediating proteasome-dependent degradation of Smad2 in transforming growth factor-beta signaling. J Biol Chem. 2000;275(47):36818-22.

217. Chacko BM, Qin B, Correia JJ, Lam SS, de Caestecker MP, Lin K. The L3 loop and C-terminal phosphorylation jointly define Smad protein trimerization. Nature structural biology. 2001;8(3):248-53.

218. Inman GJ, Hill CS. Stoichiometry of active smad-transcription factor complexes on DNA. J Biol Chem. 2002;277(52):51008-16.

219. Xiao Z, Latek R, Lodish HF. An extended bipartite nuclear localization signal in Smad4 is required for its nuclear import and transcriptional activity. Oncogene. 2003;22(7):1057-69.

220. Xiao Z, Liu X, Lodish HF. Importin beta mediates nuclear translocation of Smad 3. J Biol Chem. 2000;275(31):23425-8.

221. Kurisaki A, Kurisaki K, Kowanetz M, Sugino H, Yoneda Y, Heldin CH, et al. The mechanism of nuclear export of Smad3 involves exportin 4 and Ran. Mol Cell Biol. 2006;26(4):1318-32.

222. Prunier C, Pessah M, Ferrand N, Seo SR, Howe P, Atfi A. The oncoprotein Ski acts as an antagonist of transforming growth factor-beta signaling by suppressing Smad2 phosphorylation. J Biol Chem. 2003;278(28):26249-57.

223. Sobell HM. Actinomycin and DNA transcription. Proc Natl Acad Sci U S A. 1985;82(16):5328-31.

224. Schneider-Poetsch T, Ju J, Eyler DE, Dang Y, Bhat S, Merrick WC, et al. Inhibition of eukaryotic translation elongation by cycloheximide and lactimidomycin. Nature chemical biology. 2010;6(3):209-17.

225. Rock KL, Gramm C, Rothstein L, Clark K, Stein R, Dick L, et al. Inhibitors of the proteasome block the degradation of most cell proteins and the generation of peptides presented on MHC class I molecules. Cell. 1994;78(5):761-71.

226. Adlung L, Kar S, Wagner MC, She B, Chakraborty S, Bao J, et al. Protein abundance of AKT and ERK pathway components governs cell type-specific regulation of proliferation. Mol Syst Biol. 2017;13(1):904.

227. Herhaus L, Sapkota GP. The emerging roles of deubiquitylating enzymes (DUBs) in the TGFbeta and BMP pathways. Cell Signal. 2014;26(10):2186-92.

228. Bray NL, Pimentel H, Melsted P, Pachter L. Near-optimal probabilistic RNA-seq quantification. Nature biotechnology. 2016;34(5):525-7.

229. Soneson C, Love MI, Robinson MD. Differential analyses for RNA-seq: transcript-level estimates improve gene-level inferences. F1000Research. 2015;4:1521.

230. Durinck S, Spellman PT, Birney E, Huber W. Mapping identifiers for the integration of genomic datasets with the R/Bioconductor package biomaRt. Nature protocols. 2009;4(8):1184-91.

231. Raue A, Kreutz C, Maiwald T, Bachmann J, Schilling M, Klingmuller U, et al. Structural and practical identifiability analysis of partially observed dynamical models by exploiting the profile likelihood. Bioinformatics. 2009;25(15):1923-9.

232. Chis OT, Banga JR, Balsa-Canto E. Structural identifiability of systems biology models: a critical comparison of methods. PLoS One. 2011;6(11):e27755.

233. Hayashi H, Abdollah S, Qiu Y, Cai J, Xu YY, Grinnell BW, et al. The MAD-related protein Smad7 associates with the TGFbeta receptor and functions as an antagonist of TGFbeta signaling. Cell. 1997;89(7):1165-73.

234. Bauge C, Cauvard O, Leclercq S, Galera P, Boumediene K. Modulation of transforming growth factor beta signalling pathway genes by transforming growth factor beta in human osteoarthritic chondrocytes: involvement of Sp1 in both early and late response cells to transforming growth factor beta. Arthritis research & therapy. 2011;13(1):R23.

235. Moustakas A, Heldin CH. Non-Smad TGF-beta signals. J Cell Sci. 2005;118(Pt 16):3573-84.

236. Wakefield LM, Smith DM, Masui T, Harris CC, Sporn MB. Distribution and modulation of the cellular receptor for transforming growth factor-beta. J Cell Biol. 1987;105(2):965-75.

237. Hata A, Chen YG. TGF-beta Signaling from Receptors to Smads. Cold Spring Harbor perspectives in biology. 2016.

238. Aebersold R, Mann M. Mass-spectrometric exploration of proteome structure and function. Nature. 2016;537(7620):347-55.

239. Bourmaud A, Gallien S, Domon B. Parallel reaction monitoring using quadrupole-Orbitrap mass spectrometer: Principle and applications. Proteomics. 2016;16(15-16):2146-59.

240. Tao WA, Aebersold R. Advances in quantitative proteomics via stable isotope tagging and mass spectrometry. Current opinion in biotechnology. 2003;14(1):110-8.

241. Rappsilber J, Mann M, Ishihama Y. Protocol for micro-purification, enrichment, pre-fractionation and storage of peptides for proteomics using StageTips. Nature protocols. 2007;2(8):1896-906.

242. MacLean B, Tomazela DM, Shulman N, Chambers M, Finney GL, Frewen B, et al. Skyline: an open source document editor for creating and analyzing targeted proteomics experiments. Bioinformatics. 2010;26(7):966-8.

243. Massague J. TGFbeta in Cancer. Cell. 2008;134(2):215-30.

244. Saji H, Nakamura H, Awut I, Kawasaki N, Hagiwara M, Ogata A, et al. Significance of expression of TGF-beta in pulmonary metastasis in non-small cell lung cancer tissues. Ann Thorac Cardiovasc Surg. 2003;9(5):295-300.

245. Grady WM, Willis JE, Trobridge P, Romero-Gallo J, Munoz N, Olechnowicz J, et al. Proliferation and Cdk4 expression in microsatellite unstable colon cancers with TGFBR2 mutations. Int J Cancer. 2006;118(3):600-8.

246. Uchida K, Nagatake M, Osada H, Yatabe Y, Kondo M, Mitsudomi T, et al. Somatic in vivo alterations of the JV18-1 gene at 18q21 in human lung cancers. Cancer Res. 1996;56(24):5583-5.

247. Nagatake M, Takagi Y, Osada H, Uchida K, Mitsudomi T, Saji S, et al. Somatic in vivo alterations of the DPC4 gene at 18q21 in human lung cancers. Cancer Res. 1996;56(12):2718-20.

248. Sekiya T, Adachi S, Kohu K, Yamada T, Higuchi O, Furukawa Y, et al. Identification of BMP and activin membrane-bound inhibitor (BAMBI), an inhibitor of transforming growth factor-beta signaling, as a target of the beta-catenin pathway in colorectal tumor cells. J Biol Chem. 2004;279(8):6840-6.

249. Togo N, Ohwada S, Sakurai S, Toya H, Sakamoto I, Yamada T, et al. Prognostic significance of BMP and activin membrane-bound inhibitor in colorectal cancer. World journal of gastroenterology. 2008;14(31):4880-8.

250. Pils D, Wittinger M, Petz M, Gugerell A, Gregor W, Alfanz A, et al. BAMBI is overexpressed in ovarian cancer and co-translocates with Smads into the nucleus upon TGF-beta treatment. Gynecol Oncol. 2010;117(2):189-97.

251. Khin SS, Kitazawa R, Win N, Aye TT, Mori K, Kondo T, et al. BAMBI gene is epigenetically silenced in subset of high-grade bladder cancer. Int J Cancer. 2009;125(2):328-38.

252. Degen WG, Weterman MA, van Groningen JJ, Cornelissen IM, Lemmers JP, Agterbos MA, et al. Expression of nma, a novel gene, inversely correlates with the metastatic potential of human melanoma cell lines and xenografts. Int J Cancer. 1996;65(4):460-5.

253. Lang DS, Marwitz S, Heilenkotter U, Schumm W, Behrens O, Simon R, et al. Transforming growth factor-beta signaling leads to uPA/PAI-1 activation and metastasis: a study on human breast cancer tissues. Pathology oncology research : POR. 2014;20(3):727-32.

254. Flavahan WA, Gaskell E, Bernstein BE. Epigenetic plasticity and the hallmarks of cancer. Science. 2017;357(6348).

255. Kim KH, Roberts CW. Targeting EZH2 in cancer. Nat Med. 2016;22(2):128-34.

256. Hodges C, Kirkland JG, Crabtree GR. The Many Roles of BAF (mSWI/SNF) and PBAF Complexes in Cancer. Cold Spring Harbor perspectives in medicine. 2016;6(8).

257. Audergon PN, Catania S, Kagansky A, Tong P, Shukla M, Pidoux AL, et al. Epigenetics. Restricted epigenetic inheritance of H3K9 methylation. Science. 2015;348(6230):132-5.

258. Altman BJ, Stine ZE, Dang CV. From Krebs to clinic: glutamine metabolism to cancer therapy. Nat Rev Cancer. 2016;16(12):773.

259. Taube JH, Herschkowitz JI, Komurov K, Zhou AY, Gupta S, Yang J, et al. Core epithelial-to-mesenchymal transition interactome gene-expression signature is associated with claudin-low and metaplastic breast cancer subtypes. Proc Natl Acad Sci U S A. 2010;107(35):15449-54.

260. Ohashi S, Natsuizaka M, Wong GS, Michaylira CZ, Grugan KD, Stairs DB, et al. Epidermal growth factor receptor and mutant p53 expand an esophageal cellular subpopulation capable of epithelial-to-mesenchymal transition through ZEB transcription factors. Cancer Res. 2010;70(10):4174-84.

261. Pirozzi G, Tirino V, Camerlingo R, Franco R, La Rocca A, Liguori E, et al. Epithelial to mesenchymal transition by TGFbeta-1 induction increases stemness characteristics in primary non small cell lung cancer cell line. PLoS One. 2011;6(6):e21548.

262. Pegoraro S, Ros G, Piazza S, Sommaggio R, Ciani Y, Rosato A, et al. HMGA1 promotes metastatic processes in basal-like breast cancer regulating EMT and stemness. Oncotarget. 2013;4(8):1293-308.

263. Alonso SR, Tracey L, Ortiz P, Perez-Gomez B, Palacios J, Pollan M, et al. A high-throughput study in melanoma identifies epithelial-mesenchymal transition as a major determinant of metastasis. Cancer Res. 2007;67(7):3450-60.

264. Debnath J, Brugge JS. Modelling glandular epithelial cancers in three-dimensional cultures. Nat Rev Cancer. 2005;5(9):675-88.

265. Latifi A, Abubaker K, Castrechini N, Ward AC, Liongue C, Dobill F, et al. Cisplatin treatment of primary and metastatic epithelial ovarian carcinomas generates residual cells with mesenchymal stem cell-like profile. J Cell Biochem. 2011;112(10):2850-64.

266. Toge M, Yokoyama S, Kato S, Sakurai H, Senda K, Doki Y, et al. Critical contribution of MCL-1 in EMT-associated chemo-resistance in A549 non-small cell lung cancer. Int J Oncol. 2015;46(4):1844-8.

267. Biswas S, Guix M, Rinehart C, Dugger TC, Chytil A, Moses HL, et al. Inhibition of TGF-beta with neutralizing antibodies prevents radiation-induced acceleration of metastatic cancer progression. J Clin Invest. 2007;117(5):1305-13.

268. Bedi A, Chang X, Noonan K, Pham V, Bedi R, Fertig EJ, et al. Inhibition of TGF-beta enhances the in vivo antitumor efficacy of EGF receptor-targeted therapy. Molecular cancer therapeutics. 2012;11(11):2429-39.

269. Vrba L, Jensen TJ, Garbe JC, Heimark RL, Cress AE, Dickinson S, et al. Role for DNA methylation in the regulation of miR-200c and miR-141 expression in normal and cancer cells. PLoS One. 2010;5(1):e8697.

270. Eades G, Yao Y, Yang M, Zhang Y, Chumsri S, Zhou Q. miR-200a regulates SIRT1 expression and epithelial to mesenchymal transition (EMT)-like transformation in mammary epithelial cells. J Biol Chem. 2011;286(29):25992-6002.

271. Shaker S, Bernstein M, Momparler LF, Momparler RL. Preclinical evaluation of antineoplastic activity of inhibitors of DNA methylation (5-aza-2'-deoxycytidine) and histone deacetylation (trichostatin A, depsipeptide) in combination against myeloid leukemic cells. Leukemia research. 2003;27(5):437-44.

272. Petti MC, Fazi F, Gentile M, Diverio D, De Fabritiis P, De Propris MS, et al. Complete remission through blast cell differentiation in PLZF/RARalpha-positive acute promyelocytic leukemia: in vitro and in vivo studies. Blood. 2002;100(3):1065-7.

273. Huang AL, Liu SG, Qi WJ, Zhao YF, Li YM, Lei B, et al. TGF-beta1 protein expression in non-small cell lung cancers is correlated with prognosis. Asian Pacific journal of cancer prevention : APJCP. 2014;15(19):8143-7.

274. Levayer R, Lecuit T. Breaking down EMT. Nat Cell Biol. 2008;10(7):757-9.

275. Yilmaz M, Christofori G. EMT, the cytoskeleton, and cancer cell invasion. Cancer Metastasis Rev. 2009;28(1-2):15-33.

276. Hashimoto Y, Ito T, Inoue H, Okumura T, Tanaka E, Tsunoda S, et al. Prognostic significance of fascin overexpression in human esophageal squamous cell carcinoma. Clin Cancer Res. 2005;11(7):2597-605.

277. Yoder BJ, Tso E, Skacel M, Pettay J, Tarr S, Budd T, et al. The expression of fascin, an actin-bundling motility protein, correlates with hormone receptor-negative breast cancer and a more aggressive clinical course. Clin Cancer Res. 2005;11(1):186-92.

278. Arjonen A, Kaukonen R, Mattila E, Rouhi P, Hognas G, Sihto H, et al. Mutant p53-associated myosin-X upregulation promotes breast cancer invasion and metastasis. J Clin Invest. 2014;124(3):1069-82.

279. Xia ZK, Yuan YC, Yin N, Yin BL, Tan ZP, Hu YR. Nonmuscle myosin IIA is associated with poor prognosis of esophageal squamous cancer. Diseases of the esophagus : official journal of the International Society for Diseases of the Esophagus. 2012;25(5):427-36.

280. Ouderkirk JL, Krendel M. Myosin 1e is a component of the invadosome core that contributes to regulation of invadosome dynamics. Exp Cell Res. 2014;322(2):265-76.

281. Murphy DA, Courtneidge SA. The 'ins' and 'outs' of podosomes and invadopodia: characteristics, formation and function. Nat Rev Mol Cell Biol. 2011;12(7):413-26.

282. Cao R, Chen J, Zhang X, Zhai Y, Qing X, Xing W, et al. Elevated expression of myosin X in tumours contributes to breast cancer aggressiveness and metastasis. Br J Cancer. 2014;111(3):539-50.

283. Xiong D, Ye YL, Chen MK, Qin ZK, Li MZ, Zhang H, et al. Non-muscle myosin II is an independent predictor of overall survival for cystectomy candidates with early-stage bladder cancer. Oncology reports. 2012;28(5):1625-32.

284. Acharyya S, Oskarsson T, Vanharanta S, Malladi S, Kim J, Morris PG, et al. A CXCL1 paracrine network links cancer chemoresistance and metastasis. Cell. 2012;150(1):165-78.

285. Wei Y, Hu G, Kang Y. Metadherin as a link between metastasis and chemoresistance. Cell Cycle. 2009;8(14):2132-3.

286. Xu J, Yue CF, Zhou WH, Qian YM, Zhang Y, Wang SW, et al. Aurora-A contributes to cisplatin resistance and lymphatic metastasis in non-small cell lung cancer and predicts poor prognosis. Journal of translational medicine. 2014;12:200.

287. Kiel C, Verschueren E, Yang JS, Serrano L. Integration of protein abundance and structure data reveals competition in the ErbB signaling network. Sci Signal. 2013;6(306):ra109.

288. Kim SG, Kim HA, Jong HS, Park JH, Kim NK, Hong SH, et al. The endogenous ratio of Smad2 and Smad3 influences the cytostatic function of Smad3. Mol Biol Cell. 2005;16(10):4672-83.

289. PJ N. Dynamic Modeling of Negative Feedback Regulation of TGFbeta-Smad Signaling in Primary Mouse Hepatocytes: University Heidelberg; 2008.

290. Lucarelli P. Dynamic modeling of TGFb-induced Smad complex formation and negative regulators in primary hepatocytes and hepatocarcinoma cell lines: Ruperto Carola University of Heidelberg; 2015.

291. Brown KA, Pietenpol JA, Moses HL. A tale of two proteins: differential roles and regulation of Smad2 and Smad3 in TGF-beta signaling. J Cell Biochem. 2007;101(1):9-33.

292. Goumans MJ, Valdimarsdottir G, Itoh S, Rosendahl A, Sideras P, ten Dijke P. Balancing the activation state of the endothelium via two distinct TGF-beta type I receptors. Embo J. 2002;21(7):1743-53.

293. Frick CL, Yarka C, Nunns H, Goentoro L. Sensing relative signal in the Tgf-beta/Smad pathway. Proc Natl Acad Sci U S A. 2017.

294. Guo Y, Wu X, Zheng X, Lu J, Wang S, Huang X. Usefulness of Preoperative Transforming Growth Factor-Beta to Predict New Onset Atrial Fibrillation After Surgical Ventricular Septal Myectomy in Patients With Obstructive Hypertrophic Cardiomyopathy. Am J Cardiol. 2017;120(1):118-23.

295. Anscher MS, Peters WP, Reisenbichler H, Petros WP, Jirtle RL. Transforming growth factor beta as a predictor of liver and lung fibrosis after autologous bone marrow transplantation for advanced breast cancer. N Engl J Med. 1993;328(22):1592-8.

296. Hara Y, Ghazizadeh M, Shimizu H, Matsumoto H, Saito N, Yagi T, et al. Delayed Expression of Circulating TGF-beta1 and BMP-2 Levels in Human Nonunion Long Bone Fracture Healing. Journal of Nippon Medical School = Nippon Ika Daigaku zasshi. 2017;84(1):12-8.

297. Yan Y, Wang XJ, Li SQ, Yang SH, Lv ZC, Wang LT, et al. Elevated levels of plasma transforming growth factor-beta1 in idiopathic and heritable pulmonary arterial hypertension. Int J Cardiol. 2016;222:368-74.

298. Chen XF, Zhang HJ, Wang HB, Zhu J, Zhou WY, Zhang H, et al. Transforming growth factor-beta1 induces epithelial-to-mesenchymal transition in human lung cancer cells via PI3K/Akt and MEK/Erk1/2 signaling pathways. Molecular biology reports. 2012;39(4):3549-56.

299. Chung SW, Miles FL, Sikes RA, Cooper CR, Farach-Carson MC, Ogunnaike BA. Quantitative modeling and analysis of the transforming growth factor beta signaling pathway. Biophys J. 2009;96(5):1733-50.

300. Sorre B, Warmflash A, Brivanlou AH, Siggia ED. Encoding of temporal signals by the TGF-beta pathway and implications for embryonic patterning. Dev Cell. 2014;30(3):334-42.

301. Warmflash A, Zhang Q, Sorre B, Vonica A, Siggia ED, Brivanlou AH. Dynamics of TGF-beta signaling reveal adaptive and pulsatile behaviors reflected in the nuclear localization of transcription factor Smad4. Proc Natl Acad Sci U S A. 2012;109(28):E1947-56.

302. Warmflash A, Zhang Q, Brivanlou AH, Siggia ED. Comment on "Controlling long-term signaling: Receptor dynamics determine attenuation and refractory behavior of the TGF-beta pathway"- Smad2/3 activity does not predict the dynamics of transcription. Science signaling. 2014;7(344):lc1.

303. Pierreux CE, Nicolas FJ, Hill CS. Transforming growth factor beta-independent shuttling of Smad4 between the cytoplasm and nucleus. Mol Cell Biol. 2000;20(23):9041-54.

304. Wang Y, Lui WY. Transforming growth factor-beta1 attenuates junctional adhesion molecule-A and contributes to breast cancer cell invasion. Eur J Cancer. 2012;48(18):3475-87.

305. Tani H, Mizutani R, Salam KA, Tano K, Ijiri K, Wakamatsu A, et al. Genome-wide determination of RNA stability reveals hundreds of short-lived noncoding transcripts in mammals. Genome research. 2012;22(5):947-56.

306. Zieba A, Pardali K, Soderberg O, Lindbom L, Nystrom E, Moustakas A, et al. Intercellular variation in signaling through the TGF-beta pathway and its relation to cell density and cell cycle phase. Mol Cell Proteomics. 2012;11(7):M111 013482.

307. Afrakhte M, Moren A, Jossan S, Itoh S, Sampath K, Westermark B, et al. Induction of inhibitory Smad6 and Smad7 mRNA by TGF-beta family members. Biochem Biophys Res Commun. 1998;249(2):505-11.

308. Itoh S, Landstrom M, Hermansson A, Itoh F, Heldin CH, Heldin NE, et al. Transforming growth factor beta1 induces nuclear export of inhibitory Smad7. J Biol Chem. 1998;273(44):29195-201.

309. Liu S, Nheu T, Luwor R, Nicholson SE, Zhu HJ. SPSB1, a Novel Negative Regulator of the TGF-beta Signaling Pathway Targeting the Type II Receptor. J Biol Chem. 2015.

310. Wang J, Tucker-Kellogg L, Ng IC, Jia R, Thiagarajan PS, White JK, et al. The self-limiting dynamics of TGF-beta signaling in silico and in vitro, with negative feedback through PPM1A upregulation. PLoS Comput Biol. 2014;10(6):e1003573.

311. McCubrey JA, Steelman LS, Chappell WH, Abrams SL, Wong EW, Chang F, et al. Roles of the Raf/MEK/ERK pathway in cell growth, malignant transformation and drug resistance. Biochim Biophys Acta. 2007;1773(8):1263-84.

312. Jiang BH, Liu LZ. PI3K/PTEN signaling in angiogenesis and tumorigenesis. Advances in cancer research. 2009;102:19-65.

313. Castro F, Dirks WG, Fahnrich S, Hotz-Wagenblatt A, Pawlita M, Schmitt M. High-throughput SNP-based authentication of human cell lines. Int J Cancer. 2013;132(2):308-14.

314. Kinsella TM, Nolan GP. Episomal vectors rapidly and stably produce high-titer recombinant retrovirus. Human gene therapy. 1996;7(12):1405-13.

315. Lamartina S, Roscilli G, Rinaudo CD, Sporeno E, Silvi L, Hillen W, et al. Stringent control of gene expression in vivo by using novel doxycycline-dependent trans-activators. Human gene therapy. 2002;13(2):199-210.

316. Boehm ME, Hahn B, Lehmann WD. One-source peptide/phosphopeptide ratio standards for accurate and site-specific determination of the degree of phosphorylation. Methods in molecular biology. 2014;1156:367-78.

317. Law CW, Chen Y, Shi W, Smyth GK. voom: Precision weights unlock linear model analysis tools for RNA-seq read counts. Genome biology. 2014;15(2):R29.

318. Cline MS, Smoot M, Cerami E, Kuchinsky A, Landys N, Workman C, et al. Integration of biological networks and gene expression data using Cytoscape. Nature protocols. 2007;2(10):2366-82.

319. Burgstaller G, Oehrle B, Koch I, Lindner M, Eickelberg O. Multiplex profiling of cellular invasion in 3D cell culture models. PLoS One. 2013;8(5):e63121.

320. InvasionCorrection: Invasion Correction. [Internet]. CRAN. 2017.

321. Beasley MB, Brambilla E, Travis WD. The 2004 World Health Organization classification of lung tumors. Seminars in roentgenology. 2005;40(2):90-7.

322. Dinse GE, Lagakos SW. Nonparametric estimation of lifetime and disease onset distributions from incomplete observations. Biometrics. 1982;38(4):921-32.

323. Raue A, Steiert B, Schelker M, Kreutz C, Maiwald T, Hass H, et al. Data2Dynamics: a modeling environment tailored to parameter estimation in dynamical systems. Bioinformatics. 2015;31(21):3558-60.

324. Raue A, Schilling M, Bachmann J, Matteson A, Schelker M, Kaschek D, et al. Lessons learned from quantitative dynamical modeling in systems biology. PLoS One. 2013;8(9):e74335.

325. Machne R, Finney A, Muller S, Lu J, Widder S, Flamm C. The SBML ODE Solver Library: a native API for symbolic and fast numerical analysis of reaction networks. Bioinformatics. 2006;22(11):1406-7.

6 Appendix

6.1 Tables

	Fishers' Exact Test	
protein	**LC vs AECII**	**LUAD vs LUSC**
BAMBI	$P \leq 0.001$	n.s.
TGFβ	$P \leq 0.001$	n.s.
Smad2	n.s.	$P \leq 0.05$
pSmad2	$P \leq 0.001$	$P \leq 0.05$
Smad3	$P \leq 0.001$	n.s.
pSmad3	$P \leq 0.001$	n.s.
Smad4	n.s.	$P \leq 0.05$
Smad7	$P \leq 0.001$	n.s.
SnoN	$P \leq 0.05$	n.s.
CDH1	$P \leq 0.001$	n.s.
CDH2	n.s.	n.s.
SPP1	$P \leq 0.001$	$P \leq 0.05$

Table S6.1. Immunohistochemical analysis of patient material. Scoring of protein expression levels in different cell types of lung cancer (n = 133 patients) and tumor-free lung tissues (n = 23 patients). Alveolar epithelial cells type I (AECI); Alveolar epithelial cells type II (AECII); Alveolar macrophages (AM); Bronchial epithelial cells (BEC); Connective tissue cells/Fibroblasts(CT); Lung cancer cells (LC); n = 23 (tumor-free lung) and 133 (lung cancer). To address statistical differences in the expression of single targets between AECI, AECII and LC the Fisher Exact test (two-sided) was used with the total number of observed positive and negative cases. Adenocarcinoma (AC) and Squamous cell carcinoma (SQC). Scoring: no expression (0), focal expression (1), frequent expression (2) or expression of target as dominating pattern (3). Analysis performed by Sebastian Marwitz (Research Center Borstel). The table is adapted from Marwitz*, Depner*, Dvornikov* et al. 2016 (189).

	all patients, n = 362		squamous cell carcinoma patients, n = 151	
Parameter	**n**	**(%)**	**n**	**(%)**
Median Age	65 (38-88)		65 (42-83)	
Gender	**362**		**151**	
Male	250	69	125	83
Female	112	31	26	17
Histology				
Adeno	211	58		
Squamous	151	42		
Therapy				
OP	212	59	90	60
OP/RT	13	4	7	5
OP/CT	100	28	45	30
OP/RT/CT	37	10	9	6
P stage				
IA	37	10	11	7
IB	90	25	36	24
IIA	70	19	38	25
IIB	51	14	21	14
IIIA	105	29	42	28
IIIB	9	2	3	2
ECOG				
0	320	88	134	89
1	32	9	11	7
2	4	1	2	1
n.d.	8	2	4	3
smoking status				
Non-smoker	40	11	1	0
Ex-smoker	189	52	84	56
current smoker	131	36	66	44
n.d.	2	0		

Table S6.2. Patient clinical and pathological characteristics. OP = surgery, CT = chemotherapy, RT = radiotherapy, ECOG = Eastern Cooperative Oncology Group, n.d. = no data.

6.2 Figures

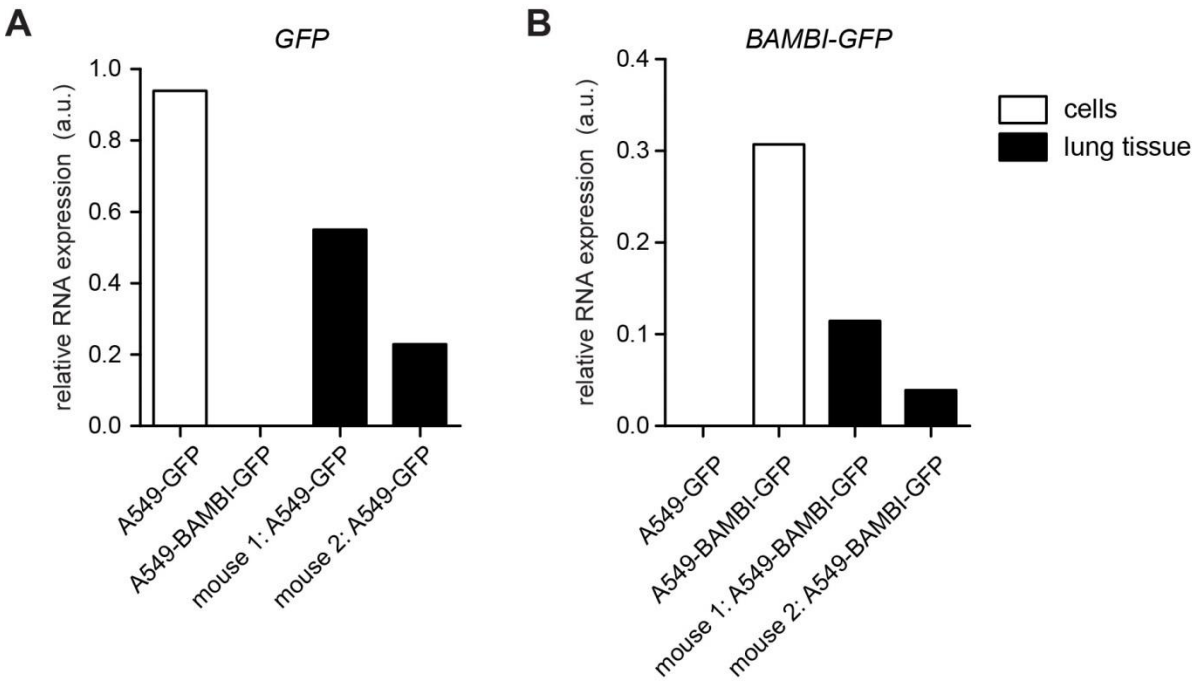

Figure S6.1. GFP- and BAMBI-GFP-positive A549 cells are present in the mice lungs at the time of sacrifice. To investigate the inducible construct expression of human A549 cells within mice lungs, mRNA from HOPE-fixed, paraffin-embedded tissues was analyzed using qRT-PCR to assess presence of either GFP or BAMBI-GFP expression at the experimental endpoint. Primers were designed to specifically recognize either GFP or GFP-BAMBI fusion. Cell blocks of A549-GFP and A549-BAMBI-GFP surplus cells from the day of tail vein injection were included as controls. Exemplary results from 2 animals each group are shown. Advanced relative quantification was used to display relative expression normalized to *RPL32* as reference gene. The figure is adapted from Marwitz*, Depner*, Dvornikov* et al. 2016 (189).

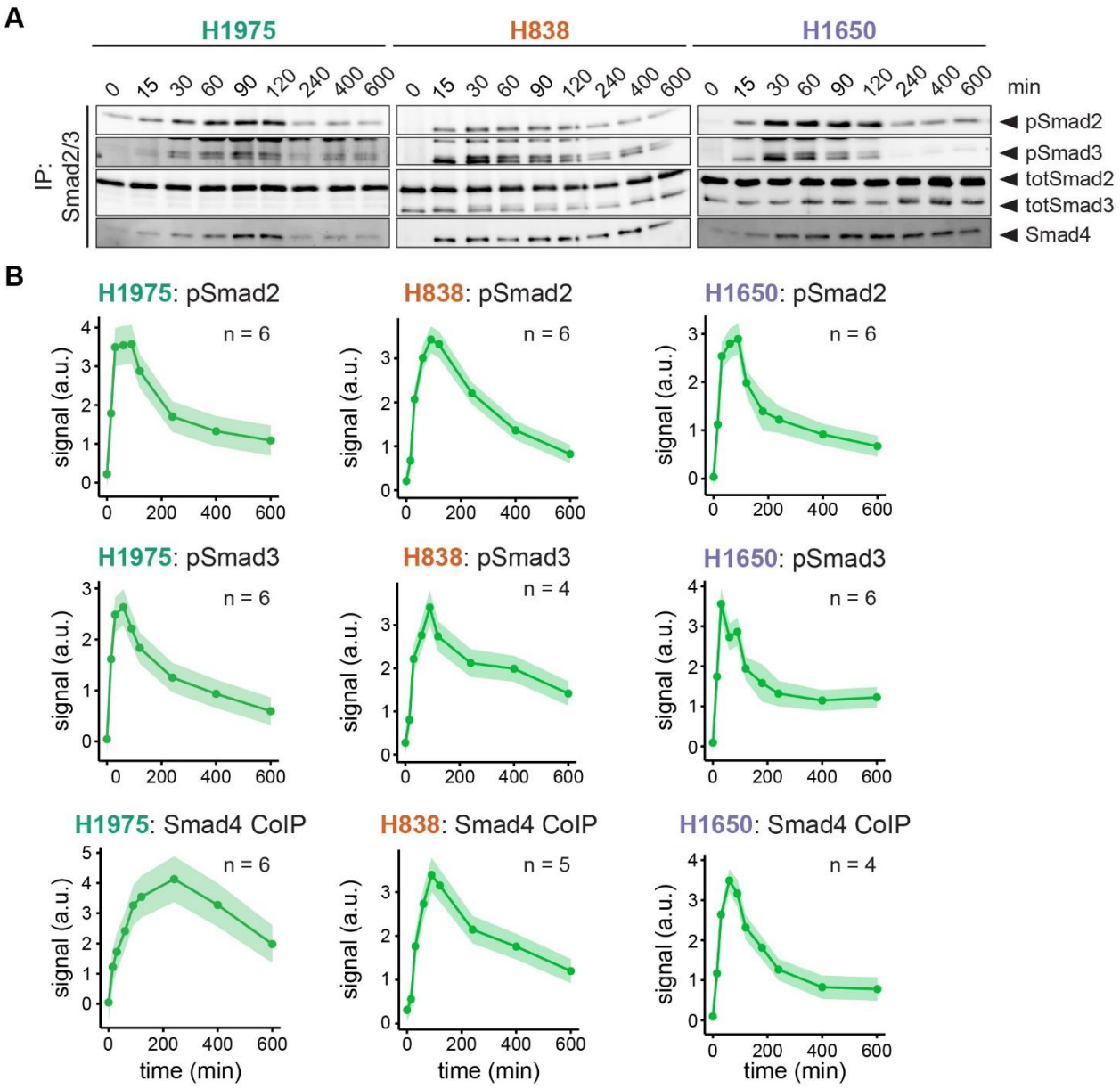

Figure S6.2. TGFβ/Smad signaling pathway dynamics in response to TGFβ stimulation in LUAD cell lines. H838, H1975 and H1650 cells were growth factor-depleted for three hours and stimulated with 1 ng/ml TGFβ and lysed at the indicated time points for time course experiments. Subsequently, cellular lysates were subjected to immunoprecipitation with antibodies against Smad2/3 and analyzed using quantitative immunoblotting. Proteins were visualized with chemiluminescence and detected using ImageQuant LAS 4000 imager. Total (tot) and phosphorylated (p) levels of Smad2 and Smad3, and co-immunoprecipiratied Smad4 (Smad4 CoIP) were assessed. (**A**) Representative immunoblots. (B) Scaled intensities of phosphorylated Smad2 (pSmad2), Smad3 (pSmad3) and co-immunoprecipitated Smad4 (Smad4 CoIP) from several independent experiments using BlotIt script (210). Dots represent mean, shaded areas correspond to standard error estimated by the BlotIt package for R developed by Dr. Daniel Kaschek; n indicates number of independent experiments.

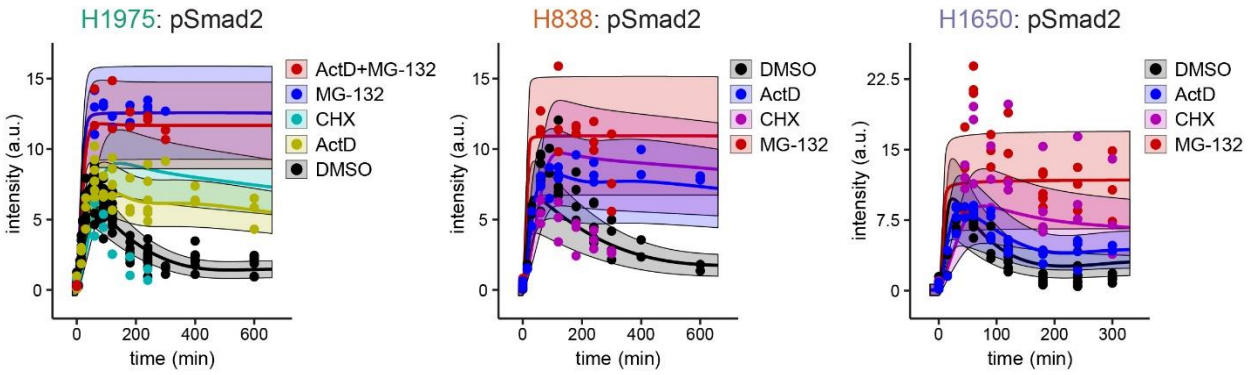

Figure S6.3. Trajectories of the model without any cell type-specific model parameters. Model fits of the inhibitor perturbations on the 3 time-resolved Smad2/phosphorylation dynamics in H1975, H838 and H1650 cells stimulated with 1 ng/ml TGFβ. Cells were pretreated with inhibitors 30 min prior to TGFβ stimulation. Experimental data of the TGFβ-induced Smad2 phosphorylation is shown as dots, model trajectories are shown as lines. Shaded areas correspond to 95% confidence interval estimated by the model. Model analysis was performed by Raphael Engesser (AG Timmer, Freiburg University).

6.3 ODE-based mathematical modeling

6.3.1 Dynamic variables

The model contains 16 dynamic variables. The dynamics of those variables evolve according to a system of ordinary differential equations (ODE) as will be defined in the following. The following list indicates the unique variable names and their initial conditions.

- **Dynamic variable 1:** Smad2

  $[\text{Smad2}](t = 0) = \text{init\_Smad2}$

- **Dynamic variable 2:** Smad3

  $[\text{Smad3}](t = 0) = \text{init\_Smad3}$

- **Dynamic variable 3:** pSmad2

  $[\text{pSmad2}](t = 0) = \text{init\_pSmad2}$

- **Dynamic variable 4:** pSmad3

  $[\text{pSmad3}](t = 0) = \text{init\_pSmad3}$

- **Dynamic variable 5:** Feedback

  $[\text{Feedback}](t = 0) = \text{init\_Feedback}$

- **Dynamic variable 6:** Feedback2

  $[\text{Feedback2}](t = 0) = \text{init\_Feedback2}$

- **Dynamic variable 7:** Rec

  $[\text{Rec}](t = 0) = \text{init\_Rec}$

- **Dynamic variable 8:** Rec_TGFb

  $[\text{Rec\_TGFb}](t = 0) = \text{init\_Rec\_TGFb}$

- **Dynamic variable 9:** TGFb

  $[\text{TGFb}](t = 0) = \text{init\_TGFb}$

- **Dynamic variable 10:** Smad4

  $[\text{Smad4}](t = 0) = \text{init\_Smad4}$

- **Dynamic variable 11:** pSmad3Smad4

  $[\text{pSmad3Smad4}](t = 0) = \text{init\_pSmad3Smad4}$

6.3.2 Reactions

The model contains 26 reactions. Reactions define interactions between dynamics variables and build up the ODE systems. The following list indicates the reaction laws and their corresponding reaction rate equations. Promoting rate modifiers are indicated in black above the rate law arrow. Inhibitory rate modifiers are indicated in red below the rate law arrow. In the reaction rate equations dynamic and input variables are indicated by square brackets. The remaining variables are model parameters that remain constant over time.

- **Reaction 1:**

$$\varnothing \xrightarrow{\text{Rec\_mRNA}} \text{Rec}$$

$$v_1 = -[\text{Rec\_mRNA}] \cdot \text{k\_prod\_rec} \cdot (\text{bool\_CycloH} - 1)$$

- **Reaction 2:**

$$\text{Rec} \longrightarrow \varnothing$$

$$v_2 = -[\text{Rec}] \cdot \text{k\_deg\_rec} \cdot \text{r\_deg\_Rec\_H1650}^{\text{bool\_H1650}} \cdot \text{r\_deg\_Rec\_H838}^{\text{bool\_H838}} \cdot (\text{bool\_MG132} - 1)$$

- **Reaction 3:**

$$\text{Rec} \xrightarrow{\text{TGFb}} \text{Rec\_TGFb}$$

$$v_3 = [\text{Rec}] \cdot [\text{TGFb}] \cdot \text{k\_act\_Rec\_TGFb}$$

- **Reaction 4:**

$$\text{TGFb} \xrightarrow{\text{Rec}} \varnothing$$

$$v_4 = \frac{[\text{Rec}] \cdot [\text{TGFb}] \cdot \text{k\_act\_Rec\_TGFb}}{\text{volume}}$$

- **Reaction 5:**

$$\mathrm{Rec\_TGFb} \longrightarrow \varnothing$$

$$v_5 = -[\mathrm{Rec\_TGFb}] \cdot \mathrm{k\_deg\_Rec\_TGFb\_const} \cdot \mathrm{r\_deg\_Rec\_TGFb\_const\_H1650}^{\mathrm{bool\_H1650}} \cdot \mathrm{r\_deg\_Rec\_TGFb\_const\_H838}^{\mathrm{bool\_H838}} \cdot (\mathrm{bool\_MG132} - 1)$$

- **Reaction 6:**

$$\mathrm{Rec\_TGFb} \xrightarrow{\mathrm{Feedback}} \varnothing$$

$$v_6 = -[\mathrm{Feedback}] \cdot [\mathrm{Rec\_TGFb}] \cdot \mathrm{k\_deg\_rec\_feedback} \cdot \mathrm{r\_deg\_rec\_feedback\_H1650}^{\mathrm{bool\_H1650}} \cdot \mathrm{r\_deg\_rec\_feedback\_H838}^{\mathrm{bool\_H838}} \cdot (\mathrm{bool\_MG132} - 1)$$

- **Reaction 7:**

$$\mathrm{Smad2} \xrightarrow[\mathrm{Feedback2}]{\mathrm{Rec\_TGFb}} \mathrm{pSmad2}$$

$$v_7 = \frac{[\mathrm{Rec\_TGFb}] \cdot [\mathrm{Smad2}] \cdot \mathrm{k\_act\_pS2}}{[\mathrm{Feedback2}] \cdot \mathrm{k\_inh} \cdot \mathrm{r\_inh\_H1650}^{\mathrm{bool\_H1650}} \cdot \mathrm{r\_inh\_H838}^{\mathrm{bool\_H838}} + 1}$$

- **Reaction 8:**

$$\mathrm{pSmad2} \longrightarrow \mathrm{Smad2}$$

$$v_8 = \mathrm{k\_dea\_S2} \cdot [\mathrm{pSmad2}]$$

- **Reaction 9:**

$$\mathrm{Smad3} \xrightarrow[\mathrm{Feedback2}]{\mathrm{Rec\_TGFb}} \mathrm{pSmad3}$$

$$v_9 = \frac{[\mathrm{Rec\_TGFb}] \cdot [\mathrm{Smad3}] \cdot \mathrm{k\_act\_pS3}}{[\mathrm{Feedback2}] \cdot \mathrm{k\_inh} \cdot \mathrm{r\_inh\_H1650}^{\mathrm{bool\_H1650}} \cdot \mathrm{r\_inh\_H838}^{\mathrm{bool\_H838}} + 1}$$

- **Reaction 10:**

$$\mathrm{pSmad3} \longrightarrow \mathrm{Smad3}$$

$$v_{10} = \mathrm{k\_dea\_S3} \cdot [\mathrm{pSmad3}]$$

- **Reaction 11:**

$$2 \cdot \mathrm{pSmad3} + \mathrm{Smad4} \longrightarrow \mathrm{pSmad3Smad4}$$

$$v_{11} = [\mathrm{Smad4}] \cdot \mathrm{k\_form\_S4Coip} \cdot [\mathrm{pSmad3}]^2$$

- **Reaction 12:**

$$2 \cdot \mathrm{pSmad2} + \mathrm{Smad4} \longrightarrow \mathrm{pSmad2Smad4}$$

$$v_{12} = [\mathrm{Smad4}] \cdot \mathrm{k\_form\_S4Coip} \cdot [\mathrm{pSmad2}]^2$$

- **Reaction 13:**

$$\mathrm{pSmad2} + \mathrm{pSmad3} + \mathrm{Smad4} \longrightarrow \mathrm{pSmad23Smad4}$$

$$v_{13} = [\mathrm{Smad4}] \cdot \mathrm{k\_form\_S4Coip} \cdot [\mathrm{pSmad2}] \cdot [\mathrm{pSmad3}]$$

- **Reaction 14:**

$$\mathrm{pSmad3Smad4} \longrightarrow 2 \cdot \mathrm{pSmad3} + \mathrm{Smad4}$$

$$v_{14} = \mathrm{k\_dis\_S4Coip} \cdot [\mathrm{pSmad3Smad4}]$$

- **Reaction 15:**

$$\mathrm{pSmad2Smad4} \longrightarrow 2 \cdot \mathrm{pSmad2} + \mathrm{Smad4}$$

$$v_{15} = \mathrm{k\_dis\_S4Coip} \cdot [\mathrm{pSmad2Smad4}]$$

- **Reaction 16:**

$$\mathrm{pSmad23Smad4} \longrightarrow \mathrm{pSmad2} + \mathrm{pSmad3} + \mathrm{Smad4}$$

$$v_{16} = \mathrm{k\_dis\_S4Coip} \cdot [\mathrm{pSmad23Smad4}]$$

- **Reaction 17:**

$$\varnothing \xrightarrow{\mathsf{Feedback\_mRNA}} \mathrm{Feedback}$$

$$v_{17} = -[\mathrm{Feedback\_mRNA}] \cdot \mathrm{k\_prod\_Feedback} \cdot (\mathrm{bool\_CycloH} - 1)$$

- **Reaction 18:**

$$\mathrm{Feedback} \longrightarrow \varnothing$$

$$v_{18} = -[\mathrm{Feedback}] \cdot \mathrm{k\_deg\_Feedback} \cdot (\mathrm{bool\_MG132} - 1)$$

- **Reaction 19:**

$$\varnothing \xrightarrow{\text{Feedback2\_mRNA}} \text{Feedback2}$$

$$v_{19} = -[\text{Feedback2\_mRNA}] \cdot \text{k\_prod\_Feedback2} \cdot (\text{bool\_CycloH} - 1)$$

- **Reaction 20:**

$$\text{Feedback2} \longrightarrow \varnothing$$

$$v_{20} = -[\text{Feedback2}] \cdot \text{k\_deg\_Feedback2} \cdot (\text{bool\_MG132} - 1)$$

- **Reaction 21:**

$$\text{Rec\_mRNA} \longrightarrow \varnothing$$

$$v_{21} = [\text{Rec\_mRNA}] \cdot \text{k\_deg\_Rec\_mRNA}$$

- **Reaction 22:**

$$\varnothing \longrightarrow \text{Rec\_mRNA}$$

$$v_{22} = -\text{k\_prod\_Rec\_mRNA} \cdot \text{r\_prod\_Rec\_mRNA\_H1650}^{\text{bool\_H1650}} \cdot \text{r\_prod\_Rec\_mRNA\_H838}^{\text{bool\_H838}} \cdot (\text{bool\_ActD} - 1)$$

- **Reaction 23:**

$$\text{Feedback\_mRNA} \longrightarrow \varnothing$$

$$v_{23} = [\text{Feedback\_mRNA}] \cdot \text{k\_deg\_Feedback\_mRNA}$$

- **Reaction 24:**

$$\varnothing \xrightarrow{\text{pSmad3Smad4, pSmad2Smad4, pSmad23Smad4}} \text{Feedback\_mRNA}$$

$$v_{24} = -(\text{k\_prod\_Feedback\_mRNA\_const} + \text{k\_prod\_Feedback\_mRNA} \cdot ([\text{pSmad23Smad4}] + [\text{pSmad2Smad4}] + [\text{pSmad3Smad4}])) \cdot (\text{bool\_ActD} - 1)$$

- **Reaction 25:**

$$\text{Feedback2\_mRNA} \longrightarrow \varnothing$$

$$v_{25} = [\text{Feedback2\_mRNA}] \cdot \text{k\_deg\_Feedback2\_mRNA}$$

- **Reaction 26:**

$$\varnothing \xrightarrow{\text{pSmad3Smad4, pSmad2Smad4, pSmad23Smad4}} \text{Feedback2\_mRNA}$$

$$v_{26} = -(\text{k\_prod\_Feedback2\_mRNA\_const} + \text{k\_prod\_Feedback2\_mRNA} \cdot ([\text{pSmad23Smad4}] + [\text{pSmad2Smad4}] + [\text{pSmad3Smad4}])) \cdot (\text{bool\_ActD} - 1)$$

6.3.3 ODE system

The specified reaction laws and rate equations v determine an ODE system. The time evolution of the dynamical variables is calculated by solving this equation system.

$$
\begin{aligned}
\mathrm{d[Smad2]}/\mathrm{dt} &= -v_7 + v_8 \\
\mathrm{d[Smad3]}/\mathrm{dt} &= -v_9 + v_{10} \\
\mathrm{d[pSmad2]}/\mathrm{dt} &= +v_7 - v_8 - 2 \cdot v_{12} - v_{13} + 2 \cdot v_{15} + v_{16} \\
\mathrm{d[pSmad3]}/\mathrm{dt} &= +v_9 - v_{10} - 2 \cdot v_{11} - v_{13} + 2 \cdot v_{14} + v_{16} \\
\mathrm{d[Feedback]}/\mathrm{dt} &= +v_{17} - v_{18} \\
\mathrm{d[Feedback2]}/\mathrm{dt} &= +v_{19} - v_{20} \\
\mathrm{d[Rec]}/\mathrm{dt} &= +v_1 - v_2 - v_3 \\
\mathrm{d[Rec\_TGFb]}/\mathrm{dt} &= +v_3 - v_5 - v_6 \\
\mathrm{d[TGFb]}/\mathrm{dt} &= -v_4 \\
\mathrm{d[Smad4]}/\mathrm{dt} &= -v_{11} - v_{12} - v_{13} + v_{14} + v_{15} + v_{16} \\
\mathrm{d[pSmad3Smad4]}/\mathrm{dt} &= +v_{11} - v_{14} \\
\mathrm{d[pSmad2Smad4]}/\mathrm{dt} &= +v_{12} - v_{15} \\
\mathrm{d[pSmad23Smad4]}/\mathrm{dt} &= +v_{13} - v_{16} \\
\mathrm{d[Rec\_mRNA]}/\mathrm{dt} &= -v_{21} + v_{22} \\
\mathrm{d[Feedback\_mRNA]}/\mathrm{dt} &= -v_{23} + v_{24} \\
\mathrm{d[Feedback2\_mRNA]}/\mathrm{dt} &= -v_{25} + v_{26}
\end{aligned}
$$

The ODE system was solved by a parallelized implementation of the CVODES algorithm (325). It also supplies the parameter sensitivities utilized for parameter estimation.

6.3.4 Conditions

Conditions modify the model according to replacement rules. New model parameters can be introduced or relations between existing model parameters can be implemented. The following list are default conditions that can be replace my experiment specific conditions defined separately for each data set.

$$
\begin{aligned}
\text{bool\_ActD} &\rightarrow 0 \\
\text{bool\_CycloH} &\rightarrow 0 \\
\text{bool\_MG132} &\rightarrow 0 \\
\text{init\_Feedback} &\rightarrow 1 \\
\text{init\_Feedback2} &\rightarrow 1 \\
\text{init\_Feedback2\_mRNA} &\rightarrow 1 \\
\text{init\_Feedback\_mRNA} &\rightarrow 1 \\
\text{init\_Rec} &\rightarrow \frac{\text{k\_prod\_rec} \cdot \text{r\_prod\_Rec\_mRNA\_H1650}^{\text{bool\_H1650}} \cdot \text{r\_prod\_Rec\_mRNA\_H838}^{\text{bool\_H838}}}{\text{k\_deg\_rec} \cdot \text{r\_deg\_Rec\_H1650}^{\text{bool\_H1650}} \cdot \text{r\_deg\_Rec\_H838}^{\text{bool\_H838}}} \\
\text{init\_Rec\_TGFb} &\rightarrow 0 \\
\text{init\_Rec\_mRNA} &\rightarrow \text{r\_prod\_Rec\_mRNA\_H1650}^{\text{bool\_H1650}} \cdot \text{r\_prod\_Rec\_mRNA\_H838}^{\text{bool\_H838}} \\
\text{init\_pSmad2} &\rightarrow 0 \\
\text{init\_pSmad23Smad4} &\rightarrow 0 \\
\text{init\_pSmad2Smad4} &\rightarrow 0 \\
\text{init\_pSmad3} &\rightarrow 0 \\
\text{init\_pSmad3Smad4} &\rightarrow 0 \\
\text{k\_prod\_Feedback} &\rightarrow \text{k\_deg\_Feedback} \\
\text{k\_prod\_Feedback2} &\rightarrow \text{k\_deg\_Feedback2} \\
\text{k\_prod\_Feedback2\_mRNA\_const} &\rightarrow \text{k\_deg\_Feedback2\_mRNA} \\
\text{k\_prod\_Feedback\_mRNA\_const} &\rightarrow \text{k\_deg\_Feedback\_mRNA} \\
\text{k\_prod\_Rec\_mRNA} &\rightarrow \text{k\_deg\_Rec\_mRNA} \\
\text{volume} &\rightarrow 1
\end{aligned}
$$

7 Abbreviations

5-azaC	5-azacytidine
ActD	actinomycin D
AECII	alveolar epithelial cells type II
Akt	RAC-alpha serine/threonine-protein kinase
ALK	ALK tyrosine kinase receptor
ATCC	american type culture collection
Azin1	antizyme inhibitor 1
BAMBI	BMP and activin membrane-bound inhibitor homolog
Bcl-2	B-cell lymphoma 2
Bcl-X_L	B-cell lymphoma-extra large
Bim	Bcl-2-like protein 11
Bmf	Bcl-2-modifying factor
BMP	bone morphogenetic protein
BRAF	serine/threonine-protein kinase B-raf
BSA	bovine serum albumin
C18ORF1	low-density lipoprotein receptor class A domain-containing protein 4
CBP	CREB-binding protein
CD133	prominin-1
CD24	Signal transducer CD24
CD44	hyaluronate receptor
CDK	cyclin-dependent kinase
CDKi	cyclin-dependent kinase inhibitor
CDKN2A	cyclin-dependent kinase inhibitor 2A
CHX	cycloheximide
CSC	cancer stem cell
CTGF	connective tissue growth factor
CTLA-4	cytotoxic T-lymphocyte protein 4
CXCL1	C-X-C motif chemokine 1
Daxx	death domain-associated protein 6
DMEM	Dulbecco modified Eagle's minimal essential medium

DMSO	dimethyl sulfoxide
DOX	doxycycline
DTT	dithiothreitol
DUSP	dual specificity protein phosphatase
E2F1	E2F transcription factor 1
ECM	extracellular matrix
EDTA	ethylenediaminetetraacetic acid
EGF	epidermal Growth Factor
EGFR	epidermal growth factor receptor
EMT	epithelial-to-mesenchymal transition
ERBB2	receptor tyrosine-protein kinase erbB-2
Erk	extracellular signal-regulated kinase
FCS	fetal calf serum
FGFR	fibroblast growth factor receptor 1
FKBP1A	FK506-binding protein 1A
FoxO	forkhead box protein O1
G6PD	glucose-6-phosphate 1-dehydrogenase
GADD34	growth arrest and DNA damage-inducible protein
GAPDH	glyceraldehyde-3-phosphate dehydrogenase
GFP	green fluorescent protein
GO	gene ontology
GSEA	gene set enrichment analysis
GSK	Glycogen synthase kinase
GST	glutathione S-transferase
GUSB	beta-glucuronidase
H&E	hematoxylin and eosin
HLA	human leukocyte antigen
HMGA1	high mobility group protein A1
HPRT	hypoxanthine-guanine phosphoribosyltransferase
HRP	horseradish peroxidase
Id1	Inhibitor of DNA binding 1
IHC	immunohistochemistry

IL	interleukin
IP	immunoprecipitation
JAK	Janus kinase
JNK	c-Jun N-terminal kinase
KEAP1	kelch-like ECH-associated protein 1
KRAS	GTPase KRas
LAP	latency-associated peptide
LCC	large-cell carcinoma
LIF	leukemia inhibitory factor
LTBP	latent TGFβ-binding protein
LUAD	lung adenocarcinoma
LUSC	lung squamous cell carcinoma
MACS	magnetic-activated cell sorting
MAPK	mitogen-activated protein kinase
MED12	mediator complex subunit 12
MET	hepatocyte growth factor receptor
MH domain	Mad-homology domain
MIP	macrophage inflammatory protein
MMP	metalloproteinase
MSI	microsatellite instability
MSV	Moloney sarcoma virus
MTMR4	myotubularin-related protein 4
mTOR	serine/threonine-protein kinase mTOR
MYC	myc proto-oncogene protein
Nedd4L	E3 ubiquitin-protein ligase NEDD4-like
NES	nuclear export signal
NF-κB	nuclear factor kappa-light-chain-enhancer of activated B cells
NK	natural killer cell
nLC	nano-liquid chromatography
NLS	nuclear localization signal
NOTCH	neurogenic locus notch homolog protein
NOX	NADPH oxidase

NPS	nucleopore signal
NSCLC	non-small-cell lung cancer
ODE	ordinary differential equation
$p15^{INK4B}$	cyclin-dependent kinase 4 inhibitor B
$p21^{CIP1}$	cyclin-dependent kinase inhibitor 1
p300	histone acetyltransferase p300
p38	mitogen-activated protein kinase 14
PAGE	polyacrylamide gel electrophoresis
PBS	phosphate-buffered saline
PCR	polymerase chain reaction
PD-L1	programmed cell death 1 ligand 1
PFA	paraformaldehyde
PI3K	phosphatidylinositol 3-kinase
PIK3CA	PI3-kinase subunit alpha
PLE	profile likelihood estimate
PMEPA1	transmembrane prostate androgen-induced protein
PP2A	protein phosphatase 2A
PPM1A	protein phosphatase 1A
pstage	pathological stage
PTEN	phosphatase and tensin homolog
qRT-PCR	quantitative real-time PCR
RAF	RAF proto-oncogene serine/threonine-protein kinase
RET	proto-oncogene tyrosine-protein kinase receptor Ret
REVIGO	reduce & visualize gene ontology
RIN	RNA integrity number
RIPA	radioimmunoprecipitation assay
RNA-Seq	RNA sequencing
ROS	reactive oxygen species
ROS1	proto-oncogene tyrosine-protein kinase ROS
RPMI	roswell Park Memorial Institute medium
RT	reverse transcriptase
RTK	receptor tyrosine kinase

SBP	streptavidine-binding peptide
SCLC	small-cell lung cancer
SD	standard deviation
SDS	sodium dodecyl sulfate
SEM	standard error of the mean
SIRT1	regulatory protein SIR2 homolog 1
Ski	Ski oncogene
slug	neural crest transcription factor Slug
Smad	mothers against decapentaplegic homolog
Smurf	SMAD ubiquitination regulatory factor
SNAI1	zinc finger protein SNAI1
SnoN	Ski-like protein
SOX2	transcription factor SOX-2
SPP1	secreted phosphoprotein 1
SRA	sequence read archive
STAT	signal transducer and activator of transcription
TAK1	TGF-beta-activated kinase 1
TCGA	the cancer genome atlas
TCL	total cell lysate
TERT	telomerase reverse transcriptase
TGFβ	transforming growth factor beta
TGIF	5'-TG-3'-interacting factor 1
TP53	cellular tumor antigen p53
TRAF6	TNF receptor-associated factor 6
TTF1	transcription termination factor 1
TWIST	Twist-related protein
TβR1	TGF-beta receptor type-1
TβR2	TGF-beta receptor type-2
USP	ubiquitin-specific-processing protease
VEGF	vascular endothelial growth factor
Zeb	zinc finger E-box-binding homeobox 1
ZO-1	tight junction protein ZO-1